Instability of a high-speed vehicle moving through a tunnel embedded in a visco-elastic half-plane

The Hyperloop case

E.M.J. Vicca

Technische Universiteit Delft

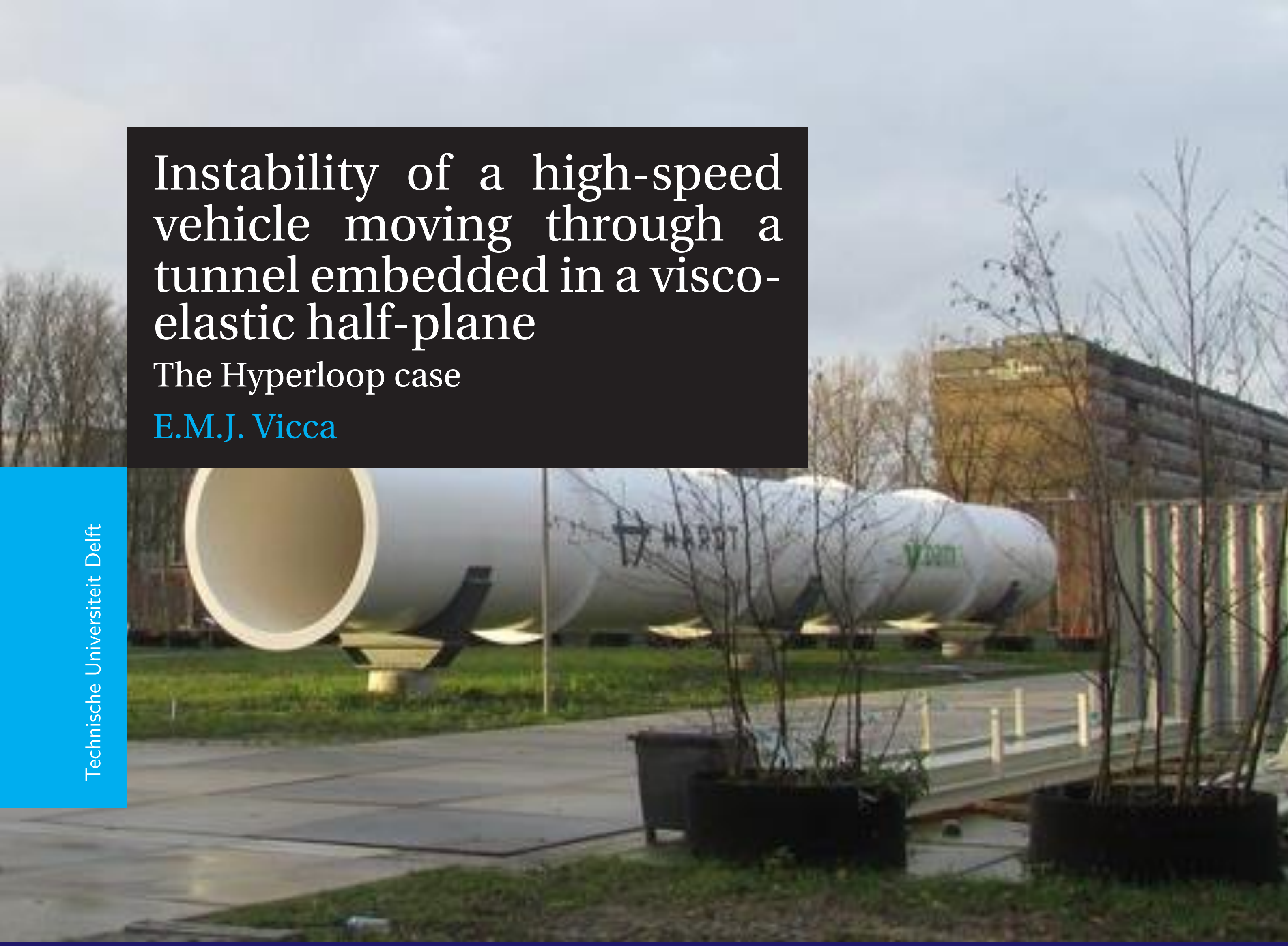

INSTABILITY OF A HIGH-SPEED VEHICLE MOVING THROUGH A TUNNEL EMBEDDED IN A VISCO-ELASTIC HALF-PLANE

THE HYPERLOOP CASE

by

E.M.J. Vicca

in partial fulfillment of the requirements for the degree of

Master of Science
in Civil Engineering

at the Delft University of Technology,
to be defended publicly on Friday January 25, 2019 at 3:00 PM.

Student number:	4281721	
Thesis committee:	Dr. ir. K. N. van Dalen,	TU Delft, supervising chair
	Prof. dr. ir. A. Metrikine,	TU Delft
	Ir. M. Zhao,	TU Delft, daily supervisor
	Ir. T. Lu,	TU Delft

Delft
University of
Technology

PREFACE

This thesis is written in partial fulfillment of the requirements for the degree of Master of Science in Civil Engineering at the Delft University of Technology. The research has been carried out in cooperation with the Structural Mechanics group at the Faculty of Civil Engineering. I started working on it at the end of February 2018 and now I am very proud to present to you the results of my research.

I decided to write my thesis in the field of structural dynamics after following the course 'Structural Dynamics', which is given by professor Andrei Metrikine. I worked hard on understanding the topics covered in that master course, but afterwards still felt the need to dive further into the domain of dynamics of structures. As I was already following the developments of the Hyperloop project, I was immediately interested when Karel van Dalen suggested I would work on a project introduced by the Delft Hyperloop team.

I could never have completed this research without the help of the members of my thesis committee and I would like to express my sincere thanks to all of them. My daily supervisor, Mingjuan Zhao, was there every step of the way. She was always prepared to help me when I had an issue and very patiently explained the methods I should follow to solve it. At one moment in my research I encountered a problem with my results and Karel van Dalen, Tao Lu and Mingjuan Zhao made a huge effort to help me through. During the course of the research we had several meetings and after each meeting I felt I had gained very valuable knowledge. I am also very grateful to professor Andrei Metrikine. During the progress meetings he gave me many useful insights on the topic of my research. He played a very important role in solving some of the problems encountered and contributed significantly to the fact that, during the last nine months, I have learned more than I could have imagined.

To my family and friends I would like to say thank you for all the support. A special thanks goes to my parents and parents-in-law for all the hours of babysitting while I was working on my thesis, to my children for making me laugh when I was a little stressed and last but not least to my husband for his unconditional support not only during the course of this research, but during the past five years of studying.

E.M.J. Vicca
Delft, December 2018

SUMMARY

Hyperloop is a high-speed transportation mode which operates by sending magnetically levitated capsule-like vehicles through a near vacuum tunnel. Due to the reduced air resistance and friction, speeds exceeding those of modern aircraft should become possible. When the system is moved underground, the stability of vehicle vibrations may become problematic as, especially in soft soils, the Hyperloop pod velocities could easily surpass the propagation speeds of waves in the soil. In that case, the radiation of anomalous Doppler waves into the system may lead to instability of vehicle vibrations, which means that the amplitude of the vibrations would grow exponentially.

The aim of this study is to evaluate the system's stability and its sensitivity to changes in the model by using analytical methods. To that end, the study is motivated by two central research questions: (1) How can the system be modelled and described, taking into account the interaction between soil, tunnel and vehicle and how does the model description change when the magnetic levitation suspension system is introduced? (2) What is the influence of the model parameters on the system's stability and what impact do modifications in the vehicle suspension have?

The first research question is answered by modelling the underground Hyperloop system as a two-mass oscillator moving uniformly along an infinitely long Euler-Bernoulli beam embedded in a visco-elastic half-plane. Through definition of the governing equations of motion, boundary and interface conditions and subsequent application of Laplace and Fourier integral transforms, the model is reduced to a lumped model for which the characteristic equation has been derived. In the latter model, the reaction of the beam-half-plane system in the point of contact with the moving load is represented by an equivalent dynamic spring stiffness. The introduction of the magnetic levitation adds a magnetic spring to the lumped model. This spring is placed in series with the equivalent spring representing the beam-half-plane stiffness.

The second research question is answered by first studying the velocity-dependent equivalent dynamic stiffness of the supporting structure in the point of contact with the moving oscillator as a function of the frequency of the oscillator vibrations. When the imaginary part of this stiffness is negative, instability of vertical oscillator vibrations may occur due to so-called negative radiation damping. Then, based on the D-decomposition method, the instability domain is found for the base parameters of the system, whereupon this instability zone is parametrically studied. The influence of the magnetic levitation suspension system is established by deriving the instability domain for two different models of a concrete tunnel and various magnitudes of the viscous damping in the vehicle.

It is found that the model parameters significantly influence the system's stability. The oscillator's viscosity in particular has an important stabilizing effect. For both the non-magnetically and magnetically levitated vehicle, a limited magnitude of the oscillator's viscous damping stabilizes the system for all velocities up to 300 m/s. Therefore, instability should not be considered as a real danger for the Hyperloop vehicle. Yet, when the electrodynamic levitation suspension system is accounted for, the total mass of the Hyperloop pod and the parameters of the non-contact suspension system should be determined with care as a change in their values may influence the instability domain considerably.

CONTENTS

LIST OF FIGURES

ACRONYMS

EDS	electrodynamic suspension.
SDOF	single degree of freedom system.
EOM	equation of motion.
DOFs	degrees of freedom.
BC	boundary conditions.
IC	interface conditions.

GLOSSARY

sign	description	unit
$v_{\mathrm{ph}}^{\mathrm{min}}$	minimum phase speed of the bending waves in the beam	m/s
$\chi_{\mathrm{eq}}^{\mathrm{h\text{-}p}}$	equivalent stiffness of the half-plane interacting with the beam	$\mathrm{N/m^2}$
$\chi_{\mathrm{eq}}^{\mathrm{beam}}$	equivalent stiffness beam in the point of contact with the moving oscillator	N/m
λ_{mag}	wavelength of the Halbach array of permanent magnets	m
m	mass	kg
k_0	spring constant	N/m
c_0	damping coefficient	Ns/m
ζ	damping ratio = $\frac{c_0}{2*\sqrt{km}}$	-
Ω_n	natural frequency of undamped vibration = $\sqrt{\frac{k}{m}}$	rad/s
Ω_1	$= \omega_n \sqrt{1-\zeta^2}$	rad/s
$A_0 \exp(-\zeta\Omega_n t)$	amplitude of the harmonic vibration	rad/s
θ	phase angle	rad/s
χ	stiffness of the elastic foundation	$\mathrm{N/m^2}$
EI	flexural rigidity of the beam	$\mathrm{Nm^2}$
A	cross-sectional area of the beam	$\mathrm{m^2}$
ρ_{b}	mass density of the beam	$\mathrm{kg/m^3}$
ϵ	strain	-
κ	curvature	-
ϕ_y	rotation around the y-axis	-
w_{b}	vertical displacement of the beam in the time-space domain	m
E	Young's modulus	$\mathrm{N/m^2}$
J	rotational inertia	$\mathrm{kgm^2}$
ϵ_{d}	damping coefficient of the visco-elastic foundation	$\mathrm{Ns/m^2}$
$\delta(x)$	Dirac-delta function centered in $x=0$	1/m
c	wave speed	m/s
ω	radial frequency of wave	rad/s
k	wavenumber of the bending waves in the beam	1/m
T	period of the wave	s
λ_0	wavelength of wave	m
θ_0	phase of the wave	-
v_{ph}	phase velocity of the wave	m/s
ω_0	cut-off frequency	rad/s
v_{gr}	group velocity of the packet of waves	m/s
∇	nabla operator for two dimensions $\left[\frac{\partial}{\partial x} \quad 0 \quad \frac{\partial}{\partial z}\right]^T$	-
λ	1st Lamé parameter = $\frac{\nu E}{(1+\nu)(1-2\nu)}$	$\mathrm{N/m^2}$
μ	2nd Lamé parameter, also called shear modulus = $\frac{E}{2(1+\nu)}$	$\mathrm{N/m^2}$
ρ	mass density of the half-plane	$\mathrm{kg/m^3}$
ν	poisson ratio of the material	-

sign	description	unit
K_b	bulk modulus of the material	$\mathrm{N/m^2}$
δ_{ij}	Kronecker delta with $\delta_{ij} = 1$ if $i = j$ and $\delta_{ij} = 0$ if $i \neq j$	-
σ_{xz}	shear stress in the half-plane in the time-space domain	$\mathrm{N/m^2}$
σ_{zz}	vertical half-plane stress in the time-space domain	$\mathrm{N/m^2}$
c_L	wave speed of compressional wave = $\sqrt{\frac{\lambda+2\mu}{\rho}}$	m/s
k_L	wavenumber of compressional wave	1/m
c_T	wave speed of shear wave = $\sqrt{\frac{\mu}{\rho}}$	m/s
k_T	wavenumber of shear wave	1/m
ϕ	scalar potential which contains the compressional part of the particle motion	$\mathrm{m^2}$
$\boldsymbol{\psi}$	vector potential which contains the rotational part of the particle motion and for a 2D-model: $\boldsymbol{\psi}=\begin{bmatrix}0 & \psi_y & 0\end{bmatrix}^T = \psi$	$\mathrm{m^2}$
Ω	radial frequency of the oscillator's vertical vibrations	rad/s
v_b	vertical displacement of the beam in the Laplace-Fourier domain	m
m_1	lower mass of the oscillator	kg
F_{lift}	lift force of the electrodynamic suspension system	N
g_1	gap between the top magnets and the track for a maglev train in the Inductrack system	m
b_{top}	width of the Halbach array magnets at the top	m
k_{mag}	wavenumber of the Halbach array permanent magnets = $\frac{2\pi}{\lambda_{\text{mag}}}$	1/m
b_{side}	width of the Halbach array magnets at the side	m
g_2	gap between the side magnets and the track for a maglev train in the Inductrack system	m
N_c	number of lifting coils in the track per wavelength λ_{mag} of the magnets	-
B_0	peak strength of the magnetic field at the surface of the Halbach arrays	T
ϕ_0	peak flux enclosed by the circuit	Wb
L	inductance of the circuit	H
R	resistance of the circuit	Ω
ω_{mag}	angular frequency of the magnetic field due to the motion of the train $\left(\omega_{\text{mag}} = k_{\text{mag}}V\right)$	rad/s
b_{mag}	width of the Halbach array magnets	m
g_{nom}	nominal gap between the magnets and the track in the Inductrack system	m
μ_0	permeability of free space	H/m
P_c	perimeter of a coil in the track	m
d_c	distance between the midplanes of adjacent coils	m
ρ_r	electrical resistivity of a material	Ω m
A_c	cross-sectional area of a coil in the track	$\mathrm{m^2}$
m_{b}	mass per unit length of the beam	kg/m
h	depth of the beam from the ground surface	m
V	constant longitudinal velocity of the oscillator	m/s
m_2	upper mass of the oscillator	kg
K	stiffness of the oscillator	N/m
ϵ_0	viscosity of the oscillator	Ns/m
$P(t)$	harmonic load in the time domain	N
$\hat{\lambda}$	adapted 1st Lamé parameter, taking into account viscosity of the half-plane; $\hat{\lambda} = \lambda + \lambda^* \frac{\partial}{\partial t}$	$\mathrm{N/m^2}$

sign	description	unit
$\hat{\mu}$	adapted 2nd Lamé parameter, taking into account viscosity of the half-plane; $\hat{\mu} = \mu + \mu^* \frac{\partial}{\partial t}$	N/m^2
$\delta(x - Vt)$	Dirac-delta function centered in $x = Vt$	1/m
w_1	vertical displacement of mass m_1 in the time domain	m
w_2	vertical displacement of mass m_2 in the time domain	m
a	characteristic length representing the length of the structure in the y-direction	m
u	horizontal displacement of the soil in the time-space domain	m
w	vertical displacement of the soil in the time-space domain	m
$\delta(\xi)$	Dirac-delta function centered in ξ	1/m
f	compressional part of the half-plane motion in the Laplace-wavenumber domain symbol	
s	Laplace variable $s = \sigma + i\Omega$ with σ and Ω real numbers [16]	rad/s
g	rotational part of the half-plane motion in the Laplace-wavenumber domain symbol	
v_1	vertical displacement of mass m_1 in the Laplace-wavenumber domain	m
v_2	vertical displacement of mass m_2 in the Laplace-wavenumber domain	m
p	harmonic load in the Laplace domain	N
S_{zz}	vertical half-plane stress in the Laplace-wavenumber domain	N/m^2
S_{xz}	shear stress in the half-plane in the Laplace-wavenumber domain	N/m^2
μ_{sk}	$= \mu + \mu^*(s - ikV)$	N/m^2
α	$= c_L^2 - 2c_T^2$	m^2/s^2
β	$= R_L^2 c_L^2$	$1/s^2$
k_1	stiffness of the nonlinear spring representing the magnetic levitation suspension system	N/m
h_{mag}	height of the Halbach array permanent magnets	m

1

INTRODUCTION

The market share for high-speed traffic grows quickly. By 2050 it is expected that 41% of the world traffic market share will be high-speed transport [17]. For long distance travel, flying is currently the fastest and cheapest option. However, for shorter distances the efficiency of air transport reduces significantly as the necessary activities before the flight (reaching the aiport in time, check-in, security control, et cetera) can take up more time than the actual flight. Hyperloop aims to offer a high-speed, ecological and affordable alternative for those short-haul aviation routes. Although the idea of high-speed tube transport was already examined in the late 20th century, the concept of the Hyperloop was first presented by Elon Musk in 2013. First developments were made by engineers of Musk's companies, Tesla Motors and SpaceX. Hyperloop is a high-speed transportation mode which operates by sending bullet-shaped capsules, also called pods, through a steel tube, maintained at a partial vacuum. Due to the reduced air resistance and friction, speeds up to 1220 km/h should become possible [18, 19]. As the Hyperloop concept is still in development, different possibilities are being explored. Currently, the third test track is under construction in France. This test track will be one km long and will be built on pylons above ground, just like the other two existing tracks in the US. As construction of large steel tubes above ground will often not be possible or desirable, the option of moving the system underground requires consideration and the issues encountered when making this modification need to be studied. This chapter acts to introduce the problem that this thesis will focus on, to outline the research objectives and questions, and to give an overview of the structure of this thesis.

1.1. PROBLEM STATEMENT

In order to make an underground Hyperloop tube possible, the effects of sending pods at very high speeds through a tunnel have to be examined. At high speeds the vertical vibrations of the mass (pod) can become unstable which implies that the amplitude of the mass vibrations would grow exponentially [20]. Therefore, determination of the pod speed at which this instability occurs is imperative. The critical pod velocity depends on the properties of the tube, the pods and the soil. It is important to understand that *instability* is not the same as *resonance*. The latter takes place when the velocity of the moving vehicle corresponds to the group velocity of waves propagating in the system. Thus, resonance arises at specific individual velocities while instability occurs in a certain velocity range. Furthermore, while resonance can be eliminated completely by increasing the foundation viscosity, the instability domain in that case only moves to higher velocities. Therefore, in practice, the instability phenomenon is even more unfavourable than resonance [10, 20].

A parametric study will show the effect of factors like the soil and tube parameters, the vehicle mass, the stiffness of the pod's springs and dampers on the instability of vibrations of the moving pod. As the Hyperloop system employs a magnetic levitation suspension system to avoid friction between wheels and track, this thesis investigates the influence of such a suspension system on the critical pod velocity and the instability.

1.2. RESEARCH OBJECTIVE AND QUESTIONS

The research problem as described above can be translated into the following two research objectives:

1. *Gain insight in the vibrations of a high-speed vehicle moving in a tunnel and in the effect of the magnetic levitation of the vehicle on its vibrations.*

   The first part of this research focuses on the vibrations of the mass (vehicle) by modelling the interaction between the moving capsule, the tube and the soil. For this research, it is assumed that the vehicle moves at a constant velocity. The effect of the introduction of the magnetic levitation suspension system on the description of the problem is studied as well.

2. *Study the effect of the system properties on the instability of vertical vehicle vibrations.*

   This objective is reached by conducting parametric studies and hence determining the effect of the soil, beam and vehicle properties. Furthermore, the influence of changes in the model, like the introduction of the non-contact suspension system, is examined.

Based on this dual research objective, two central research questions can be formulated:

1. *How can the motion of a high-speed vehicle moving in a tunnel be modelled and described taking into account the interaction between soil, tunnel and vehicle? How does the description of the motion change when the magnetic levitation suspension system is introduced?*

2. *What is the influence of the model parameters on the stability of the vehicle vibrations and what impact do modifications in the vehicle suspension have?*

There is a strong relation between both research questions. The first research question needs to be answered in order to be able to perform the parametric study and answer question two. Furthermore, when answering question one, it is necessary that the model parameters are included in a transparent way in order to make subsequent investigation of the influence of the relevant parameters possible.

By formulating sub-questions the necessary steps to answer both central research questions become apparent.

Sub-questions belonging to central question one are:

a *How can the vehicle-tube-soil system be modelled?*

In order to understand the dynamic interaction between the moving pods, the tube and the soil, a model which simulates the reality is necessary. Many different modelling possibilities are available and the choice of the model will influence the eventual results. In answering this sub-question, numerous decisions have to be made. How many dimensions will be considered? How will the soil be modelled? Is the soil assumed to be homogeneous or layered? Is the viscosity of the soil taken into account? Does the model consider shear deformation or is only bending deformation included? How to model the vehicle-tunnel system?

b *What are the governing equations of motion for the soil, for the tube and for the uniformly moving vehicle in the tube and how do they relate?*

Once the models have been defined, the dynamic behaviour of soil, tube and vehicle is described by means of equations of motion. These equations are based on Newton's second law which states that the rate of change of momentum of a mass is proportional to the force acting on it [16].

c *Which boundary and interface conditions have to be accounted for?*

d *Based on the answers to sub-questions a) to c), how can the soil-beam system be characterized and based on this characterization, how are the vehicle vibration described?*

Find the characteristic equation which enables the analysis of instability of vertical vehicle vibrations. For this purpose, Fourier and Laplace transforms are important tools as they allow the transition from the time/space to the frequency/wavenumber domain and vice versa.

e *How does the introduction of a non-contact suspension system influence the answers to sub-questions a) to d)?*

Sub-questions belonging to central question two are:

a *Up to which velocity are the vibrations of the vehicle unconditionally stable for a given set of parameters?*

b *When examining the moving vehicle vibrations, from which velocity does instability occur?*

c *How does a change in the model parameters influence the outcome of sub-question b) ?*

Parametric studies are carried out to give insight into the variables that influence the critical velocity for vibration instability. The results are represented in such a way that the reader can easily derive the influence of each of the parameters. Graphs are an important means to this end.

d *What is the effect of a change in the vehicle suspension on the instability of the vehicle vibrations?*

To complete the analysis of the Hyperloop pod's stability, the effect of the magnetic levitation suspension system is studied for different models of the tunnel and different values of the viscous damping in the vehicle.

1.3. REPORT STRUCTURE

THIS report is broken into four main chapters: a literature review, a chapter deriving the equation which describes the vehicle motion, the analysis of instability of vehicle vibrations for the model of an oscillator moving along an embedded beam and a chapter introducing the magnetic levitation suspension system into the model.

The second chapter is a literature study comprising two main parts. The first part treats the general theory on dynamics of structures that is relevant to this research. Subjects like Fourier and Laplace transforms, soil and wave dynamics, vibrations of systems with a discrete number of degrees of freedom and of continuous systems are included. A second part investigates the relevant state-of-the-art concerning oscillator vibrations for a vehicle moving either in a tunnel or on the ground surface. Finally, this section reviews literature relevant for the inclusion of the magnetic levitation suspension system in the model.

The third chapter depicts the vehicle-tube-soil model for which the instability is considered in this research. The soil is modelled as a two-dimensional visco-elastic half-plane, while the pod is represented by a two-mass moving oscillator which is in direct contact with an infinitely long Euler-Bernoulli beam acting as the tube embedded in the half-plane. For this model the relevant equations of motion with corresponding boundary and interface conditions are described. A study of the roots of the characteristic equation enables us to make a conclusion with respect to the instability of the oscillator's vibrations. To define this characteristic equation, the equivalent dynamic stiffness of the beam in the contact point with the moving oscillator is derived in accordance with the procedure applied by Metrikine *et al.* ([12, 13]). This complex-valued dynamic stiffness depends both on the frequency of vibrations of the moving oscillator and on its velocity. It is obtained by first reducing the two-dimensional model to the model of a beam resting on a visco-elastic foundation having a foundation stiffness equal to the stiffness of the half-plane [21]. Application of the inverse Fourier transform then results in the expression of the equivalent dynamic stiffness of the beam in the point of contact with the moving vehicle.

The fourth chapter starts with the analysis of the equivalent dynamic stiffness of the beam. The imaginary part of this stiffness is in fact the equivalent viscosity of the beam in the point of contact with the moving oscillator [13]. For different oscillator velocities and a given set of model parameters, frequency bands for which the imaginary part of the equivalent dynamic stiffness of the beam corresponds to a 'negative viscosity' are examined and the velocity range for which the oscillator vibrations are unconditionally stable is determined.
In the next section the velocity range in which unstable vehicle vibrations occur is studied by plotting the critical value of one oscillator parameter against the oscillator velocity. A parametric study investigates the effect of each of the model parameters on the size and shape of the instability domain.

In the fifth chapter the magnetic levitation suspension system is introduced in the model. Hyperloop employs an electrodynamic suspension (EDS) system using Halbach arrays of permanent magnets on the pods. This chapter first examines the way the suspension system can be included, whereupon the characteristic equation for the adapted model is derived. Based on this characteristic equation, the instability analysis is carried out. The instability domain for the vertical vibrations of both the Hyperloop competition pod and a full-scale vehicle model is derived. Finally, the impact of a change in the tube and vehicle parameters is examined.

A concluding chapter explains the relevance of this research for the problem at hand and presents a critical reflection of the research method and the results.

2

LITERATURE REVIEW

In order to clarify later steps that will be taken when solving the research problem, the first part of this chapter reviews relevant theory on dynamic behaviour of structures. Areas of interest include methods that can be used to analytically model vibrations of a mass on a beam, relevant theory on wave dynamics, the Laplace and Fourier transforms and an overview of relevant soil dynamics topics. The second part of this chapter is dedicated to previous work which is relevant to the current study of instability of vibrations of a high-speed Hyperloop pod moving in a tunnel.

2.1. DYNAMICS OF STRUCTURES - RELEVANT THEORY

THIS section gives an overview of the necessary theoretical background for finding the solutions to the research questions described in the first chapter.

2.1.1. MOTION OF MASS AND BEAM

In order to gain insight in the consequences of dynamic loads, structural systems (bridges, buildings, tunnels, etc.) and the impact they experience (wind, traffic, earthquakes, etc.) are schematized [16]. To understand the vehicle-tube model that will be used in this research, first the response of a simple single degree of freedom system (SDOF) including a spring and a dashpot is described. Because of its later importance, the instability phenomenon will be touched upon as well. Then the behaviour of a loaded bending beam on a visco-elastic foundation is analyzed starting from the motion of such a beam on a Winkler foundation.

SINGLE DEGREE OF FREEDOM SYSTEM (SDOF) AND INSTABILITY

Figure 2.1 shows a SDOF with mass m, a spring constant k_0 and a damping coefficient c_0 which is loaded by a random time dependent load $F(t)$. The vertical displacement of the mass as a function of time, $y(t)$ is considered.

From Newton's second law, which connects the acceleration to the internal and external forces, the equation governing the motion of this system can be derived. Initial conditions are included for defining specific problems [22].

$$\begin{aligned} &m\ddot{y} + c_0\dot{y} + k_0 y = F(t), \\ &y(0) = y_0 \qquad , \dot{y}(0) = v_0. \end{aligned} \tag{2.1}$$

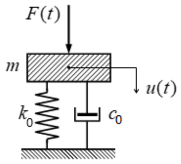

Figure 2.1: SDOF under a random load [1].

An alternative form of the equation of motion is

$$\ddot{y}+2\zeta\Omega_n\dot{y}+\Omega_n^2 y=\frac{F(t)}{m}. \tag{2.2}$$

Unforced motion When the external force F(t) is absent, eq. (2.2) reduces to a homogeneous differential equation for which the characteristic equation and eigenvalues are given by [23]

$$\begin{aligned} &s^2+2\zeta\Omega_n s+\Omega_n^2=0,\\ &s_{1,2}=-\zeta\Omega_n\pm\Omega_n\sqrt{\zeta^2-1}. \end{aligned} \tag{2.3}$$

Based on eq. (2.3), the general solution for a single degree of freedom system with viscous damping is derived:

$$y(t)=\sum_{n=1}^{2}Y_n\exp(s_n t)=\exp(-\zeta\Omega_n t)\left[Y_1\exp(\Omega_n t\sqrt{\zeta^2-1})+Y_2\exp(-\Omega_n t\sqrt{\zeta^2-1})\right]. \tag{2.4}$$

This solution clearly depends on the value of the damping ratio ζ. Four cases are relevant:

1. undamped system: $\zeta=0$:

   $$y(t)=A\cos(\Omega_n t)+B\sin(\Omega_n t)=A_0\cos(\Omega_n t+\theta),$$

   the roots $s_{1,2}$ of the characteristic equation are purely imaginary and the unforced system vibrates at its natural frequency Ω_n,

2. damped vibration: $-1<\zeta<1$ and $\zeta\neq 0$:

   $$y(t)=\exp(-\zeta\Omega_n t)\left[A\cos(\Omega_1 t)+B\sin(\Omega_1 t)\right]=A_0\exp(-\zeta\Omega_n t)\cos(\Omega_1 t+\theta),$$

   where $\Omega_1=\Omega_n\sqrt{1-\zeta^2}$ and the roots $s_{1,2}$ of the characteristic equation are complex and their real part determines whether the system will be stable or unstable,

3. critically damped system: $\zeta=1$:

   $$y(t)=A\exp(-\Omega_n t)+Bt\exp(-\Omega_n t),$$

   he roots $s_{1,2}$ of the characteristic equation coincide,

4. aperiodic motion: $\zeta\leq-1$ or $\zeta>1$:

   $$y(t)=A\exp\left(-\Omega_n t(\zeta-\sqrt{\zeta^2-1})\right)+B\exp\left(-\Omega_n t(\zeta+\sqrt{\zeta^2-1})\right),$$

   the roots $s_{1,2}$ of the characteristic equation are both real and the value of ζ determines whether the system is stable.

System stability A dynamical system is unstable when a small initial perturbation grows in time. In this case the system does not return to its equilibrium position. For the undamped and the critically damped case, the system will always be stable. However, when $\zeta \neq 0$ and $\zeta \neq 1$, dynamic instability may occur.

First consider the case where $-1 < \zeta < 1$ and $\zeta \neq 0$. In the expression for $y(t)$ given in item 2 above, only the term before the square brackets determines whether the system is stable as the term between the brackets neither decays nor grows in time. When at least one of the eigenvalues $s_{1,2}$ has a positive real part $(= -\zeta\Omega_n)$, instability occurs and the amplitude of the harmonic vibration $(= A_0 \exp(-\zeta\Omega_n t))$ will grow exponentially in time. Thus, considering that the natural frequency is always positive, the system will be unstable for $-1 < \zeta < 0$.

In case of the aperiodic motion, it follows from the expression for $y(t)$ that the displacement will grow exponentially when $\zeta \leq -1$. After all, in that case, both exponents are always positive. On the other hand, the system is stable for all $\zeta > 1$.

In conclusion, the stability of a damped system depends on the real part of its eigenvalues. When at least one of those eigenvalues has a positive real part, dynamic instability takes place. This will happen when the system is negatively damped: $\zeta < 0$.

Forced motion The force $F(t)$ is dealt with by dividing the total solution into two parts: a homogeneous solution and a particular solution. The homogeneous solution y_h is simply the general solution for the unforced damped motion that has been examined above. The particular solution y_p is found by choosing a solution with unknown constants in the same form as the load, or, in other words, with the same time signature as the load. The unknown coefficients are found by substituting the chosen expression for the displacement in the original equation of motion. The complete general solution is then obtained by adding y_h and y_p:

$$y(t) = y_\mathrm{h}(t) + y_\mathrm{p}(t).$$

The initial conditions are implemented in this total solution in order to find the solution to the initial value problem 2.1.

If there is dissipation in the system, the free vibration will gradually subside with time. As mentioned before, this means that positive damping needs to be present. The stationary situation that remains after the transient motion has died out is called the steady state response:

$$y_\mathrm{steady}(t) = \lim_{t\to\infty} y(t).$$

In case the system is dynamically unstable, the free vibration does not decay. On the contrary, it grows exponentially, which means that the steady state will not be reached.

INFINITELY LONG BENDING BEAM ON A (VISCO-)ELASTIC FOUNDATION

In this subsection the behaviour of an infinitely long Euler-Bernoulli beam on an elastic foundation with distributed stiffness χ is described. Once this description is found, the step towards finding the equations describing the motion of such a beam on a visco-elastic foundation is small.

The governing equation of motion for a small element dx of the beam shown in fig. 2.2 is derived following the displacement method. This method starts with the kinematic relations, then considers the constitutive equations and finally, Newton's second law is applied to find the governing EOM for the bending beam on an elastic foundation, loaded with a distributed load $f(x,t)$. From this equation of motion the unknown displacement can then be derived. EI is the flexural rigidity of the beam and its mass per unit length is equal to the product of the cross-sectional area A and the mass density of the beam ρ_b. As mentioned before, this section considers the behaviour of an Euler-Bernoulli beam loaded in bending. Therefore, shear deformation and the influence of rotational inertia are neglected, which can only be defended for slender beams and low frequencies [23].

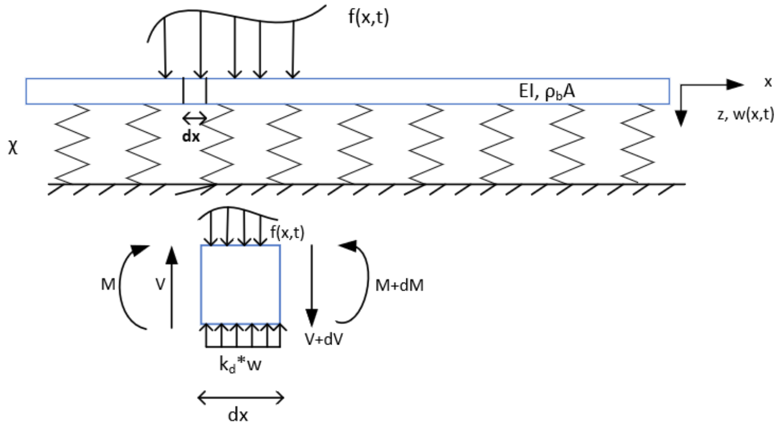

Figure 2.2: Beam on elastic foundation and sign convention.

Kinematic relations The kinematic equations relate the displacements to the deformations. For a beam loaded in bending, the deformations are the strain, ϵ, the curvature, κ, and the rotation, ϕ_y. There is only one unknown displacement in this case, i.e. the vertical displacement $w_\mathrm{b}(x,t)$.

Figure 2.3 shows the relation between the curvature and the rotation of the beam on the left hand side and that between the rotation and the vertical beam displacement on the right hand side. The expression for ϵ as a function of the vertical co-ordinate and the curvature can be derived from figure 2.4. This gives us the following kinematic equations:

$$\phi_y = -\frac{dw_\mathrm{b}}{dx}, \tag{2.5a}$$

$$\kappa = \frac{d\phi_y}{dx} = -\frac{d^2 w_\mathrm{b}}{dx^2}, \tag{2.5b}$$

$$\epsilon(z) = \frac{d(z\phi_y)}{dx} = z\kappa. \tag{2.5c}$$

Equation (2.5a) is only valid if the cross-section is perpendicular to the neutral line, before as well as after the deformation. This is true for the slender beam because, as assumed earlier, shear deformation can then be neglected.
Equation (2.5c) results from the Bernoulli assumption that plane cross-sections remain plane [23].

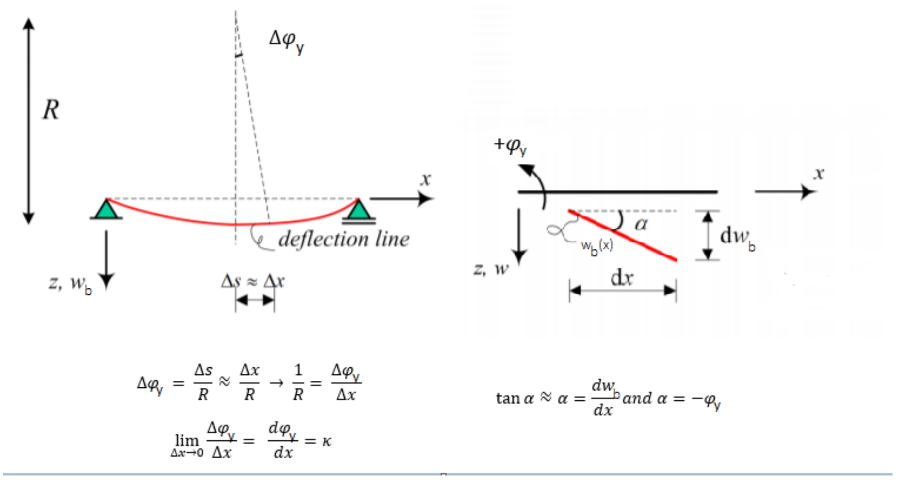

Figure 2.3: Relationship curvature-rotation and sign convention for a beam in bending [2].

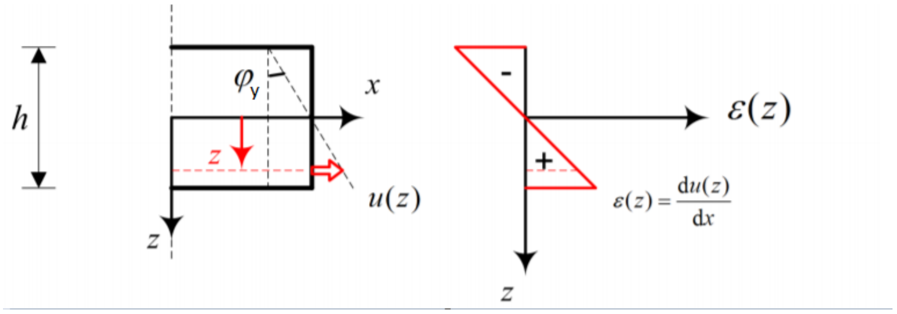

Figure 2.4: Derivation of $\epsilon(z)$ [2].

Constitutive relations The constitutive relations are derived from the material behaviour. They relate the deformations to the internal forces. For the case of the Euler-Bernoulli beam loaded in bending, the relationship between the internal bending moment M and the curvature κ has to be found. In what follows, linear-elastic material behaviour is assumed and therefore Hooke's law applies:

$$\sigma(z) = \epsilon(z) * E = z\kappa E. \tag{2.6}$$

Based on figure 2.5 the expression for the relation between M and κ is found as [2]

$$\begin{aligned} M &= \int_{z=-\frac{h}{2}}^{z=\frac{h}{2}} dM = \int_{z=-\frac{h}{2}}^{z=\frac{h}{2}} z\,dN = \int_{z=-\frac{h}{2}}^{z=\frac{h}{2}} z\sigma(z)\,dA \\ &= E\int_{z=-\frac{h}{2}}^{z=\frac{h}{2}} z\epsilon(z)\,dA = E\kappa\int_{z=-\frac{h}{2}}^{z=\frac{h}{2}} z^2\,dA = EI\kappa. \end{aligned} \tag{2.7}$$

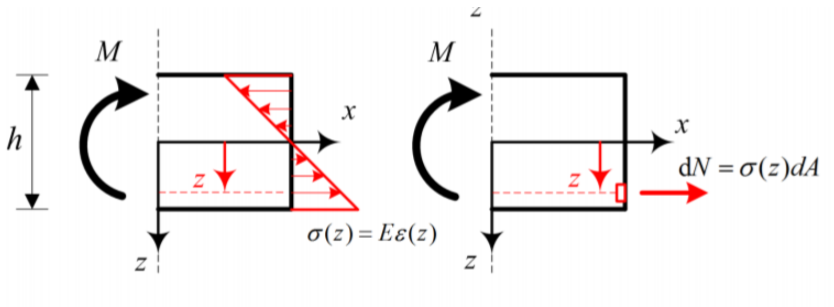

Figure 2.5: Derivation of relation between M and κ [2].

Newton's second law In a last step towards finding the governing equation of motion Newton's second law, which relates acceleration to the internal forces, is applied. Only rotation and vertical displacements are taken into account while rotational inertia is neglected. For an infinitesimal element dx of the beam the following equations are derived based on the sign convention of fig. 2.2 [23]:

- for the ϕ_y-direction, assuming $\rho_\text{b} J = 0$:

$$\begin{aligned} &\sum T_y = 0, \\ &dM - V\,dx = 0, \\ &\frac{dM}{dx} = V, \end{aligned} \tag{2.8}$$

- for the z-direction:

$$\begin{aligned} &\sum F_z = m a_z, \\ &dV + f\,dx = \rho_\text{b} A\,dx \frac{\partial^2 w_\text{b}}{\partial t^2} + \chi w_\text{b}\,dx, \\ &\frac{d^2 M}{dx^2} + f = \rho_\text{b} A \frac{\partial^2 w_\text{b}}{\partial t^2} + \chi w_\text{b}, \\ &EI \frac{\partial^2 \kappa}{\partial x^2} + f = \rho_\text{b} A \frac{\partial^2 w_\text{b}}{\partial t^2} + \chi w_\text{b}, \\ &\rho_\text{b} A \frac{\partial^2 w_\text{b}(x,t)}{\partial t^2} + EI \frac{\partial^4 w_\text{b}(x,t)}{\partial x^4} + \chi w_\text{b}(x,t) = f(x,t). \end{aligned} \tag{2.9}$$

This last inhomogeneous partial differential equation describes the motion of the bending beam placed on an elastic foundation with constant stiffness χ and loaded by a distributed load $f(x,t)$.

EOM for visco-elastic foundation Instead of assuming the foundation is purely elastic, it is often physically more realistic to include the viscosity of the foundation in the model. Figure 2.6 shows the configuration of an infinite Euler-Bernoulli beam on a visco-elastic Kelvin foundation with distributed stiffness χ and damping coefficient per unit length ϵ_d. In this case, the equation of motion in eq. (2.9) is changed in the following way:

$$\rho_\text{b} A \frac{\partial^2 w_\text{b}(x,t)}{\partial t^2} + \frac{\partial^4 w_\text{b}(x,t)}{\partial x^4} + \chi w_\text{b}(x,t) + \epsilon_\text{d} \frac{\partial w_\text{b}(x,t)}{\partial t} = f(x,t). \tag{2.10}$$

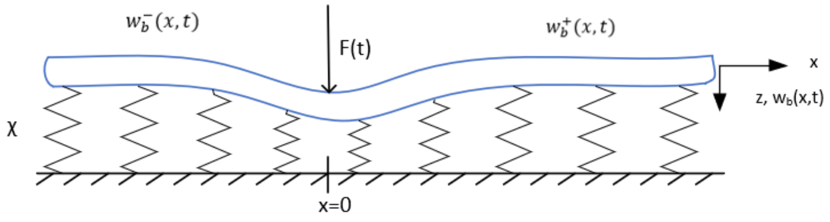

Figure 2.7: Beam on elastic foundation loaded by a point load.

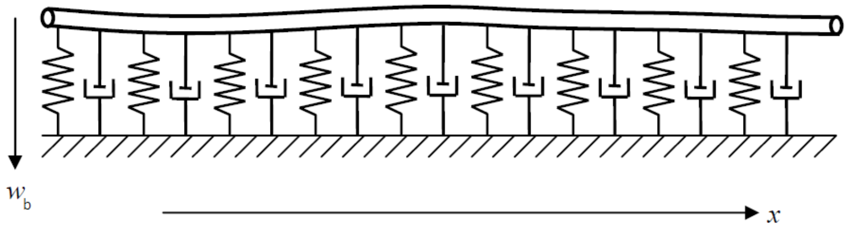

Figure 2.6: Model of an infinite beam on a visco-elastic foundation [3].

EOM and boundary conditions for beam with point load For further reference the specific case of an infinite bending beam loaded by a point load and placed on a Winkler foundation is considered. This situation is shown in fig. 2.7.

The equations of motion for this case are defined as

$$\rho_b A \frac{\partial^2 w_b^+(x,t)}{\partial t^2} + EI \frac{\partial^4 w_b^+(x,t)}{\partial x^4} + \chi w_b^+(x,t) = 0 \quad \text{for} \quad x > 0, \quad \text{and} \tag{2.11a}$$

$$\rho_b A \frac{\partial^2 w_b^-(x,t)}{\partial t^2} + EI \frac{\partial^4 w_b^-(x,t)}{\partial x^4} + \chi w_b^-(x,t) = 0 \quad \text{for} \quad x < 0. \tag{2.11b}$$

$$\tag{2.11c}$$

The point load is taken into account in the interface conditions which are defined at the loading point:

$$w_b^+(0,t) = w_b^-(0,t), \tag{2.12a}$$

$$\frac{\partial w_b^+(0,t)}{\partial t} = \frac{\partial w_b^-(0,t)}{\partial t}, \tag{2.12b}$$

$$\frac{\partial^2 w_b^+(0,t)}{\partial t^2} = \frac{\partial^2 w_b^-(0,t)}{\partial t^2}, \tag{2.12c}$$

$$EI\left(\frac{\partial^3 w_b^+(0,t)}{\partial t^3} - \frac{\partial^3 w_b^-(0,t)}{\partial t^3}\right) = F(t). \tag{2.12d}$$

The boundary conditions at plus and minus infinity are:

- at $x \to -\infty$:

  - Sommerfeld's radiation condition: all energy is radiated outward, so all waves are outgoing, there is no energy propagation in the positive x-direction [24],
  - the response is finite at infinite distance from the source: $\lim_{x\to-\infty}(|w_\mathrm{b}^-(x,t)|) < \infty$,
- at $x \to +\infty$:
  - Sommerfeld's radiation condition: all energy is radiated outward, so all waves are outgoing, there is no energy propagation in the negative x-direction [24],
  - the response is finite at infinite distance from the source: $\lim_{x\to+\infty}(|w_\mathrm{b}^+(x,t)|) < \infty$.

Instead of splitting the beam up into two parts and defining two separate equations of motion as well as interface conditions at the loading point, the motion of the bending beam on the elastic foundation can also be described using the Dirac-delta function. In that case, no interface conditions are needed and only the boundary conditions at plus and minus infinity have to be defined. For the beam in fig. 2.7, the following equation of motion is obtained:

$$\rho_\mathrm{b} A \frac{\partial^2 w_\mathrm{b}(x,t)}{\partial t^2} + EI \frac{\partial^4 w_\mathrm{b}(x,t)}{\partial x^4} + \chi w_\mathrm{b}(x,t) = F(t)\delta(x). \tag{2.13}$$

The boundary conditions at minus and plus infinity remain exactly the same as described above.

2.1.2. LAPLACE AND FOURIER TRANSFORM

This section treats two important tools for the analysis of vibration and wave propagation problems. The Fourier and Laplace transform provide a method to transform problems from the time-space domain to the frequency-wavenumber domain. With respect to the data analysis, these techniques make it possible to characterize an in- or output signal by determining which frequencies are present in the signal. Furthermore, by transforming the problem from the time-space domain to the frequency-wavenumber domain, partial differential equations are reduced to ordinary differential equations and even simple algebraic equations. As both the Fourier and the Laplace transform are based on the linear superposition principle, an exact solution to the equation of motion using these techniques can only be obtained for linear systems [25].

FOURIER TRANSFORM

The forward Fourier transform with respect to the spatial variable x transforms a function from the x-domain to the wavenumber (=k) domain. Thus, for each fixed time t, the forward Fourier transform of $w_\mathrm{b}(x,t)$ with respect to x is obtained as

$$w_\mathrm{b}(k,t) = \int_{-\infty}^{+\infty} w_\mathrm{b}(x,t) \exp(-\mathrm{i}kx)\, dx. \tag{2.14}$$

By means of the inverse Fourier transform the function $w_\mathrm{b}(x,t)$ can be recovered:

$$w_\mathrm{b}(x,t) = \frac{1}{2\pi} \int_{-\infty}^{+\infty} w_\mathrm{b}(k,t) \exp(\mathrm{i}kx)\, dk. \tag{2.15}$$

For a specific time moment t, the function $w_\mathrm{b}(k,t)$ indicates how much of any component with wavenumber k is present in the signal.

As seen before, the EOM for the infinite Euler-Bernoulli beam on an elastic foundation contains fourth order derivatives with respect to space. The Fourier transform of the derivative $\frac{\partial w_\mathrm{b}(x,t)}{\partial x}$ is obtained using integration by parts:

$$\begin{aligned} w_{\mathrm{b}}'(k,t) &= \int\limits_{-\infty}^{+\infty} w_{\mathrm{b}}'(x,t)\exp\left(-ikx\right)dx = w_{\mathrm{b}}(x,t)\exp\left(-\mathrm{i}kx\right)\Big|_{-\infty}^{+\infty} - \int\limits_{-\infty}^{+\infty} w_{\mathrm{b}}(x,t)\left(-\mathrm{i}k\right)\exp\left(-\mathrm{i}kx\right)dx, \\ &= 0 + \mathrm{i}k\int\limits_{-\infty}^{+\infty} w_{\mathrm{b}}(x,t)\exp\left(-\mathrm{i}kx\right)dx, \\ &= \mathrm{i}k w_{\mathrm{b}}(k,t), \end{aligned} \tag{2.16}$$

assuming that $w_{\mathrm{b}}(x,t) \to 0$ for $x \to -\infty$.

The Fourier transforms of the second to fourth derivative with respect to the x-co-ordinate are derived in the same way:

$$w_{\mathrm{b}}''(k,t) = \int\limits_{-\infty}^{+\infty} w_{\mathrm{b}}''(x,t)\exp\left(-ikx\right)dx = \mathrm{i}k w_{\mathrm{b}}'(k,t) = \left(\mathrm{i}k\right)^2 w_{\mathrm{b}}(k,t) = -k^2 w_{\mathrm{b}}(k,t), \tag{2.17a}$$

$$w_{\mathrm{b}}'''(k,t) = \int\limits_{-\infty}^{+\infty} w_{\mathrm{b}}'''(x,t)\exp\left(-ikx\right)dx = \mathrm{i}k w_{\mathrm{b}}''(k,t) = \left(\mathrm{i}k\right)^3 w_{\mathrm{b}}(k,t) = -\mathrm{i}k^3 w_{\mathrm{b}}(k,t), \tag{2.17b}$$

$$w_{\mathrm{b}}''''(k,t) = \int\limits_{-\infty}^{+\infty} w_{\mathrm{b}}''''(x,t)\exp\left(-ikx\right)dx = \mathrm{i}k w_{\mathrm{b}}'''(k,t) = \left(\mathrm{i}k\right)^4 w_{\mathrm{b}}(k,t) = k^4 w_{\mathrm{b}}(k,t). \tag{2.17c}$$

When studying the steady state behaviour of a system, the Fourier transform can also be used with respect to the time variable in order to analyze the behaviour of the system in the frequency domain.

After applying the Fourier transform with respect to the x-co-ordinate to eq. (2.13), the following equation in the time-wavenumber domain is obtained:

$$\rho_{\mathrm{b}} A \frac{\partial^2 w_{\mathrm{b}}(k,t)}{\partial t^2} + EIk^4 w_{\mathrm{b}}(k,t) + \chi w_{\mathrm{b}}(k,t) = F(t)\exp\left(-\mathrm{i}k\cdot 0\right) = F(t), \tag{2.18}$$

where the shift property of the Dirac delta function is used:

$$\int\limits_{-\infty}^{+\infty} f(t)\delta(t-t_0)\,dt = f(t_0). \tag{2.19}$$

LAPLACE TRANSFORM

As this study examines the (in)stability of a system, the Laplace transform with respect to time has to be considered, as the steady-state response will not be reached in case of instability. This technique transforms a function from the time to the Laplace domain:

$$w_{\mathrm{b}}(x,s) = \int\limits_{0}^{+\infty} w_{\mathrm{b}}(x,t)\exp\left(-st\right)dt. \tag{2.20}$$

The Laplace s can contain a real and an imaginary part: $s = \sigma + \mathrm{i}\Omega$. This implies that, contrary to the Fourier transform, the Laplace transform not only considers the oscillatory part of the signal (the sinusoidal part), but also its changing magnitude (the exponential part).

The EOM for the infinite Euler-Bernoulli beam on an elastic foundation contains second order derivatives with respect to time. The Laplace transform of the derivative can be obtained similarly to the Fourier transform of the derivatives that were described above:

$$\begin{aligned}\dot{w}_{\mathrm{b}}(x,s) &= \int_{0}^{+\infty} \dot{w}_{\mathrm{b}}(x,t)\exp(-st)\,dt = w_{\mathrm{b}}(x,t)\exp(-st)\Big|_{0}^{+\infty} - \int_{0}^{+\infty} w_{\mathrm{b}}(x,t)\big(-s\big)\exp(-st)\,dt,\\ &= 0 + s\cdot w_{\mathrm{b}}(x,s), \qquad (2.21\text{a})\\ \ddot{w}_{\mathrm{b}}(x,s) &= \int_{0}^{+\infty} \ddot{w}_{\mathrm{b}}(x,s)\exp(-st)\,dt = s^{2}\cdot w_{\mathrm{b}}(x,s). \qquad (2.21\text{b})\end{aligned}$$

If the Laplace transform is applied to eq. (2.18), we receive the following equation in the (complex) frequency - wavenumber domain:

$$\begin{aligned}&\rho_{\mathrm{b}}As^{2}w_{\mathrm{b}}(k,s) + EIk^{4}w_{\mathrm{b}}(k,s) + \chi w_{\mathrm{b}}(k,s) = F(s),\\ &\big(\rho_{\mathrm{b}}As^{2} + EIk^{4} + \chi\big)w_{\mathrm{b}}(k,s) = F(s).\end{aligned} \qquad (2.22)$$

2.1.3. WAVE DYNAMICS

When studying vibrations, one considers only the motion of an object in time around an equilibrium state. The way energy goes from one location to the other is not considered in this case. However, when examining waves, one wants to know how a disturbance propagates through a medium, i.e. how energy is transported from one location to the other. The topic of waves has already briefly been touched upon at the end of section 2.1.1. This section will further elaborate on the dynamics of waves and treat the wave theory that is relevant for this study.

WAVE PROPAGATION

Wave equation Consider the one-dimensional classical wave equation:

$$\frac{\partial^{2}w(x,t)}{\partial t^{2}} = c^{2}\frac{\partial^{2}w(x,t)}{\partial x^{2}}, \qquad (2.23)$$

where c is equal to the speed of the propagating wave. One example of the many physical phenomena that can be modelled by this equation is the transverse vibration of a taut string [26].

D'Alembert (1747) developed the following classical solution to this equation [6]:

$$w(x,t) = f^{+}(x-ct) + f^{-}(x+ct). \qquad (2.24)$$

In eq. (2.24), $f^{+}(x-ct)$ represents a wave propagating in the positive x-direction without distortion (with its shape unchanged), while $f^{-}(x+ct)$ represents a wave propagating in the negative x-direction without distortion. So, any solution of the wave equation 2.23 is the sum of a wave traveling rightwards and a wave traveling leftwards. The specific shape of $f^{+}(x-ct)$ and $f^{-}(x+ct)$ is determined by the initial conditions of the problem [6]. Making use of a small example, the fact that the wave $f^{+}(x-ct)$ is propagating in the positive x-direction can be derived from the argument $(x-ct)$:

Suppose $f^{+}(x-ct) = w_0\exp\frac{-(x-ct)^2}{x_0^2}$, then:

- for $t = 0$: $f^+(x) = w_0 \exp\left(\frac{-x^2}{x_0^2}\right)$ and this function reaches its maximum at $x = 0$,
- for $t = t^* > 0$: $f^+(x - ct^*) = w_0 \exp\frac{-(x-ct^*)^2}{x_0^2}$ and the maximum is reached at $x - ct^* = 0$ so at $x = ct^* > 0$ and that means that the wave propagates in the positive x-direction.

The d'Alembert solution describes waves propagating without changing shape. When the wave equation is changed, for example by adding distributed stiffness or damping terms to it, there will be dispersion of waves. In that case, the d'Alembert solution can not be used anymore as the expression for $w(x,t)$ (eq. (2.24)) will no longer satisfy the governing equation of motion. However, the description of propagating waves above is still useful for the later interpretation of the wave motion.

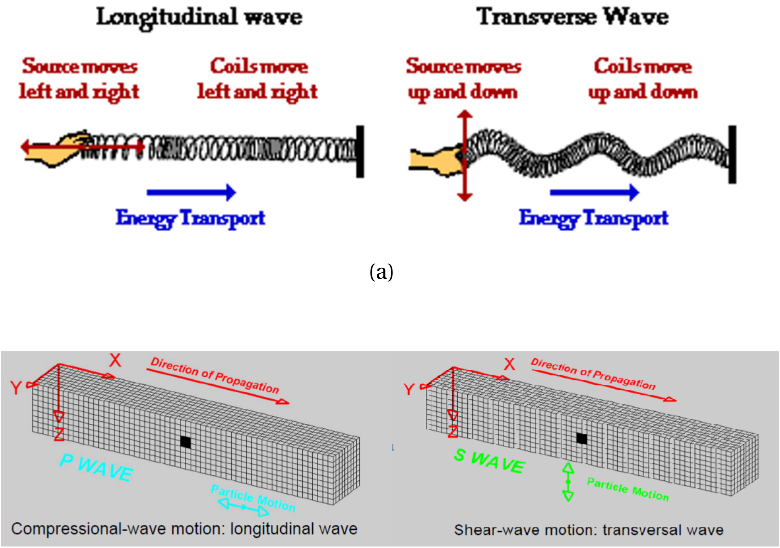

(a)

(b)

Figure 2.8: Difference between longitudinal and transverse wave for (a) a 'slinky' [4] and (b) an elastic continuum [5].

Longitudinal and transverse waves If the vibration direction of the particles of the medium through which the wave travels is aligned with the propagation direction of the wave, one speaks of a longitudinal wave, also called compressional wave. In a transverse or shear wave, the pulse travels perpendicular to the direction of motion of the disturbance [4] (see also section 2.1.4). The difference between both types of waves is shown in fig. 2.8 for both a 'slinky' and an elastic continuum.

REPRESENTATION AND PARAMETERS OF A HARMONIC WAVE

The harmonic wave To understand the propagation of distortions in the soil and in a bending beam, the concept of the harmonic wave is introduced. Just as any function of time can be expressed as the superposition of harmonic vibrations (see section 2.1.2), any wave which is a function of spatial coordinate x and time t can be expressed as the superposition of harmonic waves. The Fourier representation of a wave is [6] defined as

$$w(x,t) = \frac{1}{4\pi^2} \int_{-\infty}^{+\infty} \int_{-\infty}^{+\infty} W(k,\omega) \exp\left(\mathrm{i}(\omega t - kx)\right) d\omega\, dk. \tag{2.25}$$

So an harmonic wave can be represented using the following complex form:

$$w(x,t) = \hat{W}_0 \exp\left(\mathrm{i}(\omega t - kx)\right), \tag{2.26}$$

where $\hat{W}_0$ is the (complex) amplitude which may depend on the radial frequency of the wave ω and the wavenumber k, but is always independent of x and t. As described above $f^+(x-ct)$ is a wave propagating in the positive x-direction. Analogously, the wave in eq. (2.26) is propagating in the positive x-direction due to the argument $(\omega t - kx)$. The main characteristics of a harmonic wave are [6]:

- amplitude = maximum displacement that wave moves away from its equilibrium [m] [4] (see fig. 2.9),
- ω = radial frequency of the wave [rad/s],
- $T = \frac{2\pi}{\omega}$ = period of the wave [s] (see fig. 2.9),
- $f = \frac{1}{T} = \frac{\omega}{2\pi}$ = cyclic frequency of the wave [1/s or Hz],
- k = wavenumber [rad/m],
- $\lambda_0 = \frac{2\pi}{k}$ = wavelength of the wave [m] (see fig. 2.9),
- $\theta_0 = \omega t - kx$ = phase of the wave [-], and
- $v_{\mathrm{ph}} = \frac{dx}{dt} = \frac{\omega}{k}$ = velocity with which a the constant phase moves [m/s] .

The expression for the phase velocity as a function of ω and k is derived as follows:

$$\theta_0 = \omega t - kx = \text{constant}, \qquad \text{so:}$$
$$\frac{\partial \theta_0}{\partial t} = \omega - k\frac{dx}{dt} = \omega - k v_{\mathrm{ph}} = 0.$$

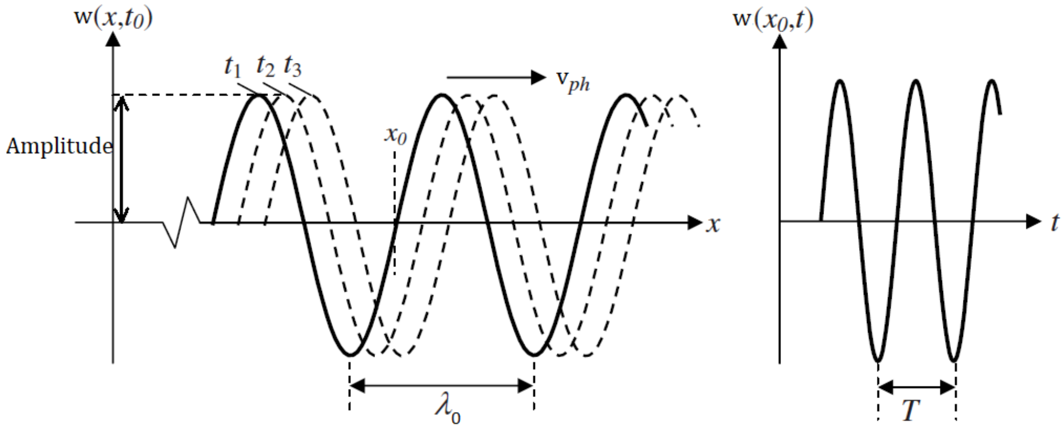

Figure 2.9: Harmonic wave [6].

Phase velocity Because of the importance of the phase velocity for the later analysis, a more detailed explanation of this wave characteristic is relevant. The phase velocity is the velocity with which crests and troughs of the wave travel [27]. Suppose the wave can be described by

$$w(x,t) = \cos(\omega t - kx),$$

then, a crest occurs when the phase $\omega t - kx$ is equal to zero, or, in other words, when $x = \frac{\omega t}{k}$. As can be derived from fig. 2.9, the distance the peak has traveled from t_1 to t_2 is equal to $x_2 - x_1 = \frac{\omega t_2}{k} - \frac{\omega t_1}{k}$. As the phase velocity equals the distance the peak has traveled divided by the time it has taken to travel this distance, it can be concluded that $v_{\mathrm{ph}} = \frac{\omega}{k}$.

Dispersion relation

The dispersion equation for bending waves in the beam relates frequency ω and wavenumber k and therefore describes what frequency and wavelength a wave in the structure may have [27]. The dispersion relation is a property of the structure (in this case the beam-foundation system) and is independent of the load working on the structure. It can be obtained from the substitution of the expression for the wave $w_{\mathrm{b}}(x,t)$:

$$w_{\mathrm{b}}(x,t) = \hat{W}_{b,0} \exp\left(\mathrm{i}(\omega t - kx)\right)$$

into the equation of motion:

$$\rho_{\mathrm{b}} A \frac{\partial^2 w_{\mathrm{b}}(x,t)}{\partial t^2} + EI \frac{\partial^4 w_{\mathrm{b}}(x,t)}{\partial x^4} + \chi w_{\mathrm{b}}(x,t) + \epsilon_{\mathrm{d}} \frac{\partial w_{\mathrm{b}}(x,t)}{\partial t} = 0.$$

In what follows the value of the foundation damping coefficient ϵ_{d} is taken equal to zero.

The dispersion relation for bending waves in an Euler-Bernoulli beam on an elastic foundation is then given by the expression [6]:

$$-\rho_{\mathrm{b}} A \omega^2 + EIk^4 + \chi = 0, \tag{2.27a}$$

$$-\omega^2 + \frac{EI}{\rho_{\mathrm{b}} A} k^4 + \omega_0^2 = 0, \tag{2.27b}$$

where $\omega_0 = \sqrt{\frac{\chi}{\rho_{\mathrm{b}} A}}$ is the cut-off frequency. From eq. (2.27b) one can see that this cut-off frequency is the frequency for which the wavenumber $k = 0$. The dispersion relation 2.27b is plotted in the fig. 2.10.

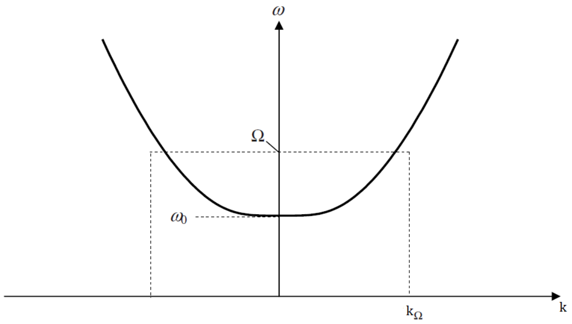

Figure 2.10: Dispersion relation for bending waves in a beam on an elastic foundation [6].

As mentioned in reference [6], a harmonic force with a frequency larger than the cut-off frequency excites waves, while such a force only perturbs exponentially decaying in space vibrations when its frequency is below the cut-off frequency. When the frequency of the force equals the cut-off frequency, resonance occurs because, in that case, the group velocity of the waves $v_{\mathrm{gr}} = \frac{\partial \omega}{\partial k}$ is equal to zero. As the group velocity gives the speed with which the group of waves perturbed by the load travels, there will be no energy propagation when this velocity drops to zero. This means that the energy accumulates at the introduction point of the load and resonance occurs.

2.1.4. SOIL DYNAMICS

As the understanding of wave propagation in the soil is essential for the study, this section deals with the motion of the soil particles. First the equation of motion for a linear-elastic, homogeneous half-space is considered. Because of its later importance, a second part of this section treats the Helmholtz decomposition for the displacement vector of the soil particles. A few examples are presented to clarify the physical meaning of the theoretical descriptions included in this section.

SOIL EQUATION

Governing equations for a continuum Figure 2.11 presents the three-dimensional homogeneous half-space. As chapters 3 and 4 consider a two-dimensional model for the soil (a half-plane) only displacements in the vertical (z-) and horizontal (x-) direction are considered in this section.

Navier's equation describes the motion of a linear-elastic homogeneous continuum without body forces [28]:

$$\mu \nabla^2 \boldsymbol{u} + (\lambda + \mu) \nabla (\nabla \cdot \boldsymbol{u}) = \rho \frac{\partial^2 \boldsymbol{u}}{\partial t^2}, \tag{2.28}$$

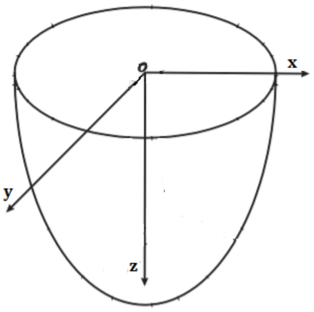

Figure 2.11: Three dimensional half-space [7].

where for the two-dimensional case

- $\mathbf{u}(\mathbf{x}, t) = \{u(\mathbf{x}, t), w(\mathbf{x}, t)\}$ represents the vector displacement of the half-plane particles and $\mathbf{x} = [x \ z]^T$,
- $\mu = \frac{E}{2(1+\nu)}$ (= second Lamé parameter or shear modulus),
- $\lambda = \frac{E\nu}{(1+\nu)(1-2\nu)} = K_b - \frac{2}{3}\mu$ (= first Lamé parameter).

Specific loading conditions can be taken into account by means of boundary and/or interface conditions that consider the normal and shear stresses. Using the tensor notation, the link between the displacement vector $\mathbf{u}(\mathbf{x}, t)$ and the stresses in the half-plane is made through the following stress-strain relationship for a continuum [5]:

$$\sigma_{ij} = \lambda \epsilon_{kk} \delta_{ij} + 2\mu \epsilon_{ij}, \tag{2.29}$$

where, for the two-dimensional case,

- $\sigma_{ij} = \begin{bmatrix} \sigma_{xx} & \sigma_{xz} \\ \sigma_{zx} & \sigma_{zz} \end{bmatrix}$,
- while application of the Einstein convention in combination with the kinematic relation that relates the strains to the displacements, gives $\epsilon_{kk} = \epsilon_{xx} + \epsilon_{zz} = \frac{\partial u}{\partial x} + \frac{\partial w}{\partial z}$, and

- $\epsilon_{ij} = \frac{1}{2}\left(\frac{\partial u_i}{\partial x_j} + \frac{\partial u_j}{\partial x_i}\right) = \begin{bmatrix} \epsilon_{xx} & \epsilon_{xz} \\ \epsilon_{zx} & \epsilon_{zz} \end{bmatrix}$.

Examples In what follows, two examples are presented to clarify how the response of the half-plane to specific loading conditions can be obtained. These examples are treated in more detail in the lecture notes on soil dynamics [5] and are presented in this chapter due to their later importance for the analyses in this report.

Example A If only a normal stress at the surface is applied as in fig. 2.12, and assuming that the loading does not vary in the horizontal direction, soil equation 2.28 reduces to the one-dimensional wave equation:

$$\rho \frac{\partial^2 w}{\partial t^2} = \left(\lambda + 2\mu\right) \frac{\partial^2 w}{\partial z^2}. \tag{2.30}$$

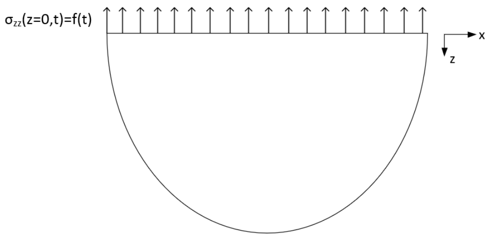

Figure 2.12: Two-dimensional half-plane loaded by a uniform normal stress at the surface [5].

As the direction of wave propagation (waves will propagate in the z-direction) is aligned with the direction of the particle motion (also in the z-direction), this type of wave is called a longitudinal wave. For this type of wave $\sigma_{xz} = \sigma_{zx} = 0$ and $\epsilon_{xz} = \epsilon_{zx} = 0$. Accordingly, the propagating waves will not cause shear deformation while the volume of the material does change when a wave passes by, as $\epsilon_{kk} = \frac{\partial w}{\partial z} \neq 0$. Therefore this wave is also referred to as a compressional wave and its motion is shown in the left picture in fig. 2.8.

Assuming zero initial conditions $\left(w(z,t=0) = \dot{w}(z,t=0) = 0\right)$, the Fourier transform with respect to time can be applied to eq. (2.30).

$$w(z,\omega) = \int_{-\infty}^{+\infty} w(z,t) \exp -\mathrm{i}\omega t \, dt. \tag{2.31}$$

This will eventually lead to the following equation in the space-frequency domain:

$$\begin{aligned} & \frac{d^2 w(z,\omega)}{dz^2} + \frac{\omega^2}{(\lambda + 2\mu)/\rho} w(z,\omega) \\ &= \frac{d^2 w(z,\omega)}{dz^2} + \frac{\omega^2}{c_L^2} w(z,\omega) \\ &= \frac{d^2 w(z,\omega)}{dz^2} + k_L^2 w(z,\omega) \\ &= 0, \end{aligned} \tag{2.32}$$

In the space-frequency domain, the general solution to eq. (2.32) is given by

$$w(z,\omega) = A \exp(-\mathrm{i}k_L z) + B \exp(\mathrm{i}k_L z). \tag{2.33}$$

Two boundary conditions are needed to find the value of the constants A and B and subsequently derive the half-plane response.

- **BC 1**: Radiation condition: no energy is coming from infinity, so no waves are propagating in the negative z-direction (=upwards) Based on eq. (2.33), the general solution in the space-time domain is defined as:

  $$\left[A\exp(-\mathrm{i}k_L z)+B\exp(\mathrm{i}k_L z)\right]\exp(\mathrm{i}\omega t).$$

  As will be explained in section 2.1.3, this means that the part $B\exp\left(\mathrm{i}(\omega t+k_L z)\right)$ is an upward propagating wave and thus B will have to be equal to zero: $B=0$.

- **BC 2**: $\sigma_{zz}(z=0,t)=f(t)$ in the time domain implies that $S_{zz}(z=0,\omega)=f(\omega)$ in the frequency domain. Considering relation 2.29, $\sigma_{zz}=\lambda\frac{\partial w(z,t)}{\partial z}+2\mu\frac{\partial w(z,t)}{\partial z}$ and thus:

  $$S_{zz}(z=0,\omega)=\left(\lambda+2\mu\right)\frac{dw(z=0,\omega)}{dz}=f(\omega).$$

  Based on this equation for the normal stress in the space-frequency domain, the expression for A is determined as

  $$A=\frac{f(\omega)}{\left(\lambda+2\mu\right)\left(-\mathrm{i}k_L\right)}.$$

Hence, in the space-frequency domain, the response will look like this:

$$w(z,\omega)=\left[\frac{1}{\left(\lambda+2\mu\right)\left(-\mathrm{i}k_L\right)}\exp(-\mathrm{i}k_L z)\right]f(\omega), \tag{2.34}$$

where the part between the square brackets is the transfer function as it transfers the load in the frequency domain to the displacement in the frequency domain. Normally, application of the inverse Fourier transform would result in the displacement in the space-time domain. However, in this case, because ω is present in the denominator of $w(z,\omega)$ (due to the presence of k_L), the velocity instead of the displacement in the space-time domain is to be determined, as integration over ω goes from $-\infty$ to $+\infty$ and thus at some point ω will be zero. The velocity in the frequency domain is easily derived as follows:

$$v(z,\omega)=\mathrm{i}\omega w(z,\omega)=\left[\frac{-c_L}{\lambda+2\mu}\exp(-\mathrm{i}\frac{\omega}{c_L}z)\right]f(\omega). \tag{2.35}$$

Now the part between the square brackets is the transfer function related to the velocity excited by the normal stress σ_{zz}. Application of the inverse Fourier transform to eq. (2.35) will give an expression for the vertical particle velocity in the space-time domain.

Example B When, instead of a normal stress, a shear stress is applied at the surface (see fig. 2.13) and again assuming that the loading does not change in the horizontal direction, only the horizontal particle displacement as a function of the z-coordinate will be different from zero. Again the soil equation 2.28 reduces to the one dimensional wave equation,

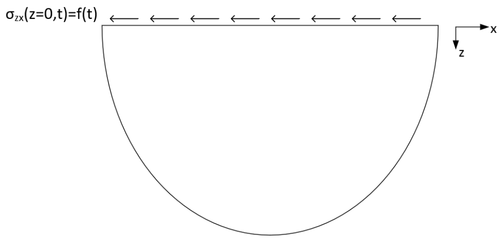

Figure 2.13: Two-dimensional half-plane loaded by a uniform shear stress at the surface [5].

but this time as a function of the variable $u(z,t)$ and with a different governing stiffness (μ instead of $(\lambda+2\mu)$):

$$\rho\frac{\partial^2 u}{\partial t^2} = \mu\frac{\partial^2 u}{\partial z^2}. \tag{2.36}$$

As the propagation direction (z-direction) of the waves is now perpendicular to the direction of motion of the particles (x-direction), the considered wave is referred to as a transverse wave. From eq. (2.29) it follows that $\sigma_{xz} = \sigma_{zx} \neq 0$, while $\sigma_{xx} = \sigma_{zz} = 0$ and thus the propagating wave will not change the volume of the material but it will cause shear deformation. Therefore, this wave is also called a shear wave and its motion is shown in the right picture in fig. 2.8.

The solution to eq. (2.36) is obtained in exactly the same way as for example A, but now the shear wave velocity, $c_T = \sqrt{\frac{\mu}{\rho}}$ and wavenumber of the shear wave, $k_T = \frac{\omega}{c_T}$ will be introduced.

HELMHOLTZ DECOMPOSITION

In the examples mentioned above, the soil equation could always be reduced to the one-dimensional wave equation. If this simplification is not possible however, eq. (2.28) for a two-dimensional half-plane are actually two coupled equations:

$$\rho\frac{\partial^2 u}{\partial t^2} = \mu\Big(\frac{\partial^2 u}{\partial x^2} + \frac{\partial^2 u}{\partial z^2}\Big) + (\lambda+\mu)\frac{\partial}{\partial x}\Big(\frac{\partial u}{\partial x} + \frac{\partial w}{\partial z}\Big), \quad \text{and} \tag{2.37a}$$

$$\rho\frac{\partial^2 w}{\partial t^2} = \mu\Big(\frac{\partial^2 w}{\partial x^2} + \frac{\partial^2 w}{\partial z^2}\Big) + (\lambda+\mu)\frac{\partial}{\partial z}\Big(\frac{\partial u}{\partial x} + \frac{\partial w}{\partial z}\Big). \tag{2.37b}$$

Helmholtz decomposition In this study, Helmholtz decomposition of a vector, as described in reference [5], will be used to decouple the equations and simplify their solving. For this purpose, the displacement vector $\mathbf{u}$ is written as a function of the scalar potential ϕ and the vector potential $\boldsymbol{\psi}$:

$$\mathbf{u} = \nabla\phi + \nabla\times\boldsymbol{\psi} \tag{2.38}$$

As ϕ is related to the divergence of $\mathbf{u}$ ($= \nabla\cdot\mathbf{u}$) it contains the compressional part of the particle motion. $\boldsymbol{\psi}$ on the other hand consists of the rotational part of the motion as it is related to the curl of $\mathbf{u}$ ($= \nabla\times\mathbf{u}$). For the two-dimensional case, the vector potential $\boldsymbol{\psi} = [0\ \psi_y\ 0]^T$, where only ψ_y is different from zero as both ψ_x (=rotation around the x-axis) and ψ_z (=rotation around the z-axis) would give displacements in the y-direction. Hereinafter ψ_y will simply be referred to as ψ. According to this reasoning, the components of the displacement vector are derived as

$$u = \frac{\partial\phi}{\partial x} - \frac{\partial\psi}{\partial z}, \quad \text{and} \tag{2.39a}$$

$$w = \frac{\partial\phi}{\partial z} + \frac{\partial\psi}{\partial x}. \tag{2.39b}$$

Substituting equations 2.39 in the coupled equations 2.37 results in the two following equations:

$$\frac{\partial}{\partial x}\boxed{\Big\{\rho\frac{\partial^2\phi}{\partial t^2} - (\lambda+2\mu)\Big(\frac{\partial^2\phi}{\partial x^2} + \frac{\partial^2\phi}{\partial z^2}\Big)\Big\}} - \frac{\partial}{\partial z}\boxed{\Big\{\rho\frac{\partial^2\psi}{\partial t^2} - \mu\Big(\frac{\partial^2\psi}{\partial x^2} + \frac{\partial^2\psi}{\partial z^2}\Big)\Big\}} = 0, \quad \text{and} \tag{2.40a}$$

$$\frac{\partial}{\partial z}\boxed{\Big\{\rho\frac{\partial^2\phi}{\partial t^2} - (\lambda+2\mu)\Big(\frac{\partial^2\phi}{\partial x^2} + \frac{\partial^2\phi}{\partial z^2}\Big)\Big\}} + \frac{\partial}{\partial x}\boxed{\Big\{\rho\frac{\partial^2\psi}{\partial t^2} - \mu\Big(\frac{\partial^2\psi}{\partial x^2} + \frac{\partial^2\psi}{\partial z^2}\Big)\Big\}} = 0 \tag{2.40b}$$

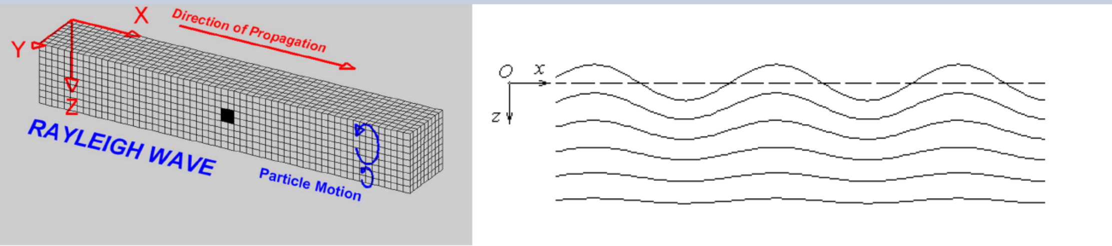

Figure 2.14: Rayleigh wave motion [5].

A convenient (albeit not unique) choice to solve eq. (2.40) is to set the equations in each of the boxes equal two zero. In this way, two uncoupled two-dimensional wave equations are obtained:

$$\frac{\partial^2 \phi}{\partial t^2} - c_L^2\left(\frac{\partial^2 \phi}{\partial x^2} + \frac{\partial^2 \phi}{\partial z^2}\right) = 0, \quad \text{and} \tag{2.41a}$$

$$\frac{\partial^2 \psi}{\partial t^2} - c_T^2\left(\frac{\partial^2 \psi}{\partial x^2} + \frac{\partial^2 \psi}{\partial z^2}\right) = 0, \tag{2.41b}$$

where eq. (2.41a) is related to compression and eq. (2.41b) to rotation.

When equations 2.39 are inserted into the stress-strain relationship for a continuum (eq. (2.29)), we find:

$$\begin{aligned} \sigma_{zz} &= \lambda\left(\frac{\partial^2 \phi}{\partial x^2} + \frac{\partial^2 \phi}{\partial z^2}\right) + 2\mu\left(\frac{\partial^2 \phi}{\partial z^2} + \frac{\partial^2 \psi}{\partial x \partial z}\right) \\ &= \mu\left(\frac{c_L^2}{c_T^2} - 2\right)\left(\frac{\partial^2 \phi}{\partial x^2} + \frac{\partial^2 \phi}{\partial z^2}\right) + 2\mu\left(\frac{\partial^2 \phi}{\partial z^2} + \frac{\partial^2 \psi}{\partial x \partial z}\right), \quad \text{and} \end{aligned} \tag{2.42a}$$

$$\sigma_{xz} = \mu\left(2\frac{\partial^2 \phi}{\partial x \partial z} + \frac{\partial^2 \psi}{\partial x^2} - \frac{\partial^2 \psi}{\partial z^2}\right). \tag{2.42b}$$

Example For a wave propagating at the surface of the half-plane, a reduction to the one-dimensional wave equation is not possible as such a wave propagates in the x-direction and its amplitude depends on the value of the z-co-ordinate. In that case, Helmholtz decomposition facilitates the solving of the problem. Surface waves at the surface of an elastic half-space are often referred to as "Rayleigh waves", as it was Lord Rayleigh who first described their properties [5]. Figure 2.14 shows the Rayleigh wave motion.

In order to find the horizontal and vertical soil particle displacement caused by such a wave, we start with a trial solution for the potentials ϕ and ψ in the same way as this is done when searching for the general solution for the vibration of a mass-spring system. However, the trial solution for ϕ and ψ will now not be a vibration but a wave propagating in the x-direction with a z-dependent amplitude, for example [5]:

$$\phi = F(z)\exp(\mathrm{i}(\omega t - kx)), \tag{2.43a}$$

$$\psi = J(z)\exp(\mathrm{i}(\omega t - kx)). \tag{2.43b}$$

Substituting eqs. (2.43a) and (2.43b) into eqs. (2.41a) and (2.41b) and subsequently applying the boundary conditions at infinity (radiation condition and decaying response when going to infinity) and at $z = 0$: $\sigma_{zz}(x, z = 0, t) = \sigma_{xz}(x, z = 0, t) = 0$, eventually leads to solutions for ϕ and ψ. The expressions for $u(x, z, t)$ and $w(x, z, t)$ can then easily be derived from eq. (2.39).

2.2. STATE-OF-THE-ART

THIS section reviews previous work that is relevant to the current project. The first section gives an overview of existing research into the way waves are radiated in the system of rail (or tube) and soil. The anomalous Doppler effect and its importance for the instability of vibrations of a moving vehicle is explained. Other sections include modelling options for trains moving on a rail or inside a tube embedded in the soil, the mathematical procedure to obtain a description of the vehicle vibrations which enables the instability analysis and the strategy to be employed for the instability analysis. Only analytical methods are discussed, as this project does not examine numerical methods for examining railway-induced vibrations, like for example the Finite Difference or Finite Element method. A last section introduces the reader to the concept of electrodynamic suspension systems using permanent magnets on the moving pods.

2.2.1. WAVES IN THE STRUCTURE

As mentioned in section 2.1.3, the relation between the frequency ω and the wavenumber k of waves that may be radiated in a structure is described by the dispersion relation. For a one-dimensional system, this relation is of the form $\omega = F(k)$ for $\omega, k \in \Re$ [8] In section 2.1.3 it is mentioned that the dispersion relation is a property of the elastic system and is independent of the moving load. Therefore, the dispersion relation is the real solution to the following equation:

$$\lim_{\mu^*,\lambda^*=0} \Delta(k,\omega) = 0, \tag{2.44}$$

where the material damping as well as the load are neglected. The determinant is obtained by substituting the general solution for the vertical and horizontal motion of the soil particles into the boundary and interface conditions for the model. When doing so, the terms related to a possible external load need to be neglected. The real solution to eq. (2.44) will lead to a curve in the k-ω-plane equivalent to the bold curve in fig. 2.10 where, instead of the radial frequency ω, the frequency in Herz, $f = \frac{\omega}{2\pi}$, is presented on the vertical axis. The minimum phase velocity, $v_{\mathrm{ph}}^{\min}$, of waves radiated in the structure is found as the slope of the line starting from the origin and tangent to this dispersion curve.

As discussed by Metrikine and Vrouwenvelder [8], waves which may propagate along the x-axis with a slight attenuation play an important role in the dynamic structural response. Mathematically, the dispersion curves for these waves may be found as the minima of $|\Delta(k,\omega)|$ for real k and ω. As explained by Veritchev [10], the wavenumbers of these waves for which the amplitude decays with the distance from the moving load, are complex-valued. Figure 2.15 depicts an example of the dispersion curve for non-attenuating waves (solid line) and of the dispersion curves for attenuated waves (dashed lines). The straight lines represent the Rayleigh wave velocity (c_R), the shear wave velocity (c_T) and the compressional wave velocity (c_L) in the soil.

Consider now a one-dimensional elastic medium where a harmonic wave propagates. The travelling of a point x at time t is expressed as:

$$w(x,t) = w_0 \exp\left(\mathrm{i}(\omega t - kx)\right), \tag{2.45}$$

where ω is the angular frequency of the wave and k is the wavenumber. As mentioned before, $(\omega t - kx)$ represents the phase of the wave. If now a point load is present which is travelling at a constant

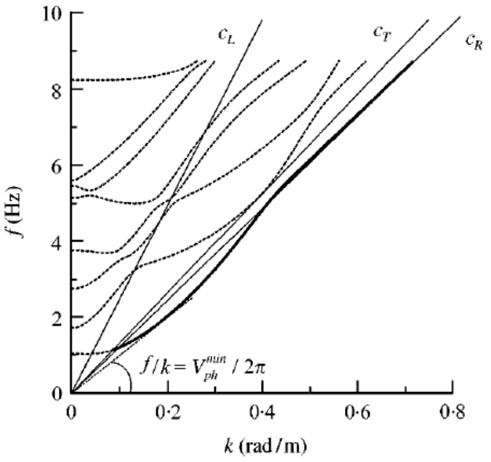

Figure 2.15: Dispersion curves [8].

speed V and vibrates at an angular frequency equal to Ω, the phase of vibrations of the moving load and the phase of the radiated waves at the point of loading will be equal [29]. At time t the load travelling with a speed V will be at $x = Vt$ and thus the following equation applies:

$$w(x = Vt, t) = w_0 \exp\left(\mathrm{i}(\omega t - kVt)\right) = w_0 \exp(\mathrm{i}\Omega t). \tag{2.46}$$

From eq. (2.46) the relation between the angular frequency of the radiated waves and that of the moving load can be derived as

$$\omega = kV + \Omega. \tag{2.47}$$

This equation represents the so-called kinematic invariant. When the frequency of the load is equal to zero, eq. (2.47) reduces to

$$\omega = kV. \tag{2.48}$$

Reference [8] states that in the latter case the phase velocity $v_{\mathrm{ph}} = \frac{\omega}{k}$ of all the waves that are radiated by the uniformly moving constant load must be equal to the velocity V of the load. Taking into account the formula for the phase velocity, eq. (2.47) can be written as

$$\omega = \frac{\Omega}{1 - \frac{V}{v_{\mathrm{ph}}}}. \tag{2.49}$$

As discussed in reference [30], this equation illustrates the Doppler effect as it proves that the frequency that is observed by a fixed observer is higher than the frequency of the moving load when V is positive and thus the load is travelling towards the observer. When, on the other hand, the load is moving away from a fixed observer, V changes sign and the denominator in eq. (2.49) becomes larger than unit. This means that the angular frequency perceived by the observer becomes lower than the frequency of the perturbation.

As shown by Metrikine [31], the oscillations of an object moving uniformly along the elastic one-dimensional system may be unstable when the velocity of the load is larger than the minimum phase velocity at which waves can be excited in a structure, $v_{\mathrm{ph}}^{\mathrm{min}}$. In that case, the waves excited by the moving load are the so-called anomalous Doppler waves which transfer the energy from the external source that maintains the uniform motion of the object into the energy of the vertical vibrations of the object [31]. Accordingly, instability may only take place when the moving load radiates anomalous Doppler waves [10].

The crossing points between the kinematic invariant and the dispersion curve determine the frequency and wavenumber of the waves perturbed by the moving load. Thus, to derive these frequencies and wavenumbers the solution to the following system of equations has to be found.

$$\begin{aligned} &\Delta(k,\omega) = 0, \\ &\omega = kV + \Omega. \end{aligned} \tag{2.50}$$

The solution of this system can be found graphically by using a graph similar to the one in fig. 2.16 [9, 10]. The two parabolas in fig. 2.16 are the dispersion curves. The straight lines represent the kinematic invariant. Their slope is equal to the velocity V of the moving load, while the point where these lines intersect the vertical axis, is defined by the frequency Ω of the load. For the case modelled in fig. 2.16, the frequency of the load is equal to zero. Line number one does not have any crossing points with the dispersion curve. The velocity V in this case is lower than the minimum phase velocity and the load will not radiate waves in the system. In the second case, the kinematic invariant has four crossing points with the dispersion curves. Therefore the load excites four waves with wavenumbers $k_1 \rightarrow k_4$. The radiation condition implies that waves should abstract energy from the moving object. As shown by Veritchev [10], this means that for waves propagating in front of the load ($x > Vt$) the group velocity ($v_{\text{gr}} = \frac{\partial\omega}{\partial k}$) should be larger than the velocity of the moving load V, while for waves propagating behind the load ($x < Vt$) the group velocity should be smaller than V. As derived from fig. 2.16 the waves with wavenumbers k_1 and k_3 travel in front of the moving load as in those points the slope of the dispersion curve is steeper than that of the kinematic invariant. According to the same reasoning, one can conclude that the waves with wavenumbers k_2 and k_4 propagate behind the load. Furthermore, for this velocity and frequency of the moving load, anomalous Doppler waves are excited. More specifically, waves with wavenumber k_1 and k_2 are normal Doppler as their frequency is higher than zero, while waves with wavenumber k_3 and k_4 are anomalous Doppler waves as their frequency is negative [31]. The third line for the kinematic invariant is tangent to the dispersion curve which means that $V = v_{\text{gr}} = \frac{\partial\omega}{\partial k}$ (assuming a real value of v_{gr}). For this combination of frequency Ω and velocity V, no energy is transported away from the load and therefore the structural displacement is infinite and resonance occurs.

2.2.2. MODELLING OPTIONS

To make the analysis of the instability of vibrations of a vehicle moving along a railway track or in a tube embedded in the soil possible, a model of the train and supporting structure needs to be defined. In what follows some of the different modelling options and the relevant literature studying these models will be described in more detail.

MODEL OF THE TRAIN

The moving train can be modelled in many different ways. Generally, two different approaches in modelling of the moving load are possible: one where the internal degrees of freedom (DOFs) of the load are neglected and the other approach where the load has its own DOFs [32].

When the internal DOFs of the moving load are neglected, it is represented by a moving point load $P(t)$, as is done in reference [8] and shown in fig. 2.17 where the load is moving on a beam on an elastic foundation. This way of modelling the load of the train on the structure may for example be adopted if the analysis focuses on the response of the structure itself rather than on the vehicle vibrations.

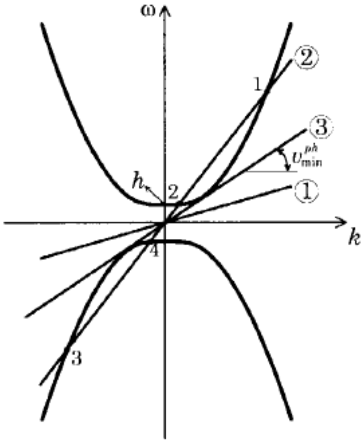

Figure 2.16: Graphical evaluation of frequencies and wavenumbers of waves perturbed by the moving load [9].

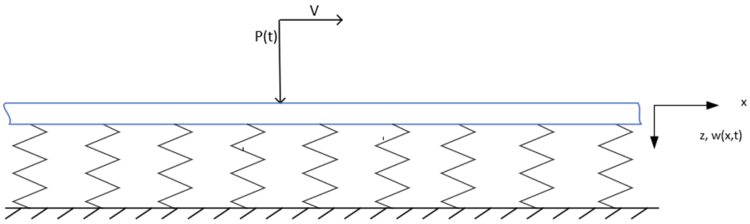

Figure 2.17: Point load along a beam moving at a constant velocity V on an elastic foundation.

As mentioned in reference [8], the load can be considered as a constant ($P(t) = P_0$) when the structural response to the constant pressure on the rails due to the gravity force is analyzed. When, on the other hand, the model should take certain frequencies of the loading spectrum into account, $P(t)$ should be modelled as a harmonic load. This way of modelling the load enables, for example, the study of the structural response as a function of the vehicle vibrations or, of the out-off-roundness of the wheels. An important distinction between the two loading models is that the kinematic invariant is different for both cases. As discussed earlier, when the load is moving at a constant velocity V and the frequency of the load is equal to zero, the kinematic invariant is described by eq. (2.48). When the point load $P(t)$ is harmonic with angular frequency Ω, eq. (2.47) defines the kinematic invariant.

From eq. (2.47) it can be seen that the harmonic load may radiate waves from much lower load velocities than the constant load. Even when the velocity of the harmonic load is equal to zero, it may still radiate waves as wave radiation by the load takes place when the kinematic invariant crosses the dispersion curve or the curves representing the attenuated waves (see section 2.2.1) [8].

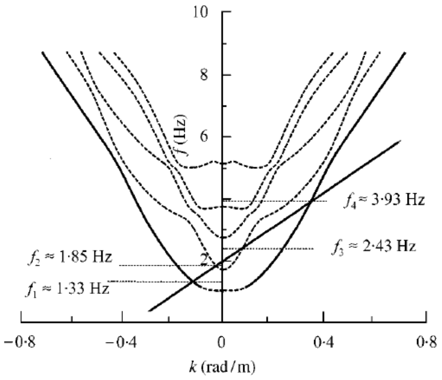

Figure 2.18: Kinematic invariant crossing the dispersion curves for load velocity V smaller than $v_{\text{ph}}^{\text{min}}$ and load vibrating at a frequency $\Omega \neq 0$ [8].

Figure 2.18 gives a good illustration of this fact. As the slope of the kinematic invariant is clearly smaller than the slope of the bold dispersion curve (= dispersion curve for non-attenuating waves), the load velocity V is smaller than $v_{\text{ph}}^{\text{min}}$. However, as the load vibrates at a frequency Ω (= crossing point with the vertical frequency axis), it will still radiate waves in the structure. Metrikine and Vrouwenvelder [8] have shown that when the frequency of the vehicle vibrations is larger than the cut-off frequency, waves will always be excited, even if the vehicle is not moving.

In reality, the structure is subject to a wide variety of loads. The response to a wide loading spectrum can be examined by modelling the vehicle as a random function of time. The effect of a random load on surface ground vibrations has been analyzed by Metrikine and Vrouwenvelder [8].

When the instability of vibrations of the vehicle is under investigation, the internal degrees of freedom of the vehicle should be considered. In this case the contact force between the moving load and the elastic system is not prescribed, but instead has to be determined by considering the interaction between the load and the system [32]. Metrikine *et al.* [20] and Denisov *et al.* [33] examine the instability of vibrations of a single mass moving uniformly along a beam. The vehicle may also be modelled as an oscillator moving on the railway track. In this case, many different modelling options are available. References [9, 10, 13] investigate the stability of vibrations of one single mass moving oscillator, while the vibrations of one two-mass oscillator are studied in papers [10, 12, 32]. A two-oscillator model of the vehicle is considered by Wolfert *et al.* [9, 11]. The theory developed for two oscillators may be extended to the case of a chain of oscillators. Veritchev [10] refines the model with the two moving oscillators by studying the instability of vibrations of a bogie modelled as a rigid bar supported by two identical supports, each consisting of a spring-damper system. Figure 2.19 visualizes the cases of the single mass, the one- and two-mass single oscillator, the double moving oscillator and the bogie.

In fact, the cases of the single mass (fig. 2.19a) and that of the one-mass single oscillator (fig. 2.19b) moving uniformly along a track are simplifications of the case where a two-mass single oscillator is

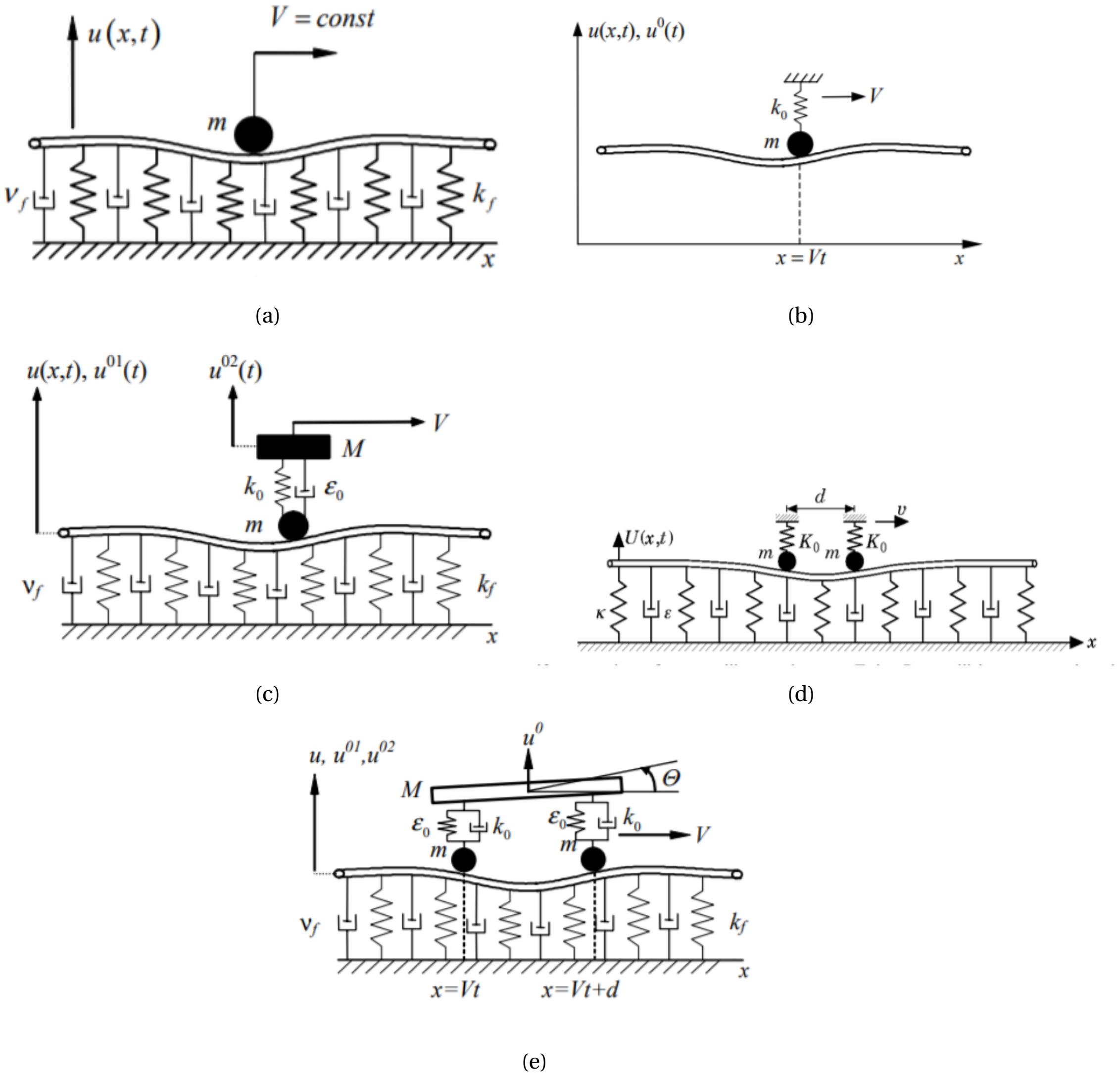

Figure 2.19: Different modelling options for the moving vehicle: (a) Uniformly moving single mass [10], (b) Uniformly moving one-mass oscillator [10], (c) Uniformly moving two-mass oscillator [10], (d) Uniformly moving double oscillator [11] and (e) Uniformly moving bogie supported by two identical oscillators [10].

considered. In the model with the moving mass, the values of the second mass, the spring stiffness and the damping coefficient of the two-mass oscillator are taken equal to zero. When examining the instability of vibrations of a one-mass single oscillator, the magnitude of the second mass is neglected. When only the single mass is studied, the instability regions as a function of the mass magnitude and the effect of the stiffness and viscosity of the supporting structure can be derived. Modelling the vehicle as a moving oscillator enables the evaluation of the effect of the stiffness and viscosity of the oscillator on the instability zone [10]. The advantage of modelling the train as a two degree of freedom system rather than as a one-mass moving oscillator, lies in the fact that the two-mass oscillator model takes into account the weight and dynamic behaviour of the supports as well as that of the train itself. The model of the bogie is the most sophisticated one, taking into account the reality that the supports of the vehicle do not only interact through the track the vehicle is moving on, but also by means of the bogie that connects the supports. The moment of inertia of the bogie now appears as an extra degree of freedom. The bogie as well as the double oscillator model permit analysis of the effect of the size of the wheelbase (= parameter d in fig. 2.19) on the system's stability [10].

MODEL OF THE SUPPORTING STRUCTURE

The structure the load is moving on can either be analyzed as a finite-length structure, or as an infinitely long structure. When, for example, the response of a railway bridge is analyzed, the bridge on which the load is moving is modelled as a finite length element. However, for the examination of the dynamic behaviour of a long underground tube embedded in the soil or of an open-field railway track the infinitely long structure is better suited [32]. Therefore, the discussion in this paper will only be limited to that of a load moving along an infinitely long structure.

Many existing papers on instability of a vehicle moving along an infinitely long structure employ a one-dimensional homogeneous model of the railway track ([9, 11, 20, 32, 34–37]). References [12, 13, 21] however adopt a three-dimensional model for the supporting structure, while the inhomogeneity of the track is taken into account in papers [10, 38].
The main advantage of the one-dimensional models is their simplicity. Nevertheless, as shown in papers [10, 12], these 1D models of the track underestimate the velocity at which the vibrations of the vehicle become unstable. Therefore, the one-dimensional models are only able to qualitatively estimate the instability domain. A quantitatively accurate estimation of the instability domain for the vehicle velocity is only achievable when the properties of the supporting structure are accounted for. In practice the rails are often not homogeneous, for example due to the corrugation of rails. Moreover, a realistic model of the foundation should take into account its inhomogeneity as well. Veritchev [10] studies the effect of a periodic inhomogeneity of the supporting structure on the stability of the moving vehicle. He concludes that parametric instability may occur at any non-zero velocity when taking into account this inhomogeneity and not only when the vehicle velocity exceeds the minimum phase velocity as is the case for a vehicle moving on a homogeneous structure. Jones [39] pointed out that when the inhomogeneity of the soil is accounted for and the soil is for example modelled as a layered half-space, analytical methods for the analysis of the system's stability lack the flexibility to investigate such complex scenarios. Semi-analytical methods and discrete numerical methods have proven to be more suited for modelling the complex soil structure [39].

When using the model of a beam as a simplistic model for the rails (or tube), the choice that remains is whether the shear deformation of the beam will be taken into account or not. In the first case the beam is modelled as a Timoshenko beam, while in the latter case it is represented by an Euler-Bernoulli beam. The Timoshenko beam model is the more accurate one. Nonetheless, as the ratio of the length to the thickness of the track or tube is very large, it has been shown that the the Euler-Bernoulli beam is applicable if instability occurs for low frequencies [10].

With respect to the foundation, there are many different modelling options. The simplest foundation models are the one-dimensional elastic and visco-elastic foundation as described in section 2.1.1. However, as these models don't take into account the subsoil of the track and the phase velocity of waves in a railway track is strongly influenced by this subsoil, they can not give a reasonable estimation of the vehicle velocity at which unstable vibrations may emerge [10].

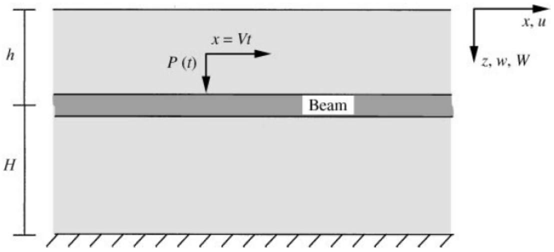

Figure 2.20: Example of a foundation modelled as a 2D soil layer with a fixed lower boundary [8].

More realistic models take into account the soil parameters and wave propagation in the soil by modelling the foundation as a soil layer (see the example in fig. 2.20) or as a half-space (see fig. 2.11). The difference between both is that the soil layer has a fixed boundary at a certain depth and thus, waves will be reflected at this boundary. The half-space on the other hand is assumed to extend towards infinity and no waves can be reflected from infinity upward. The model of the 3D half-space can be simplified by neglecting the out-of-plane dimension and studying the subsoil as a two-dimensional model. figs. 2.12 and 2.13 visualize such a half-plane.

When modelling the subsoil as a layer or as a half-space (or half-plane) the rail can either be modelled as a beam placed on top of the foundation or as a tube embedded in the foundation.

As shown by Metrikine and Dieterman [21], the two- or three-dimensional models can be reduced to a one-dimensional model by deriving an equivalent stiffness of the subsoil interacting with the beam. In the next section this procedure will be explained.

The soil can either be assumed to be elastic or the viscosity can be accounted for by including material damping parameters in the model. The latter option will produce the more realistic estimation of the instability region.

2.2.3. PROCEDURE FOR STUDYING THE INSTABILITY OF VIBRATIONS OF A VEHICLE

Once the model of the moving vehicle inside the tube embedded in the soil has been described, a mathematical procedure needs to be applied to eventually be able to analyze the instability of the vehicle's vibrations. As discussed in section 2.1.1, this instability depends on the roots of the characteristic equation. In what follows, the procedure for deriving the characteristic equation is explained step by step. This procedure is employed in existing papers and summarized by Veritchev in [10].

1) **Mathematical description of the model** For the description of the interaction of a moving vehicle with the elastic structure, three components are necessary: the partial differential equation(s) describing the motion of the supporting structure, the ordinary differential equation(s) governing the motion of the moving vehicle and the boundary and interface conditions defining the interaction between the vehicle, the beam and the foundation. For the formulation of the boundary conditions that describe the vehicle-structure interaction, the Dirac delta function is usually applied to fix the position of the loading point and connect the point load(s) representing the moving vehicle to the elastic structure. Therefore, the Dirac delta function is included in the right-hand side of the equation of motion for the beam. In case of a 3D model, the Heaviside step function is commonly introduced to account for the finite width of the beam. As the model is only a simplification of the reality, assumptions concerning the supporting structure and the moving vehicle have to be made before the equations of motion can be determined (see for example the assumptions in [12, 13]).

2) **Introduction of a moving reference system** In case of a moving load, the Dirac delta function

that is used to describe the interaction between the vehicle and its supporting structure in the loading point, depends both on the time t and on the horizontal spatial co-ordinate x. As clearly explained in reference [10], it is customary to introduce a reference system that is fixed to the moving vehicle and thus moves at the velocity of the vehicle. For a three-dimensional model this reference system is defined as follows [12, 13]:

$$\begin{cases} \xi &= x - Vt, \\ y &= y, \\ z &= z, \\ \tau &= t, \end{cases}$$

where V is the velocity of the moving vehicle. The advantage of the introduction of such a reference system is that the Dirac delta function no longer depends on the time t and, as a result, the application of the inverse Laplace transform can be avoided when deriving the characteristic equation.

3) **Application of the Laplace and Fourier integral transform** As mentioned in section 2.1.2, the Laplace and Fourier transforms facilitate the reduction of partial differential equations to ordinary differential equations and even simple algebraic equations. They can be applied as long as a linear statement of the equations of motion, boundary and interface conditions is adopted. As depicted in eq. (2.20), the Laplace transform with respect to time introduces the eigenvalues s of the problem and has to be applied rather than the Fourier transform with respect to time when the instability phenomenon is studied. As shown in references [8, 10, 12, 13, 20, 32], the Fourier transform is applied with respect to the horizontal space co-ordinates (x and y in case of a 3D model, x in case of a 1D or 2D model). Equation (2.14) gives the expression for the forward Fourier transform with respect to x that introduces the wavenumber into the problem. After applying both the Laplace transform with respect to time and the Fourier transform with respect to the horizontal spatial co-ordinates, all differential equations are reduced to algebraic ones for a one-dimensional model, while for two- and three dimensional models only the derivatives with respect to the vertical co-ordinate remain.

4) **Reduction to a one-dimensional model by solving in the Laplace-Fourier domain and derivation of the equivalent stiffness of the foundation** In the papers that study the instability of vehicle vibrations and adopt a three-dimensional model for the supporting structure ([12, 13], the model, usually a half-space, is reduced to a one-dimensional model comparable to that of an infinite beam on an elastic foundation as depicted in fig. 2.7. To obtain such a model, the equivalent stiffness of the half-space interacting with the beam needs to be derived. As outlined in [21], this equivalent stiffness can be determined by first finding the general solution to the equations describing the half-space motion in the Laplace-Fourier domain. Then the equivalent stiffness of the half-space is identified by expressing the motion of the infinitely long beam on the half-space in the Laplace-Fourier domain and comparing it to the description for the motion of the same beam resting on a Winkler foundation. Equation (2.51) describes the displacement of the beam on the elastic foundation with stiffness χ in the Laplace-wavenumber domain for the case where no loading is applied.

$$v_b(k,s)\big(D(k,s)+\chi\big)=0. \tag{2.51}$$

In this equation, $D(k,s) = m_\mathrm{b}s^2 + EIk^4 = 0$ is the dispersion relation for bending waves in an Euler-Bernoulli beam with $s = \mathrm{i}\Omega$ [21]. The derivation of the expression for the beam displacement for the case where the beam is loaded by an uniformly moving two-mass oscillator is given in appendix A.

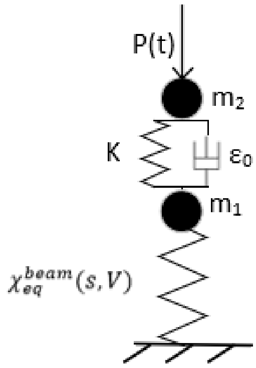

Figure 2.21: Equivalent lumped model for the vertical vibrations of the oscillator [12].

5) **Reduction to a lumped model by applying the inverse Fourier transform and derivation of the characteristic equation** In a last step towards finding the characteristic equation, the one-dimensional model is further reduced to a lumped model for which the motion is only a function of time and no longer of the spatial co-ordinates. For the case where the beam is loaded by a two-mass oscillator, the lumped model is depicted in fig. 2.21. To derive an equation that describes the oscillator motion as a function of time, in a first step, the vertical motion of the beam is transformed to the Laplace-space domain by applying the inverse Fourier transform on $v_b(k,s)$. The description of the behaviour of the lumped mass-spring-dashpot model is then obtained by accounting for the fact that the displacement of the lower mass m_1 and of the beam are equal at the location of the oscillator. The resulting equation is only a function of the eigenvalues s of the problem. In fig. 2.21 the reaction of the beam-half-space system in the point of contact with the load is reflected by a spring with frequency-and velocity-dependent complex stiffness $\chi_{\mathrm{eq}}^{\mathrm{beam}}(s,V)$. The value of this equivalent dynamic stiffness can be derived from the equation describing the vertical motion of the oscillator [10, 12]. Finally the characteristic equation for the vibrations of the oscillator is obtained by combining the equation of motion for the upper mass in the Laplace domain with the equation describing the motion of the oscillator in the lumped model.

2.2.4. INSTABILITY ANALYSIS

In the approach adopted in references [12, 13, 20, 35], the stability analysis starts by studying the equivalent dynamic stiffness $\chi_{\mathrm{eq}}^{\mathrm{beam}}$, which reflects the reaction of the elastic system in the contact point with the moving load. The reason for this is that instability may only arise when the imaginary part of $\chi_{\mathrm{eq}}^{\mathrm{beam}}$ is negative, as this means that the equivalent spring has a 'negative viscosity'. In this case the velocity of the oscillator exceeds the minimum phase velocity of waves in the structure and anomalous Doppler waves are excited by the moving oscillator. If, for a certain load velocity, $\Im(\chi_{\mathrm{eq}}^{\mathrm{beam}}) > 0$ for all frequencies, the oscillator vibrations are unconditionally stable. However, as mentioned in [10], the existence of a frequency band where the imaginary part of the equivalent stiffness is negative, is a necessary, but not a sufficient condition for unstable oscillator vibrations to occur. As discussed earlier, the roots of the characteristic equation have to be studied to make a judgment about the instability. When at least one of these roots has a positive real part, unstable vehicle vibrations will arise.

Because the characteristic equation contains an integral due to the presence of $\chi_{\mathrm{eq}}^{\mathrm{beam}}$, it is difficult to determine its roots directly. Therefore, the approach proposed in papers [8, 9, 13, 20, 32] will be followed in this study. Analogously with this approach, the study of the stability will be accomplished using the D-decomposition method [33]. The latter employs the fact that the imaginary axis of the complex s-plane separates the field where s has a negative real part (the 'stable' values for s) from that where the eigenvalues have a positive real part (the 'unstable' values for s). In other words, the axis $\mathrm{i}\Omega$ marks the border between stability and instability as has been visualized in fig. 2.22.

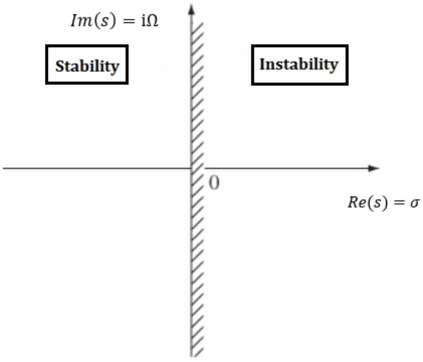

Figure 2.22: Visualization of the complex s-plane.

In the D-decomposition method, the imaginary axis of the complex s-plane is mapped onto the plane of one of the system parameters, which, for this purpose, should be considered as complex-valued. The frequency Ω is used as the parameter for the mapping. More specifically, the studied complex parameter 'Q' first has to be written as a function of the frequency Ω by rewriting the characteristic equation and replacing s by $\mathrm{i}\Omega$. Then the real and imaginary part of 'Q' have to be determined for real values of $\Omega \in [-\infty \ +\infty]$. The D-decomposition curve plots $\Im(Q)$ versus $\Re(Q)$ and this mapped line separates the plane of the observed complex parameter into domains with a different number of unstable roots (=roots with a positive real part). As is done in fig. 2.22, the side of the D-decomposition curve corresponding to the right-hand side of the $\Im(s)$-axis is shaded, which means that crossing the mapped line in the direction of the shading results in one more root with a positive real part. Figure 2.23a gives an example of the D-decomposition of the complex K-plane where K is the parameter representing the stiffness of the oscillator spring and n is the number of unstable roots for each domain.

Finally, based on the D-decomposition of the complex parameter, an instability domain can be derived for this parameter. For the given velocity range, this instability region plots the value of the parameter where unstable vibrations first occur. In a parametric study, the effect of varying the model parameters on the instability domain is investigated. Figure 2.23b shows an example of the instability domain for the stiffness of a two-mass oscillator.

2.2.5. THE PERMANENT MAGNET ELECTRODYNAMIC SUSPENSION SYSTEM

As denoted in reference [15], the Hyperloop pods are suspended using a non-contact suspension system. This suspension system consists of Halbach arrays of permanent magnets in the bogies of the vehicle. The test track is a solid conductive plate, but a significant decrease in electromagnetic drag could be achieved when opting for the Inductrack instead [15]. Therefore, the existing literature on this type of track, in combination with Halbach arrays on the vehicle is reviewed in this section.

The Inductrack is a magnetic levitation system that has been developed at the Lawrence Livermore National Laboratory for use in maglev trains. While previous EDS systems employ cryogenically cooled superconducting magnets on the moving vehicle, the Inductrack uses unpowered loops of wire and permanent Halbach magnet arrays on the train to realize magnetic levitation. As explained by Post and Ryutov in [40], the system is passively stable as it only requires motion and no electromagnets or control circuits to maintain stable levitation. Moreover, the system is fail-safe as failure of the

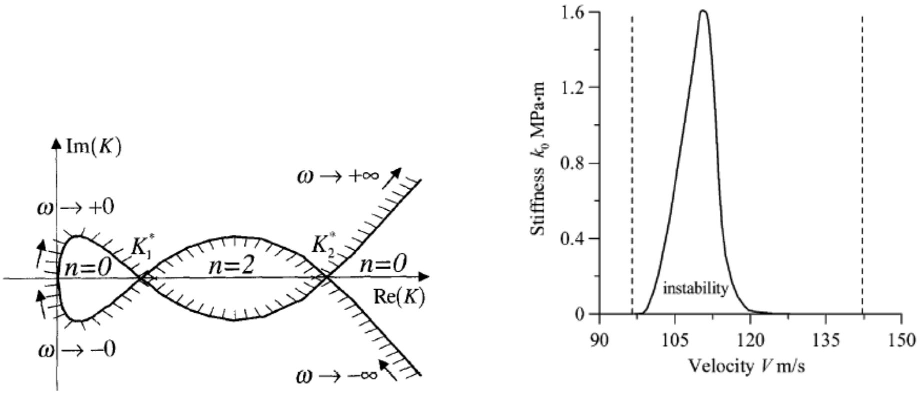

(a) (b)

Figure 2.23: Example of (a) D-decomposition of the complex K-plane with n the number of unstable roots per domain [13] and (b) instability domain for the stiffness k_0 of a moving two-mass oscillator [12].

power system only causes the pod to slow down and move at low speed on the auxiliary wheels before stopping.

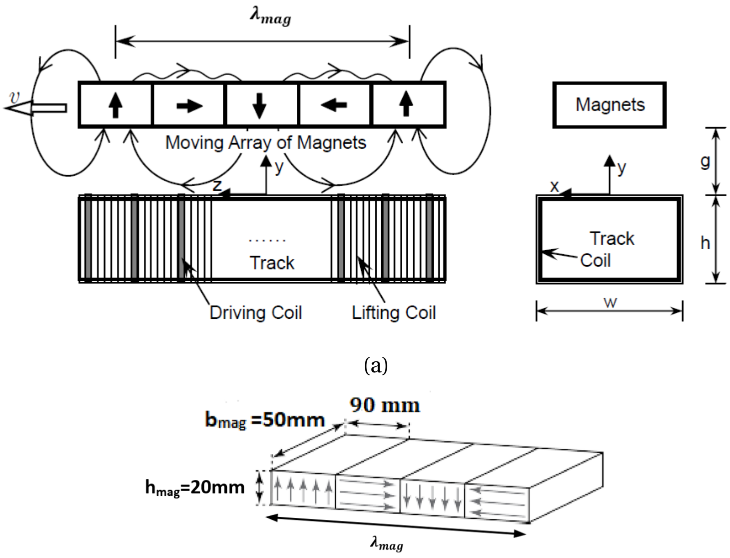

(a)

(b)

Figure 2.24: Configuration of the magnetic levitation system: (a) the Inductrack system [14], (b) Lift magnet Halbach array used for the Hyperloop competition pod consisting of 4 permanent magnets. The arrows denote the different polarizations of each magnet [15].

In the Halbach array, permanent magnets in different polarizations are combined to create a sinusoidally-like periodic magnetic field that is amplified below the array, while almost canceling it above the array [15, 40]. Figure 2.24 depicts the configuration of the Inductrack system as well as a schematic drawing of the lift magnets employed on the Hyperloop competition pods. As the magnet array passes over the multi-loops of wire in the track, it induces a current in them.

This way the magnets and coils create an electromagnetic field which repels the permanent magnets. When the pod moves, the change in the magnetic field causes an electromagnetic force [14, 41].

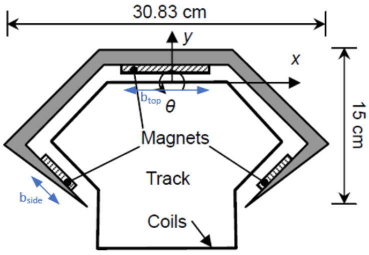

Figure 2.25: Inductrack model with maglev train. Top and side magnet arrays are attached at the bottom of the train [14].

Kim and Ge [14] have formulated an expression for the levitation force on a maglev train produced by the Inductrack system. The configuration of such a train on a track made out of shorted circular loops is shown in fig. 2.25. In the Inductrack system the levitation force depends both on the velocity of the cradle, which is assumed to be uniform, and on the gap between the track and the vehicle. Due to the vibrations of the vehicle this gap changes as the train moves. For the model in fig. 2.25, the lift force is written as [14]

$$F_{\text{lift}}(V, g_1) = \left(b_{\text{top}} \exp\left(-k_{\text{mag}} g_1\right) - \sqrt{2} b_{\text{side}} \exp\left(-k_{\text{mag}} g_2\right)\right) \cdot 2N_c \frac{B_0 \phi_0}{2L} \frac{1}{1 + \left(\frac{R}{\omega_{\text{mag}} L}\right)^2}, \tag{2.52}$$

with

$$\phi_0 = \frac{b_{\text{mag}} B_0}{k_{\text{mag}}} \exp\left(k_{\text{mag}} g_{\text{nom}}\right) \qquad [m^2 T]. \tag{2.53}$$

The angular frequency of the magnetic field due to the motion of the vehicle is determined by $\omega_{\text{mag}} = k_{\text{mag}} V$, where V is the uniform vehicle velocity. Typically, the peak strength of the magnetic field at the surface of the Halbach arrays, B_0, has a magnitude of about one T (=Tesla) for NdFeB magnets [40], which are generally used on the Hyperloop pods. The inductance and resistance are properties of the track and can be derived from the following expressions [40]:

$$L = \frac{\mu_0 P_c}{2 k_{\text{mag}} d_c}, \tag{2.54a}$$

$$R = \frac{\rho_r P_c}{A_c}. \tag{2.54b}$$

The definition of the symbols in eqs. (2.52), (2.53), (2.54a) and (2.54b) is given in the glossary. The term with b_{side} is present in eq. (2.52) because, for the maglev trains in the Inductrack system, the arrays at the top cause a positive levitation force, while the arrays at the side reduce this force. Furthermore, the number of lifting coils in the track per wavelength (= N_c) is multiplied by two because there are two sets of Halbach arrays per maglev train in the Inductrack system [14].

Figure 2.26a presents an exploded view of the Hyperloop competition vehicle designed by Delft Hyperloop. A detail of the vehicle suspension is depicted in fig. 2.26b, while fig. 2.26c shows the configuration of the lifting bogie. The bogies are connected to the vehicle body by means of a spring damper system. The final design document of the Hyperloop competition pod [15] states that the heaving motion of the lifting magnets is uncoupled from the lateral stabilization magnets for sway. Thus, for the Hyperloop pod, the side magnets do not influence the levitation force. Moreover, each

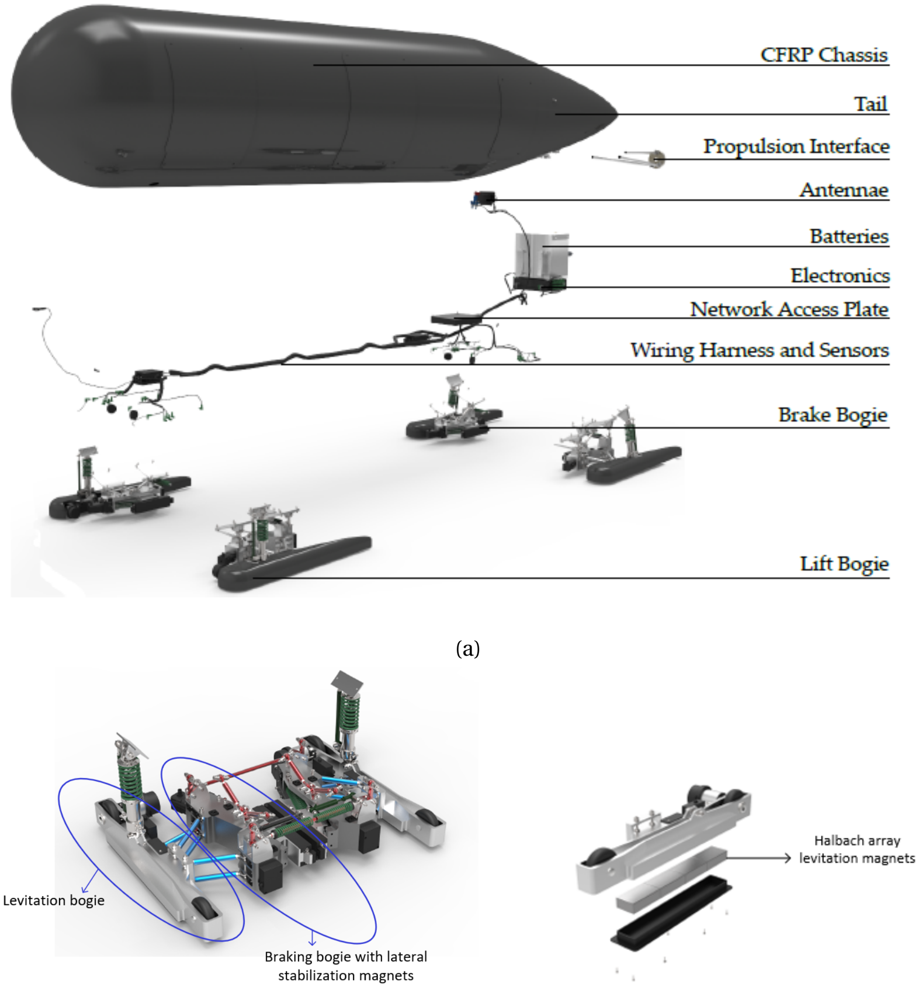

(a)

(b) (c)

Figure 2.26: Overview of the configuration of the Hyperloop vehicle with (a) an exploded view of the Hyperloop pod, (b) a detail of the suspension system and (c) an exploded view of the levitation bogie with Halbach array of permanent magnets. The blue and red rods cause the heaving motion to be completely uncoupled from the braking motion in sway [15].

Hyperloop vehicle has four Halbach arrays (as opposed to two arrays per train in the case of the maglev trains). Based on this distinction between the Hyperloop pod and the maglev train, the adapted lifting force for the Hyperloop vehicle on a rail with coils in it reads

$$F_{\text{lift}}(V, g_1) = 4 * b_{\text{mag}} N_c \frac{B_0 \phi_0}{2L} \frac{1}{1 + (\frac{R}{\omega_{\text{mag}} L})^2} \exp(-k_{\text{mag}} g_1). \tag{2.55}$$

According to reference [14], this levitation force can be introduced in the model by adding a nonlinear spring.

3

MODELS AND DESCRIPTION OF MOTION

The reality of a moving pod in a near vacuum underground tube is modelled to make the analysis of vibrations of the vehicle possible. This chapter describes the chosen vehicle-tube-soil model as well as the equations that govern the motion of its components. To find a solution to these equations, boundary and interface conditions are determined. Since the considered model is linear, Fourier and Laplace integral transforms are employed to simplify the partial differential equations and facilitate the analysis. Eventually, the derivation of the equivalent soil stiffness and, subsequently, of the equivalent dynamic stiffness of the underground beam at the location of the contact point with the moving vehicle results in the description of the pod's vertical vibrations in the form of the equation of motion for a simple mass-spring system. This equation delivers the characteristic equation of which the roots need to be studied for the stability analysis in chapter 4.

3.1. MODEL OF THE VEHICLE-TUBE-SOIL SYSTEM

FIGURE 3.1 shows the model of the vehicle-tunnel-soil system that will be adopted for this research.

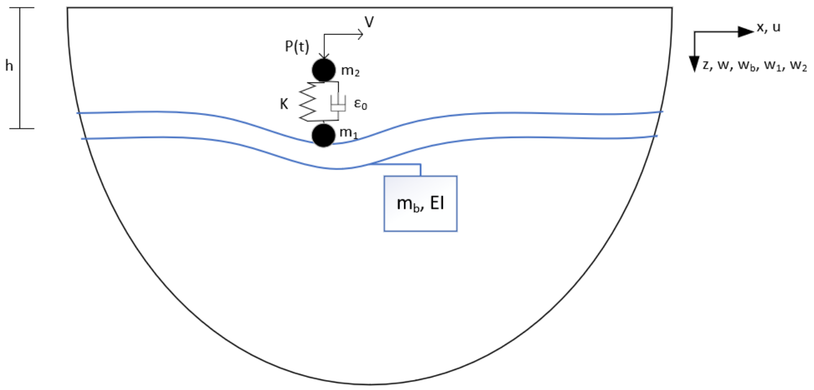

Figure 3.1: Vehicle-tube-soil model.

The soil is modelled as a two-dimensional visco-elastic half-plane. This means that there is no fixed bottom and thus z goes to infinity. The tube is represented by an infinitely long Euler-Bernoulli beam with a mass per unit length and flexural rigidity equal to m_b and EI respectively. The tube is located at a depth h from the ground surface. A two-mass oscillator describes the motion of the moving pod. This oscillator vibrates vertically and moves along the beam with a constant velocity V. As depicted in figure 3.1, m_1 and m_2 are the lower and upper masses of the oscillator respectively. K and ϵ_0 are the oscillator's stiffness and viscous damping. The upper mass of the oscillator is loaded by the harmonic load $P(t) = P_0 \cos(\Omega t)$.

For this study the following assumptions are adopted [8, 12]:

1. the half-plane is visco-elastic, isotropic and homogeneous,
2. the surface is not loaded and it is traction-free,
3. the beam does not move horizontally,
4. the beam is assumed to be slender and the interface between beam and half-plane is defined at $z = h \pm 0$,
5. the displacements of beam and half-plane are equal at the interfaces $z = h \pm 0$,
6. the vertical displacements of the lower mass and the beam are equal at the interfaces $z = h \pm 0$.

3.2. EOM, BC AND IC IN THE TIME-SPACE DOMAIN

BASED on the model described in section 3.1, the equations of motion (EOM) characterizing the behaviour of the vehicle-tube-soil system are derived. In first instance these equations describe the motion in the time (t)-space (x,z) domain. Definition of the boundary conditions (BC) and interface conditions (IC) completes the problem statement. As in the approach adopted in references [12, 13, 20], once the governing equations of motion and conditions are determined, a moving reference system is introduced and all equations are transformed into this reference system which moves along the x-direction with the constant velocity of the oscillator.

3.2.1. EOM, BC AND IC IN THE X,Z-REFERENCE SYSTEM

EOM FOR THE HALF-PLANE

Taking into account the material damping in the half-plane and based on eq. (2.28) , the motion of the half-plane is obtained as [8]

$$\hat{\mu}\nabla^2 \boldsymbol{u} + (\hat{\lambda} + \hat{\mu})\nabla(\nabla \cdot \boldsymbol{u}) = \rho \frac{\partial^2 \boldsymbol{u}}{\partial t^2}, \tag{3.1}$$

where $\hat{\lambda}$ and $\hat{\mu}$ are used instead of the Lamé parameters in order to take into account the material damping in the half-plane. Therefore, $\hat{\lambda} = \lambda + \lambda^* \frac{\partial}{\partial t}$ and $\hat{\mu} = \mu + \mu^* \frac{\partial}{\partial t}$, where the terms $\lambda^* \frac{\partial}{\partial t}$ and $\mu^* \frac{\partial}{\partial t}$ describe the viscosity of the half-plane.

The vector form of the equations of motion for the half-plane (equation (3.1)) are in fact coupled equations. As discussed in section 2.1.4, Helmholtz decomposition is applied to decouple the equations by describing the half-plane motion in terms of the Lamé potentials ϕ and $\boldsymbol{\psi}$. The components of the displacement vector **u** are

$$u = \frac{\partial \phi}{\partial x} - \frac{\partial \psi}{\partial z}, \quad \text{and} \tag{3.2a}$$

$$w = \frac{\partial \phi}{\partial z} + \frac{\partial \psi}{\partial x}. \tag{3.2b}$$

The expressions (3.2a) and (3.2b) are inserted in the equation of motion for the continuum (3.1). This gives the following two decoupled equations in terms of ϕ and ψ:

$$\frac{\partial^2\phi}{\partial t^2} - \big(c_L^2 + \frac{\lambda^* + 2\mu^*}{\rho}\frac{\partial}{\partial t}\big)\big(\frac{\partial^2\phi}{\partial x^2} + \frac{\partial^2\phi}{\partial z^2}\big) = 0, \quad \text{and} \tag{3.3a}$$

$$\frac{\partial^2\psi}{\partial t^2} - \big(c_T^2 + \frac{\mu^*}{\rho}\frac{\partial}{\partial t}\big)\big(\frac{\partial^2\psi}{\partial x^2} + \frac{\partial^2\psi}{\partial z^2}\big) = 0, \tag{3.3b}$$

where:

$$c_L = \sqrt{\frac{\lambda + 2\mu}{\rho}}, \quad \text{and} \tag{3.4a}$$

$$c_T = \sqrt{\frac{\mu}{\rho}}. \tag{3.4b}$$

As the vertical stress, σ_{zz}, and shear stress, σ_{xz}, in the soil are also a function of the horizontal and vertical soil particle motion, their potential form is used in this study. The expressions for σ_{zz} and σ_{xz} in terms of potentials are derived in section 2.1.4. When taking into account the viscosity of the half-plane and eliminating λ from the equation for σ_{zz}, these equations are

$$\sigma_{zz}(x,z,t) = \big(\mu + \mu^*\frac{\partial}{\partial t}\big)\big(\frac{c_L^2}{c_T^2} - 2\big)\big(\frac{\partial^2\phi}{\partial x^2} + \frac{\partial^2\phi}{\partial z^2}\big) + 2\big(\mu + \mu^*\frac{\partial}{\partial t}\big)\big(\frac{\partial^2\phi}{\partial z^2} + \frac{\partial^2\psi}{\partial x\partial z}\big), \quad \text{and} \tag{3.5a}$$

$$\sigma_{xz}(x,z,t) = \big(\mu + \mu^*\frac{\partial}{\partial t}\big)\big(2\frac{\partial^2\phi}{\partial x\partial z} + \frac{\partial^2\psi}{\partial x^2} - \frac{\partial^2\psi}{\partial z^2}\big) \tag{3.5b}$$

EOM FOR THE BEAM

The equation that describes the vertical motion of the infinitely long Euler-Bernoulli beam takes into account the force on the beam introduced by the moving oscillator as well as the jump in the vertical stress at the beam-soil interface [12]. It is defined as

$$\begin{aligned} m_b\frac{\partial^2 w_b}{\partial t^2} + EI\frac{\partial^4 w_b}{\partial x^4} = {} & \delta(x - Vt) * \Big\{-\Big[m_1\frac{d^2 w_1}{dt^2} + \big(K + \epsilon_0\frac{d}{dt}\big)\big(w_1 - w_2\big)\Big]\Big\} \\ & - a\big(\sigma_{zz}(x, h-0, t) - \sigma_{zz}(x, h+0, t)\big). \end{aligned} \tag{3.6}$$

EOM FOR THE UPPER MASS m_2 OF THE OSCILLATOR

Finally, an equation is needed that describes the vertical motion of the upper mass m_2 of the moving oscillator. The vibrations of this mass depend on the stiffness and viscosity of the oscillator, of the vertical displacement of the beam at the location of the moving oscillator and on the load $P(t)$. The equation for the vertical motion of the upper oscillator mass reads [12]

$$m_2\frac{d^2 w_2}{dt^2} + \big(K + \epsilon_0\frac{d}{dt}\big)\big(w_2 - w_1\big) = P(t). \tag{3.7}$$

BOUNDARY AND INTERFACE CONDITIONS

After describing the governing equations of motion, the boundary and interface conditions still have to be defined [8]. They are as follows:

- at $z = 0$ the surface is not loaded and traction-free:

$$\sigma_{zz}(x, 0, t) = 0, \tag{3.8a}$$

$$\sigma_{xz}(x, 0, t) = 0, \tag{3.8b}$$

- at $z = h \pm 0$:
  - the beam does not move horizontally and displacements of beam and half-plane are equal at the interfaces:

$$u(x, h-0, t) = 0, \tag{3.9a}$$

$$u(x, h+0, t) = 0, \tag{3.9b}$$

$$w(x, h-0, t) = w_{\mathrm{b}}(x, t), \tag{3.9c}$$

$$w(x, h+0, t) = w_{\mathrm{b}}(x, t), \tag{3.9d}$$

  - the displacement of the lower mass m_1 and of the beam are equal at the location of the oscillator:

$$w_1(t) = w_{\mathrm{b}}(Vt, t). \tag{3.10}$$

  The latter condition is usually referred to as the the continuity condition.

- For $z \to \infty$, the following conditions apply:
  - Sommerfeld's radiation condition: no waves coming from ∞, and
  - response is finite at infinite distance from the source.

3.2.2. EOM, BC AND IC IN THE MOVING REFERENCE SYSTEM

As one of the objectives is to analyze the stability of the oscillator vibrations, it is more convenient to introduce a moving reference system as has been done in references [12, 13, 20]. This moving reference system is determined as

$$\begin{cases} \xi &= x - Vt, \\ z &= z, \\ \tau &= t. \end{cases}$$

By rewriting equations eqs. (3.3) and (3.6) to (3.10) into a reference system that moves along the x-direction with the same speed as the moving oscillator, the stability of vibrations of the oscillator can be analyzed without having to apply the inverse Laplace transform because the argument of the Delta Dirac function in eq. (3.6) is then independent of time [13]. In what follows, this transformation is performed for the aforementioned equations.

- For the EOM describing the half-plane motion (eq. (3.3)), the equations change to

$$\left(\frac{\partial}{\partial \tau} - V\frac{\partial}{\partial \xi}\right)^2 \phi - \left[c_L^2 + \frac{\lambda^* + 2\mu^*}{\rho}\left(\frac{\partial}{\partial \tau} - V\frac{\partial}{\partial \xi}\right)\right]\left(\frac{\partial^2 \phi}{\partial \xi^2} + \frac{\partial^2 \phi}{\partial z^2}\right) = 0, \quad \text{and} \tag{3.11a}$$

$$\left(\frac{\partial}{\partial \tau} - V\frac{\partial}{\partial \xi}\right)^2 \psi - \left[c_T^2 + \frac{\mu^*}{\rho}\left(\frac{\partial}{\partial \tau} - V\frac{\partial}{\partial \xi}\right)\right]\left(\frac{\partial^2 \psi}{\partial \xi^2} + \frac{\partial^2 \psi}{\partial z^2}\right) = 0, \tag{3.11b}$$

- For the EOM describing the beam motion (eq. (3.6)), the following equation in the moving reference system is obtained:

$$\begin{aligned} m_{\mathrm{b}}\Big(\frac{\partial}{\partial\tau}-V\frac{\partial}{\partial\xi}\Big)^2 w_{\mathrm{b}}+EI\frac{\partial^4 w_{\mathrm{b}}}{\partial\xi^4} &= \delta(\xi)*\Big\{-\Big[m_1\frac{d^2 w_1}{d\tau^2}+\Big(K+\epsilon_0\frac{d}{d\tau}\Big)(w_1-w_2)\Big]\Big\} \\ &\quad -a\big(\sigma_{zz}(\xi,h-0,\tau)-\sigma_{zz}(\xi,h+0,\tau)\big), \end{aligned} \tag{3.12}$$

where the expression for $\sigma_{zz}(\xi,z,\tau)$ follows from eq. (3.5a) and reads

$$\begin{aligned} \sigma_{zz}(\xi,z,\tau) &= \Big(\mu+\mu^*\Big(\frac{\partial}{\partial\tau}-V\frac{\partial}{\partial\xi}\Big)\Big)\Big(\frac{c_L^2}{c_T^2}-2\Big)\Big(\frac{\partial^2\phi}{\partial\xi^2}+\frac{\partial^2\phi}{\partial z^2}\Big) \\ &\quad +2\Big(\mu+\mu^*\Big(\frac{\partial}{\partial\tau}-V\frac{\partial}{\partial\xi}\Big)\Big)\Big(\frac{\partial^2\phi}{\partial z^2}+\frac{\partial^2\psi}{\partial\xi\partial z}\Big). \end{aligned} \tag{3.13}$$

- The EOM describing the vertical motion of mass m_2 (eq. (3.7)) is adapted to

$$m_2\frac{d^2 w_2}{d\tau^2}+\Big(K+\epsilon_0\frac{d}{d\tau}\Big)(w_2-w_1)=P(\tau). \tag{3.14}$$

- The boundary conditions at $z=0$ (eq. (3.8)) read

$$\begin{aligned} \sigma_{zz}(\xi,0,\tau) &= \Big(\mu+\mu^*\Big(\frac{\partial}{\partial\tau}-V\frac{\partial}{\partial\xi}\Big)\Big)\Big(\frac{c_L^2}{c_T^2}-2\Big)\Big(\frac{\partial^2\phi}{\partial\xi^2}+\frac{\partial^2\phi}{\partial z^2}\Big) \\ &\quad +2\Big(\mu+\mu^*\Big(\frac{\partial}{\partial\tau}-V\frac{\partial}{\partial\xi}\Big)\Big)\Big(\frac{\partial^2\phi}{\partial z^2}+\frac{\partial^2\psi}{\partial\xi\partial z}\Big)=0, \quad \text{and} \end{aligned} \tag{3.15a}$$

$$\sigma_{xz}(\xi,0,\tau)=\Big(\mu+\mu^*\Big(\frac{\partial}{\partial\tau}-V\frac{\partial}{\partial\xi}\Big)\Big)\Big(2\frac{\partial^2\phi}{\partial\xi\partial z}+\frac{\partial^2\psi}{\partial\xi^2}-\frac{\partial^2\psi}{\partial z^2}\Big)=0. \tag{3.15b}$$

- The interface conditions at $z=h\pm 0$ (eqs. (3.9) and (3.10)),taking into account eq. (3.2), are

$$u(\xi,h-0,\tau)=\frac{\partial\phi}{\partial\xi}-\frac{\partial\psi}{\partial z}=0, \tag{3.16a}$$

$$u(\xi,h+0,\tau)=\frac{\partial\phi}{\partial\xi}-\frac{\partial\psi}{\partial z}=0, \tag{3.16b}$$

$$w(\xi,h-0,\tau)=\frac{\partial\phi}{\partial z}+\frac{\partial\psi}{\partial\xi}=w_{\mathrm{b}}(\xi,\tau), \tag{3.16c}$$

$$w(\xi,h+0,\tau)=\frac{\partial\phi}{\partial z}+\frac{\partial\psi}{\partial\xi}=w_{\mathrm{b}}(\xi,\tau), \tag{3.16d}$$

$$w_1(\tau)=w_{\mathrm{b}}(0,\tau). \tag{3.16e}$$

In eq. (3.16e) $\xi=0$ because the vertical displacement of the beam is equal to that of the lower mass at the location of this mass, so at $x=Vt$ or at $\xi=x-Vt=0$.

3.3. EOM, BC AND IC IN THE LAPLACE-WAVE NUMBER DOMAIN

As discussed in chapter 2, the Fourier and Laplace transforms are tools which can be used to simplify the equations of motion. As this study involves a stability analysis of the oscillator vibrations, the Laplace transform with respect to time should be applied. The Fourier transform is used to transform the horizontal co-ordinate ξ from the space domain into the wavenumber domain. For the problem at hand, the forward Fourier and Laplace transforms are defined as follows [13]:

- for the half-plane motion:

$$f(k,z,s) = \int_0^{+\infty}\int_{-\infty}^{+\infty} \phi(\xi,z,\tau)\exp\left(-s\tau - \mathrm{i}k\xi\right) d\xi\, d\tau, \quad \text{and} \tag{3.17a}$$

$$g(k,z,s) = \int_0^{+\infty}\int_{-\infty}^{+\infty} \psi(\xi,z,\tau)\exp\left(-s\tau - \mathrm{i}k\xi\right) d\xi\, d\tau, \tag{3.17b}$$

- for the beam motion:

$$v_b(k,s) = \int_0^{+\infty}\int_{-\infty}^{+\infty} w_{\mathrm{b}}(\xi,\tau)\exp\left(-s\tau - \mathrm{i}k\xi\right) d\xi\, d\tau, \tag{3.18}$$

- for the motion of the oscillator masses:

$$v_1(s) = \int_0^{+\infty} w_1(\tau)\exp\left(-s\tau\right) d\tau, \quad \text{and} \tag{3.19a}$$

$$v_2(s) = \int_0^{+\infty} w_2(\tau)\exp\left(-s\tau\right) d\tau, \tag{3.19b}$$

- for the load:

$$p(s) = \int_0^{+\infty} P(\tau)\exp\left(-s\tau\right) d\tau, \tag{3.20}$$

- for the half-plane stresses:

$$S_{zz}(k,z,s) = \int_0^{+\infty}\int_{-\infty}^{+\infty} \sigma_{zz}(\xi,z,\tau)\exp\left(-s\tau - \mathrm{i}k\xi\right) d\xi\, d\tau, \quad \text{and} \tag{3.21a}$$

$$S_{xz}(k,z,s) = \int_0^{+\infty}\int_{-\infty}^{+\infty} \sigma_{xz}(\xi,z,\tau)\exp\left(-s\tau - \mathrm{i}k\xi\right) d\xi\, d\tau. \tag{3.21b}$$

Applying the transforms in eqs. (3.17) to (3.21) to the EOMs, BC and IC that were determined in the moving reference system (eqs. (3.11) to (3.16)), results in the governing equations of motion, boundary and interface conditions below.

- For the EOM describing the half-plane motion (eq. (3.11)):

$$\left(s-\mathrm{i}kV\right)^2 f - \left[c_L^2 + \frac{\lambda^* + 2\mu^*}{\rho}\left(s-\mathrm{i}kV\right)\right]\left(\frac{\partial^2 f}{\partial z^2} - k^2 f\right) = 0, \quad \text{and} \tag{3.22a}$$

$$\left(s-\mathrm{i}kV\right)^2 g - \left[c_T^2 + \frac{\mu^*}{\rho}\left(s-\mathrm{i}kV\right)\right]\left(\frac{\partial^2 g}{\partial z^2} - k^2 g\right) = 0, \tag{3.22b}$$

- for the EOM describing the beam motion (eq. (3.12)):

$$\begin{aligned} D(k,s)\,v_b(k,s) = &-\left[m_1 s^2 v_1 + \left(K+\epsilon_0 s\right)\left(v_1 - v_2\right)\right] \\ &- a\left(S_{zz}(k,h-0,s) - S_{zz}(k,h+0,s)\right), \end{aligned} \tag{3.23}$$

where

- the expression for $S_{zz}(k,z,s)$ follows from eqs. (3.13) and (3.21a):

$$\begin{aligned} S_{zz}(k,z,s) = \big(\mu+\mu^*(s-\mathrm{i}kV)\big)\big(\frac{c_L^2}{c_T^2}-2\big)\big(\frac{\partial^2 f}{\partial z^2}-k^2 f\big) \\ +2\big(\mu+\mu^*(s-\mathrm{i}kV)\big)\big(\frac{\partial^2 f}{\partial z^2}+\mathrm{i}k\frac{\partial g}{\partial z}\big), \quad \text{and} \end{aligned} \tag{3.24}$$

- the expression for D is given by:

$$D(k,s) = m_\mathrm{b}\big(s-\mathrm{i}kV\big)^2 + EIk^4,$$

- for the EOM describing the motion of the upper oscillator mass (eq. (3.14)):

$$m_2 s^2 v_2 + \big(K+\epsilon_0 s\big)\big(v_2-v_1\big) = p(s), \tag{3.25}$$

- for the boundary conditions at $z=0$ (eq. (3.15)):

$$\begin{aligned} S_{zz}(k,0,s) = \big(\mu+\mu^*(s-\mathrm{i}kV)\big)\big(\frac{c_L^2}{c_T^2}-2\big)\big(\frac{\partial^2 f}{\partial z^2}-k^2 f\big) \\ +2\big(\mu+\mu^*(s-\mathrm{i}kV)\big)\big(\frac{\partial^2 f}{\partial z^2}+\mathrm{i}k\frac{\partial g}{\partial z}\big) = 0, \quad \text{and} \end{aligned} \tag{3.26a}$$

$$S_{xz}(k,0,s) = \big(\mu+\mu^*(s-\mathrm{i}kV)\big)\big(2\mathrm{i}k\frac{\partial f}{\partial z}-k^2 g-\frac{\partial^2 g}{\partial z^2}\big) = 0, \tag{3.26b}$$

- for the interface conditions at $z = h \pm 0$ (eq. (3.16)):

$$\mathrm{i}kf - \frac{\partial g}{\partial z}\Big|_{z=h-0} = 0, \tag{3.27a}$$

$$\mathrm{i}kf - \frac{\partial g}{\partial z}\Big|_{z=h+0} = 0, \tag{3.27b}$$

$$\frac{\partial f}{\partial z} + \mathrm{i}kg\Big|_{z=h-0} = v_b(k,s), \tag{3.27c}$$

$$\frac{\partial f}{\partial z} + \mathrm{i}kg\Big|_{z=h+0} = v_b(k,s), \quad \text{and} \tag{3.27d}$$

$$v_1(s) = v_b(\xi,s)\Big|_{\xi=0}, \tag{3.27e}$$

where $v_b(\xi,s)$ is the forward Laplace transform of $w_\mathrm{b}(\xi,\tau)$ or, similarly, the inverse Fourier transform of $v_b(k,s)$ and is described as

$$\begin{aligned} v_b(\xi,s) &= \int_0^{+\infty} w_\mathrm{b}(\xi,\tau)\exp(-s\tau)\,d\tau \\ &= \frac{1}{2\pi}\int_{-\infty}^{+\infty} v_b(k,s)\exp(\mathrm{i}k\xi)\,dk. \end{aligned} \tag{3.28}$$

For the further analysis, the following variable is introduced to simplify the notation of the equations:

$$\mu_{sk} = \mu + \mu^*\big(s-\mathrm{i}kV\big). \tag{3.29}$$

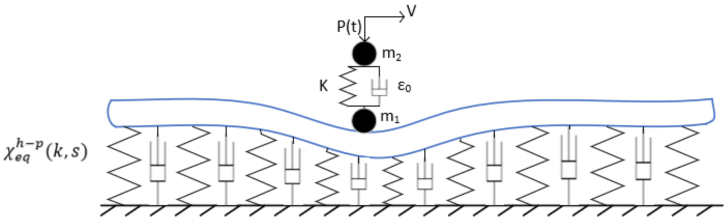

Figure 3.2: Equivalent one-dimensional model for the beam on the half-plane loaded by a uniformly moving two-mass oscillator for which the reaction of the half-plane is represented by the complex stiffness $\chi_{\text{eq}}^{\text{h-p}}(k,s)$. [12]

3.4. REDUCTION OF THE MODEL AND EXPRESSION FOR OSCILLATOR VIBRATION

THE approach proposed in references [12, 13, 20] is used to find the expression for the vibrations of the oscillator moving along a beam embedded in a visco-elastic half-plane. As discussed in section 2.2.3, in a first step the model is reduced to the equivalent one-dimensional model shown in fig. 3.2 by deriving the equivalent stiffness of the half-plane $\chi_{\text{eq}}^{\text{h-p}}(k,s)$. The next step is then to further reduce the model to the lumped mass-spring-dashpot model given in fig. 2.21 in which the reaction of the embedded beam in the point of contact with the moving oscillator is given by the equivalent spring stiffness $\chi_{\text{eq}}^{\text{beam}}(s,V)$. This stiffness depends both on the frequency of the oscillator's vertical vibrations and on its velocity along the beam.

3.4.1. EQUIVALENT STIFFNESS HALF-PLANE

Figure 3.2 considers the oscillator motion along the beam on a visco-elastic foundation with stiffness $\chi_{\text{eq}}^{\text{h-p}}(k,s)$. This foundation accounts for the reaction of the half-plane. As discussed in section 2.2.3, the equivalent half-plane stiffness that is a function of the two variables s and k, can be found by searching for a description of the beam motion in the same form as that for the motion of the infinitely long Euler-Bernoulli beam loaded by a moving two-mass oscillator and supported by a Winkler foundation with stiffness χ, as given by eq. (3.30) [12, 13, 21]. The derivation of this expression is depicted in appendix A.

$$v_b(k,s)\big(D(k,s)+\chi\big) = v_2(s)\big(K+\epsilon_0 s\big) - v_1(s)\big(m_1 s^2 + K + \epsilon_0 s\big). \tag{3.30}$$

In the one-dimensional model, the equivalent stiffness of the half-plane substitutes the stiffness χ in eq. (3.30) and is determined from the general solution to eq. (3.22):

- for $z \in [0, h-0]$:

$$f = A_1 \exp\left(-zR_L\right) + A_2 \exp\left((z-h)R_L\right), \quad \text{and} \tag{3.31a}$$

$$g = A_3 \exp\left(-zR_T\right) + A_4 \exp\left((z-h)R_T\right), \tag{3.31b}$$

- for $z \in [h+0, +\infty]$ and taking into account the boundary conditions for $z \to \infty$ as defined earlier in section 3.2 :

$$f = A_5 \exp\left(-(z-h)R_L\right), \quad \text{and} \tag{3.32a}$$

$$g = A_6 \exp\left(-(z-h)R_T\right), \tag{3.32b}$$

where

$$R_L = \sqrt{k^2 + \frac{\left(s - \mathrm{i}kV\right)^2}{c_L^2 + \frac{\lambda^* + 2\mu^*}{\rho}\left(s - \mathrm{i}kV\right)}}, \qquad R_T = \sqrt{k^2 + \frac{\left(s - \mathrm{i}kV\right)^2}{c_T^2 + \frac{\mu^*}{\rho}\left(s - \mathrm{i}kV\right)}}. \tag{3.33}$$

The exponents in the general solution are chosen in the particular way shown in eqs. (3.31) and (3.32) to avoid the values of the constants (and thus of the solution) to explode for the case where a large value of h is combined with large values of k and thus of $R_{L,T}$.
Equation (3.32) already takes into account the fact that there is no energy coming from infinity and that the response has to be finite at infinite distance from the source. Assuming that both $\Re(R_{L,T}) \geq 0$ and $\Re(s) \geq 0$, this means that the terms containing $\exp(+zR_{L,T})$ drop out of the solution for the half-plane motion below the beam-soil interface.

Substitution of the general solution eqs. (3.31) and (3.32) into the boundary and interface conditions (eqs. (3.26) and (3.27a) to (3.27d)) gives the following system of algebraic equations with unknowns $A_1 \to A_6$:

- for boundary conditions at $z = 0$ (eq. (3.26)):

$$\begin{aligned} \frac{-2\mu_{sk}}{c_T^2}\Big[\Big(\frac{\alpha k^2 - \beta}{2}\Big)A_1 + \Big(\frac{\alpha k^2 - \beta}{2}\Big)\exp(-hR_L)A_2 & \\ + \mathrm{i}R_T c_T^2 k A_3 - \mathrm{i}R_T c_T^2 k \exp(-hR_T)A_4\Big] &= 0, \quad \text{and} \qquad (3.34\text{a}) \\ 2\mu_{sk}\Big[-\mathrm{i}R_L k A_1 + \mathrm{i}R_L k\exp(-hR_L)A_2 & \\ -\frac{\left(R_T^2 + k^2\right)}{2}A_3 - \frac{\left(R_T^2 + k^2\right)\exp(-hR_T)}{2}A_4\Big] &= 0, \qquad (3.34\text{b}) \end{aligned}$$

- for boundary conditions at $z = h - 0$ (eqs. (3.27a) and (3.27c)):

$$\begin{aligned} \mathrm{i}k\big(A_1\exp(-hR_L) + A_2\big) + R_T\big(A_3\exp(-hR_T) - A_4\big) &= 0, \quad \text{and} \qquad (3.35\text{a}) \\ -R_L\big(A_1\exp(-hR_L) - A_2\big) + \mathrm{i}k\big(A_3\exp(-hR_T) + A_4\big) &= v_b(k,s), \qquad (3.35\text{b}) \end{aligned}$$

- for boundary conditions at $z = h + 0$ (eqs. (3.27b) and (3.27d)):

$$\begin{aligned} \mathrm{i}kA_5 + R_T A_6 &= 0, \quad \text{and} \qquad (3.36\text{a}) \\ -R_L A_5 + \mathrm{i}kA_6 &= v_b(k,s). \qquad (3.36\text{b}) \end{aligned}$$

The expression for $v_b(k,s)$ is derived from eq. (3.23) and reads

$$v_b(k,s) = \frac{1}{D(k,s)}\Big\{-\Big[m_1 s^2 v_1 + \big(K + \epsilon_0 s\big)\big(v_1 - v_2\big)\Big]\Big\} - a\big(S_{zz}(k,h-0,s) - S_{zz}(k,h+0,s)\big) \tag{3.37}$$

The obtained system of six equations and six unknowns may be written in the form

$$\sum_{j=1}^{6} a_{ij}A_j = F_i, \tag{3.38}$$

where i goes from one to six. The matrices with the values for coefficients a_{ij} and for F_i are given in appendix B. According to Cramer's rule the solution of this linear system with an equal number of equations and unknowns can be found in the following way:

$$A_j = \frac{\Delta_j(k,s)}{\Delta(k,s)}, \tag{3.39}$$

where $\Delta(k,s)$ is the determinant of the coefficient matrix a_{ij} as given in appendix B and $\Delta_j(k,s)$ is the determinant of the modified matrix $\tilde{a}_{ij}$ where column j of the matrix a_{ij} has been replaced by the column vector F_i.

The values for the unknown constants $A_1 \rightarrow A_6$ are obtained using Maple 2017 Release 3 (Waterloo Maple Inc.). Maple uses Cramer's rule to obtain the solution of linear systems. In their most simplified form, the unknowns can be written as:

- for $z \in [0, h-0]$:

$$A_i = \frac{N_i}{D^-}, \tag{3.40}$$

for i=1,..,4,

- for $z \in [0, h+0]$:

$$A_j = \frac{N_j}{D^+}, \tag{3.41}$$

for j=5,6.

The values for N_i, N_j, D^- and D^+ can be found in appendix B. Figure B.1 of this appendix presents the Maple code applied to find the expressions for the constants.

Once the values of the constants have been determined, the general solution to the equation of motion for the half-plane is known in the Laplace-wavenumber domain. As shown before, the vertical stresses in the soil can be described in terms of f and g and thus, $S_{zz}(k,h-0,s)$ and $S_{zz}(k,h+0,s)$ in eq. (3.23) are found. The motion of the beam embedded in the half-plane and loaded by a two-mass moving oscillator can then be derived in the form of eq. (3.30):

$$v_b(k,s)\left(D(k,s)+\chi_{\text{eq}}^{\text{h-p}}(k,s)\right) = v_2(s)\left(K+\epsilon_0 s\right) - v_1(s)\left(m_1 s^2 + K + \epsilon_0 s\right), \tag{3.42}$$

where $\chi_{\text{eq}}^{\text{h-p}}(k,s)$ is the equivalent stiffness of the half-plane interacting with the beam and is found as

$$\begin{aligned}\chi_{\text{eq}}^{\text{h-p}}(k,s) &= \frac{a\left(S_{zz}(k,h-0,s)-S_{zz}(k,h+0,s)\right)}{v_b(k,s)}\\ &= -\frac{2\mu_{sk}a}{c_T^2 v_b}\left[\frac{A_1\left(\alpha k^2-\beta\right)}{2}\exp\left(-hR_L\right)+\frac{\left(A_2-A_5\right)\left(\alpha k^2-\beta\right)}{2}\right.\\ &\quad\left.+\,\mathrm{i}kR_T c_T^2 A_3 \exp\left(-hR_T\right) - \mathrm{i}kR_T c_T^2\left(A_4+A_6\right)\right].\end{aligned} \tag{3.43}$$

The following notations have been introduced in order to simplify the expression for $\chi_{\text{eq}}^{\text{h-p}}$:

$$\alpha = c_L^2 - 2c_T^2, \qquad \beta = R_L^2 c_L^2.$$

Equation (3.42) together with the equation of motion for the upper mass of the oscillator (eq. (3.25)) and the condition of continuity between the lower oscillator mass and the beam (eq. (3.27e)) describe vibrations of the oscillator on the beam supported by a visco-elastic foundation as depicted in fig. 3.2 [12].

3.4.2. EQUIVALENT STIFFNESS BEAM AND EXPRESSION FOR OSCILLATOR VIBRATION

In what follows, the one-dimensional model of the previous section is further reduced to the model shown in fig. 2.21 following the procedure described in section 2.2.3. First the inverse Fourier transform on $v_b(k,s)$ (eq. (3.42)) is applied. Subsequently, the continuity condition expressed by eq. (3.27e) is inserted.

The inverse Fourier transform of $v_b(k,s)$ is given by

$$\begin{aligned} v_b(\xi,s) &= \frac{1}{2\pi}\int_{-\infty}^{+\infty} v_b(k,s)\exp(\mathrm{i}k\xi)\,dk \\ &= \frac{1}{2\pi}\int_{-\infty}^{+\infty}\left[\frac{-v_1\left(m_1s^2+K+\epsilon_0 s\right)+v_2\left(K+\epsilon_0 s\right)}{D(k,s)+\chi_{\mathrm{eq}}^{\text{h-p}}(k,s)}\right]\exp(\mathrm{i}k\xi)\,dk \\ &= \left[\frac{-v_1\left(m_1s^2+K+\epsilon_0 s\right)+v_2\left(K+\epsilon_0 s\right)}{2\pi}\right]\int_{-\infty}^{+\infty}\frac{\exp(\mathrm{i}k\xi)\,dk}{D(k,s)+\chi_{\mathrm{eq}}^{\text{h-p}}(k,s)}, \end{aligned} \tag{3.44}$$

and the continuity condition

$$v_1(s) = v_b(\xi,s)\Big|_{\xi=0}, \tag{3.45}$$

is inserted.

The resulting equation (eq. (3.46)) describes the behaviour of the lumped mass-spring-dashpot model. From this equation, one can obtain the equivalent stiffness of the beam embedded in the half-plane at the location of the contact point with the moving oscillator as follows [12]:

$$v_1\left(m_1s^2+K+\epsilon_0 s+\chi_{\mathrm{eq}}^{\mathrm{beam}}(s)\right)-v_2\left(K+\epsilon_0 s\right)=0, \tag{3.46}$$

where

$$\chi_{\mathrm{eq}}^{\mathrm{beam}}(s) = \left[\frac{1}{2\pi}\int_{-\infty}^{+\infty}\frac{dk}{D(k,s)+\chi_{\mathrm{eq}}^{\text{h-p}}(k,s)}\right]^{-1} \tag{3.47}$$

As stated in [12, 13, 20], it are the roots of the characteristic equation that determine the stability of the system. This equation is obtained by combining the equation of motion for the upper mass of the oscillator (eq. (3.25)) and eq. (3.46):

$$v_1\left[\left(m_1s^2+K+\epsilon_0 s+\chi_{\mathrm{eq}}^{\mathrm{beam}}\right)\left(m_2s^2+K+\epsilon_0 s\right)-\left(K+\epsilon_0 s\right)^2\right]=p\left(K+\epsilon_0 s\right), \tag{3.48}$$

in which

$$\left(m_1s^2+K+\epsilon_0 s+\chi_{\mathrm{eq}}^{\mathrm{beam}}\right)\left(m_2s^2+K+\epsilon_0 s\right)-\left(K+\epsilon_0 s\right)^2=0 \tag{3.49}$$

represents the characteristic equation for the vertical vibrations of the oscillator.

4

RESULTS AND ANALYSIS: INSTABILITY OF THE OSCILLATOR VIBRATION

As shown in references [12, 13, 20], the roots of the characteristic equation (eq. (3.49)) determine the stability of the uniformly moving oscillator. Section 2.1.1 explains that when at least one of the eigenvalues s of the system has a positive real part, instability occurs. As the roots of eq. (3.49) depend crucially on the dynamic stiffness χ_{eq}^{beam} *of the beam in the point of contact with the moving oscillator, this equivalent stiffness is analyzed first. Subsequently the roots of the characteristic equation are investigated employing the D-decomposition method described in section 2.2.4. Based on the D-decomposition, instability regions are defined for different values of the model parameters. The derivation of these instability domains facilitates the determination of the velocity from which the oscillator vibrations become unstable given certain values of the parameters. However, because of its relevance throughout this study, first the dispersion relation for the elastic system is discussed.*

4.1. DISPERSION RELATION FOR THE BEAM-HALF-PLANE SYSTEM

BASED on the explanation in section 2.2.1 the dispersion curve for waves propagating with a constant amplitude in the system under consideration is obtained as the real solution to the following equation:

$$\lim_{\mu^*,\lambda^*=0} \Delta(k,\omega) = 0, \tag{4.1}$$

where the material damping in the half-plane as well as the moving oscillator are neglected. More specifically, the dispersion curve can be found by taking the determinant of the coefficient matrix in appendix B equal to zero while changing the following terms in this matrix:

- s is replaced by $\mathrm{i}\omega$,
- μ_{sk} is replaced by μ,
- $D(k,s)$ is replaced by $D(k,\omega) = -m_b\omega^2 + EIk^4$, and
- R_L and R_T are replaced by $q_L = \sqrt{k^2 - \omega^2/c_L^2}$ and $q_T = \sqrt{k^2 - \omega^2/c_T^2}$ respectively.

Figure 4.1a depicts the real solution to eq. (4.1). This is the dispersion curve for non-attenuating waves. The dispersion curves for waves which propagate with a slight attenuation are defined as the

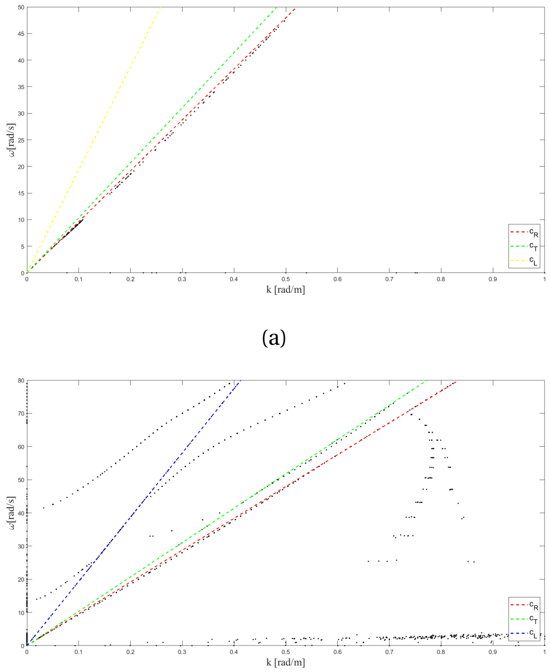

(a)

(b)

Figure 4.1: (a) Zeros of $\Delta(k,\omega)$, defining the dispersion curve for waves propagating with constant amplitude. Imaginary and real part of the determinant are equal to zero in this case. (b) Local minima of $|\Delta(k,\omega)|$, including the dispersion curves for slightly attenuated waves. For obtaining both figures, the material damping is set to zero: $\mu^* = \lambda^* = 0$.

minima of the function $|\Delta(k,\omega)|$. For these waves the wavenumber is complex-valued. The dispersion curves for both attenuated and non-attenuating waves are determined using Matlab R2018a. The Matlab code is included in appendix C. The dots in fig. 4.1b represent the local minima of the determinant. Because the system consists of two completely alien structures, i.e. the beam and the half-plane, not all local minima that are found are really part of a dispersion curve. However, fig. 4.1 clearly shows the dispersion curve for waves that propagate with constant amplitude. For low values of k this curve lies slightly below the red line indicating the Rayleigh wave speed, while it converges towards the c_R-line for higher wavenumber values. The minimum phase velocity is determined by the slope of the tangent to this dispersion curve and is equal to 92.98 m/s ($= 0.898 * c_T$), which is a bit lower than the Rayleigh wave speed $c_R = 95.9$ m/s ($= 0.927 * c_T$).

The system parameters for which the dispersion curves are plotted and the minimum phase velocity $v_{\text{ph}}^{\text{min}}$ is calculated, are given in table 4.1. These parameters are valid for a soft soil.

4.2. EQUIVALENT DYNAMIC STIFFNESS OF THE BEAM

THE dynamic stiffness $\chi_{\text{eq}}^{\text{beam}}$ is a function of s. As shown in section 2.1.1, it is the sign of the term related to s in the characteristic equation which determines the system stability. This means that the sign of the imaginary part of $\chi_{\text{eq}}^{\text{beam}}$ decides whether the eigenvalues may have a positive real part. More precisely, when, for a certain load velocity, $\Im(\chi_{\text{eq}}^{\text{beam}})$ is positive over the whole frequency band, the oscillator is unconditionally stable. If, on the other hand, $\Im(\chi_{\text{eq}}^{\text{beam}})$ is negative at a certain fre-

System part	Parameter	Value	Unit
Half-plane	ν	0.3	-
	ρ	1960	kg/m^3
	μ	$2.1 \cdot 10^7$	N/m^2
	c_L	193.6	m/s
	c_T	103.5	m/s
	c_R	95.9	m/s
Beam and Interface	EI	$1.3 \cdot 10^8$	N/m^2
	m_b	7500	kg/m
	h	12	m
	a	1.5	m

Table 4.1: Basic system parameters [12].

quency band and for certain velocities of the load, the equivalent viscosity of the beam in the point of contact with the oscillator is negative and instability of vibrations *can* occur [13]. For this reason, the stability analysis starts with the study of $\chi_{\mathrm{eq}}^{\mathrm{beam}}$ as described by eq. (3.47).

For the stability analysis s is set equal to iΩ. Thus, from now on the equivalent dynamic stiffness of the beam is considered as a function of the velocity V of the moving oscillator and the radial frequency Ω of its vertical vibrations:

$$\chi_{\mathrm{eq}}^{\mathrm{beam}}(\Omega) = \left[\frac{1}{2\pi}\int_{-\infty}^{+\infty} \frac{dk}{D(k,\Omega)+\chi_{\mathrm{eq}}^{\mathrm{h\text{-}p}}(k,\Omega)}\right]^{-1}. \tag{4.2}$$

When the material damping in the half-plane is included, the zeros of $\{D(k,\Omega)+\chi_{\mathrm{eq}}^{\mathrm{h\text{-}p}}(k,\Omega)\}$ are in the complex plane. As $\chi_{\mathrm{eq}}^{\mathrm{beam}}$ is obtained by integrating along the real k-axis, the fact that the denominator has no real zeros is a necessary requirement to be able to numerically integrate eq. (4.2). The second requirement to find $\chi_{\mathrm{eq}}^{\mathrm{beam}}$ numerically is that the integral converges for certain limit values of k. As the integrand tends to zero for large values of k, proportionally with $k^{(-4)}$, numerical integration is possible [12].

4.2.1. THE INTEGRATION ROUTINE

The integral in eq. (4.2) goes from $-\infty$ to $+\infty$. However, the value of the integrand shows peaks for specific values of the wavenumber k, while at the same time, the integrand is negligibly small for high wavenumbers. Section 2.2.1 explains that the frequency ω and wavenumber k of the waves that are perturbed by the moving load are determined by the crossing points between the dispersion curves and the kinematic invariant. Metrikine and Vrouwenvelder [8] show that the maxima in the response spectrum of structural displacements occur at the location of these points of intersection. Therefore, the peaks in the integrand of $\chi_{\mathrm{eq}}^{\mathrm{beam}}(\Omega)$ are found where the kinematic invariant crosses the dispersion curves. The Matlab code that defines the local maxima of the absolute value of the integrand is included in appendix C. This code finds the local maxima of the integrand by performing a grid optimization with three variables, k, Ω and V. The most important peaks in the absolute value of the integrand are located in the interval $k \in [0\ 1]$. The range of k over which the integration will be performed is taken as [0 10000] as this interval contains a sufficiently large safety margin for k.

As mentioned before, the integral in the formula for $\chi_{\mathrm{eq}}^{\mathrm{beam}}(\Omega)$ (eq. (4.2)) starts at $-\infty$. However, when determining the values of k where the integrand of eq. (4.2) has peaks, only positive wavenumbers are considered. To change the lower bound of the integration domain to zero, the following relation is used:

$$\begin{aligned} &\int_{-\infty}^{+\infty} f(k)\,dk = \int_{-\infty}^{0} f(k)\,dk + \int_{0}^{+\infty} f(k)\,dk, \\ \text{where } &\int_{-\infty}^{0} f(k)\,dk = \int_{+\infty}^{0} f(-k)\,d(-k) = \int_{0}^{+\infty} f(-k)\,dk. \\ \text{So } &\int_{-\infty}^{+\infty} f(k)\,dk = \int_{0}^{+\infty} \big(f(-k) + f(k)\big)\,dk, \end{aligned} \tag{4.3}$$

where $f(k)$ represents the integrand of eq. (4.2).

The Matlab code employed for performing the numerical integration and hence determining the value of $\chi_{\text{eq}}^{\text{beam}}$ for the considered frequency range and V going from $0.2c_T$ to $2.9c_T$ is presented in appendix D. In first instance, the integration routine determines the integration grid based on the integrand peaks. The grid is further refined to ensure correct results. Finally, Riemann summation is employed to find the value of $\chi_{\text{eq}}^{\text{beam}}$ as a function of V and Ω.

4.2.2. ANALYSIS EQUIVALENT DYNAMIC STIFFNESS BEAM

EQUIVALENT DYNAMIC STIFFNESS AS A FUNCTION OF OSCILLATOR VELOCITY

Taking into account the earlier defined system parameters, fig. 4.2 presents the results of the numerical integration for a low frequency band ($\Omega < 40$) and different velocities of the load. To obtain these figures, the material damping is set to $\mu^* = \lambda^* = 0.001\mu$ s. $\Re(\chi_{\text{eq}}^{\text{beam}})$ and $\Im(\chi_{\text{eq}}^{\text{beam}})$ are plotted against the frequency Ω for different velocities V of the moving oscillator. To visualize the results clearly for all frequencies, the values of $\Im(\chi_{\text{eq}}^{\text{beam}})$ are depicted for a small frequency band (plots on the left-hand side of the second row) as well as for the frequency band from $\Omega = 1$ up to $\Omega = 40$ (plots on the right-hand side of the first row). In the plots on the right-hand side of the second row in fig. 4.2, the real and imaginary part of $\chi_{\text{eq}}^{\text{beam}}$ are compared.

For certain frequencies of the moving oscillator, peaks in the real part of the equivalent dynamic beam stiffness arise. As can be seen in fig. 4.2, a peak in $\Re(\chi_{\text{eq}}^{\text{beam}})$ corresponds with the steepest slope in the curve representing $\Im(\chi_{\text{eq}}^{\text{beam}})$. These peaks are resonance peaks where the velocity of the moving oscillator corresponds to the group velocity of waves propagating in the system. They are finite due to the presence of material damping in the half-plane. In fig. 4.3 the case of resonance is presented by the blue line. This kinematic invariant line is tangent to the dispersion curve and thus gives a combination of frequency and velocity of the moving oscillator for which resonance occurs.

As long as the oscillator moves with a velocity lower than the Rayleigh wave speed, the imaginary part of $\chi_{\text{eq}}^{\text{beam}}$ is positive over the whole frequency band as shown in figs. 4.2a and 4.2b. The vertical vibrations of the oscillator are unconditionally stable for these velocities.
Figure 4.2c presents the case where the oscillator velocity exceeds the Rayleigh wave speed but is still lower than the shear wave speed c_T in the half-plane. Now the imaginary part of the equivalent dynamic stiffness of the beam is negative for low frequencies of the oscillator's vibrations (up to $\Omega \approx 1.6$ rad/s). $\Im(\chi_{\text{eq}}^{\text{beam}}) < 0$ corresponds to a 'negative viscosity' of the equivalent spring and, as discussed in section 2.2.4, this implies that the oscillator vibrations may become unstable due to the radiation of anomalous Doppler waves by the moving load.

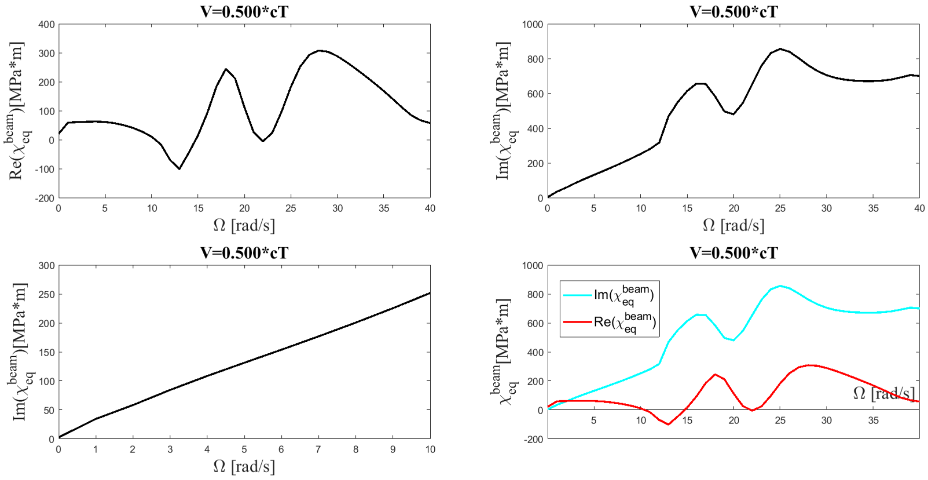
V=0.500*cT
Re(χ_eq^beam)[MPa*m]
Im(χ_eq^beam)[MPa*m]
χ_eq^beam[MPa*m]
Ω [rad/s]
Im(χ_eq^beam)
Re(χ_eq^beam)
400
300
200
100
0
-100
-200
1000
800
600
400
250
150
50
0
5
10
15
20
25
30
35
40
1
2
3
4
6
7
8
9

(a)

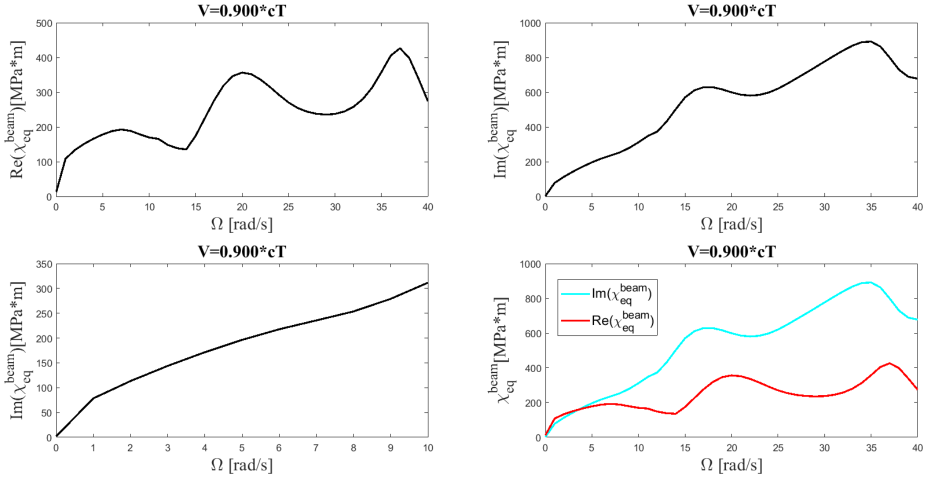
V=0.900*cT
Re(χ_eq^beam)[MPa*m]
Im(χ_eq^beam)[MPa*m]
χ_eq^beam[MPa*m]
Ω [rad/s]
Im(χ_eq^beam)
Re(χ_eq^beam)
500
400
300
200
100
0
1000
800
600
350
250
150
50
5
10
15
20
25
30
35
40
1
2
3
4
6
7
8
9

(b)

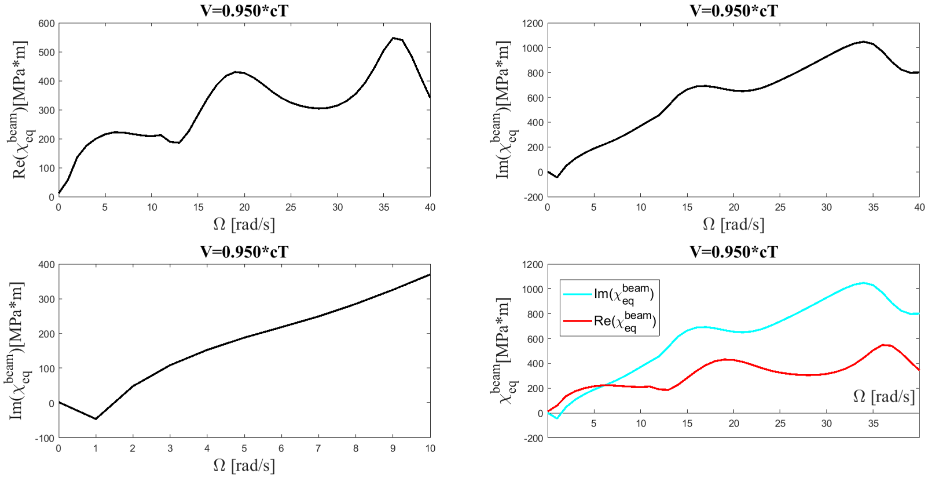
V=0.950*cT
Re(χ_eq^beam)[MPa*m]
Im(χ_eq^beam)[MPa*m]
χ_eq^beam[MPa*m]
Ω [rad/s]
Im(χ_eq^beam)
Re(χ_eq^beam)
600
500
400
300
200
100
0
-100
-200
1200
1000
800
5
10
15
20
25
30
35
40
1
2
3
4
6
7
8
9

(c)

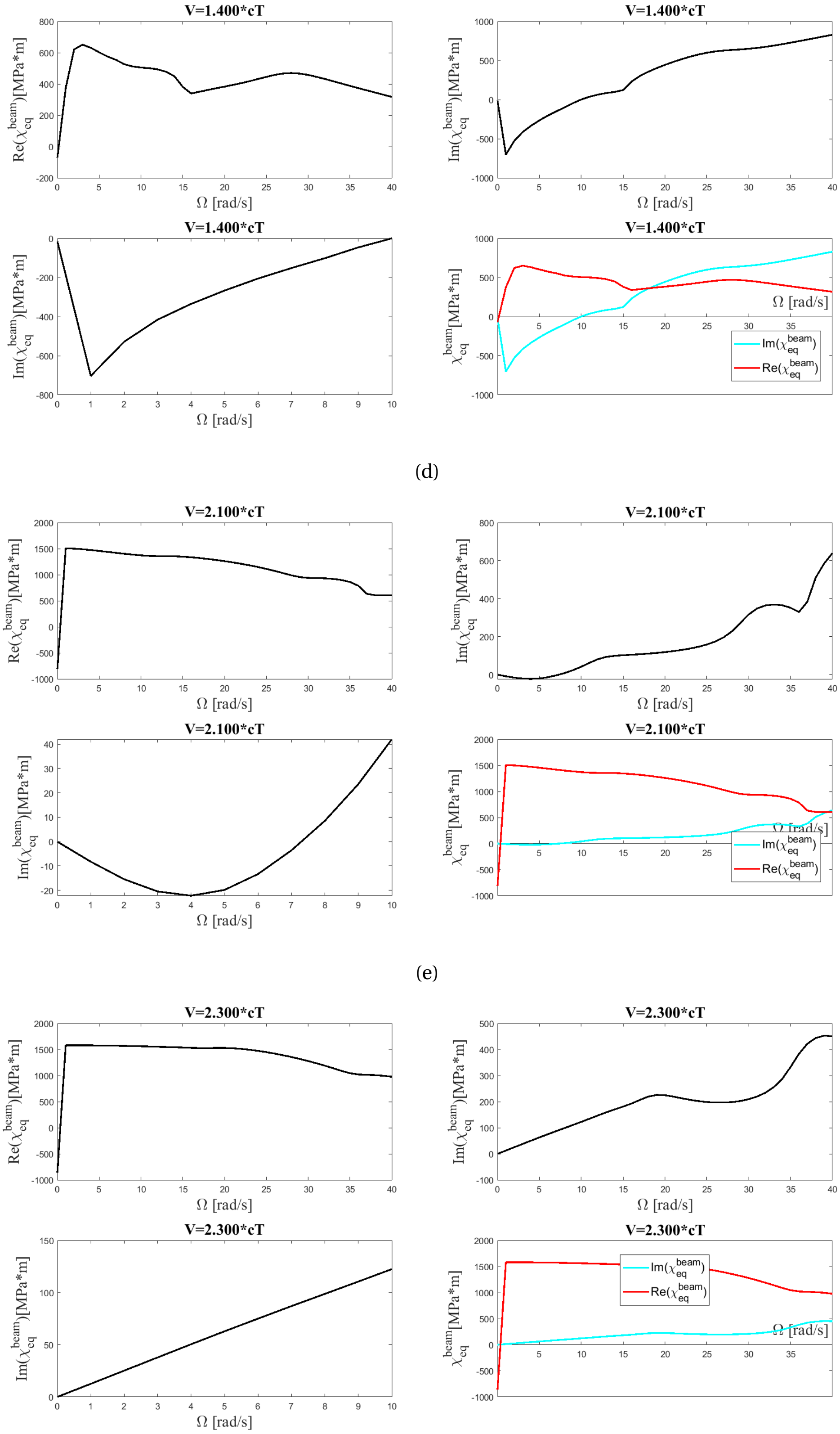

(d)

(e)

(f)

Figure 4.2: Equivalent dynamic stiffness of the beam embedded in the half-plane versus frequency Ω of the oscillator for (a) $V = 0.5c_T$, (b) $V = 0.9c_T$, (c) $V = 0.95c_T$, (d) $V = 1.4c_T$, (e) $V = 2.1c_T$ and (f) $V = 2.3c_T$.

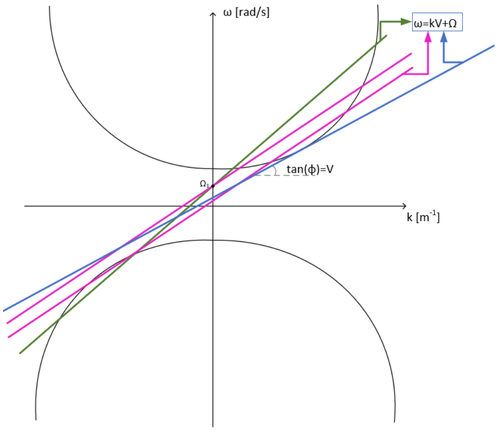

Figure 4.3: Relation dispersion curve and kinematic invariant for different values of the frequency Ω and velocity V of the moving load.

In fig. 4.2d the vehicle speed exceeds the shear wave speed. Rayleigh waves as well as shear waves are radiated. As compared to the case where $V = 0.95c_T$, the frequency band where the imaginary part of $\chi_{\text{eq}}^{\text{beam}}$ is negative, widens for $V = 1.4c_T$. This observation agrees with what would be expected from studying the green and purple lines in fig. 4.3. The slope of the kinematic invariant represented by the purple line is smaller than that of the green curve, which implies a lower oscillator velocity. For the same angular frequency Ω_1 of the oscillator, the purple line does not cross the dispersion curve on the negative side of the frequency axis, while the green curve does. Only for lower frequencies the purple curve crosses the dispersion curve on this side, in which case anomalous Doppler waves are radiated. Figure 4.2e corresponds to an oscillator velocity higher than $c_L = 1.87c_T$, which means that Rayleigh, shear and compressional waves are radiated. $\Im(\chi_{\text{eq}}^{\text{beam}})$ is still negative for low frequencies but the frequency band corresponding to a 'negative viscosity' of the equivalent spring has shrunk. Moreover, the absolute value of $\Im(\chi_{\text{eq}}^{\text{beam}})$ has decreased at this frequency range.

Figure 4.2f shows that when the velocity of the moving oscillator is further increased, $\Im(\chi_{\text{eq}}^{\text{beam}})$ is again positive over the whole frequency band. As discussed by Metrikine and Veritchev [12], this is due to the effect of the material damping in the half-plane. Without this material damping the 'negative viscosity' would not have disappeared at the observed oscillator velocity. The value of V for which $\Im(\chi_{\text{eq}}^{\text{beam}})$ becomes positive again over the whole frequency range, depends on the values of the half-plane parameters. Furthermore, for certain material properties, the damping can become 'negative' again when the oscillator velocity further increases [12]. Metrikine and Veritchev [12] point out that there always exists a material damping magnitude for which the imaginary part of the equivalent dynamic stiffness is positive over the full frequency band for all oscillator velocities. For the considered model, this is the case from the moment the magnitude of the material damping reaches the very high material damping value $\mu^* = \lambda^* = 0.8\mu$ s.

EQUIVALENT DYNAMIC STIFFNESS AS A FUNCTION OF MATERIAL DAMPING

Figure 4.4 demonstrates the effect of the material damping by plotting the real and imaginary part of $\chi_{\text{eq}}^{\text{beam}}$ against the angular frequency of the oscillator for different values of the material damping and different oscillator velocities.

For higher values of the half-plane viscosity, the resonance peaks are less pronounced and eventually disappear, confirming the fact that the resonance vibration can be effectively damped as has been shown by Metrikine and Dieterman [20].

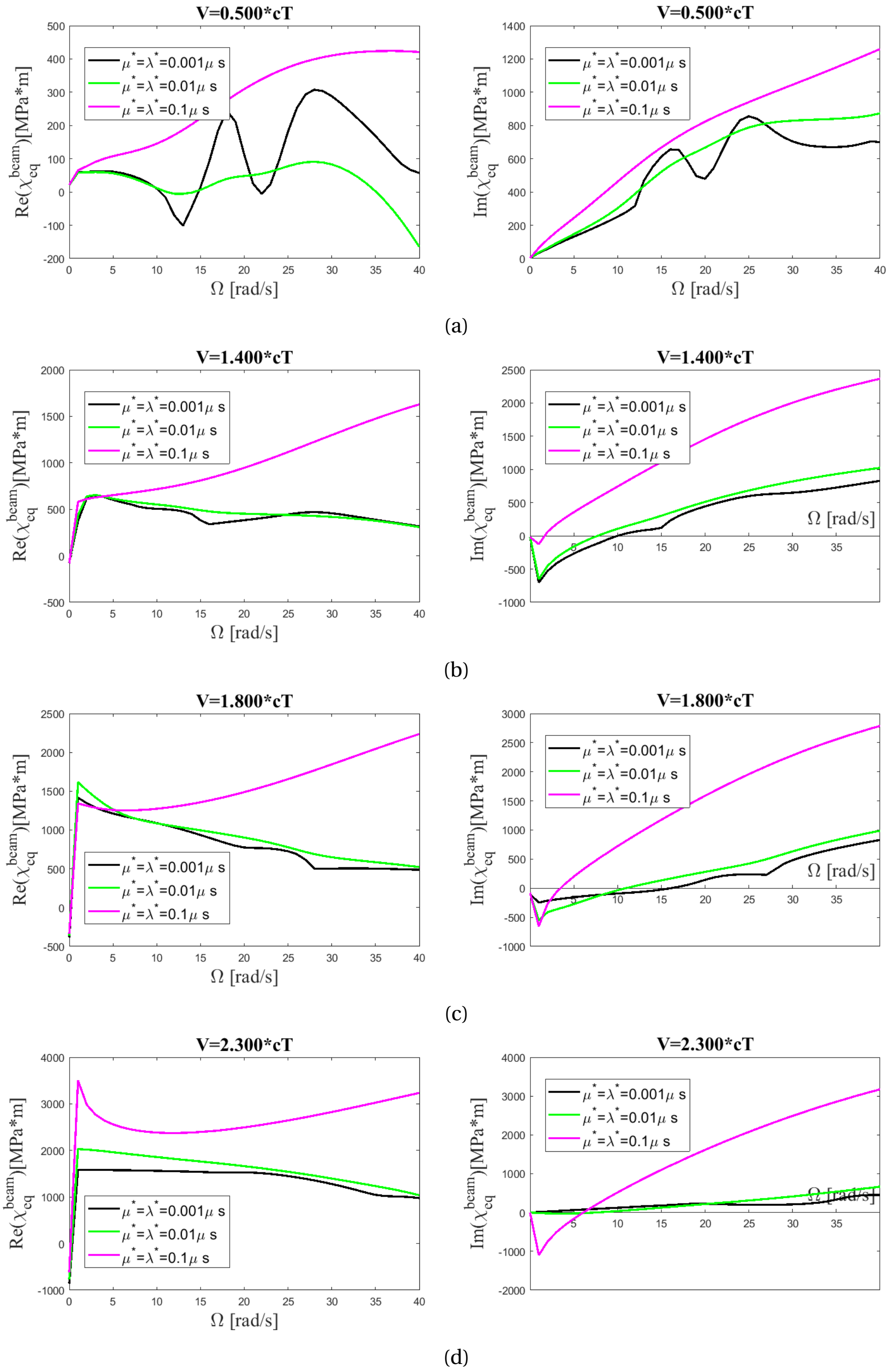

Figure 4.4: Effect of material damping in half-plane: Equivalent dynamic stiffness of the beam embedded in the half-plane versus frequency Ω of the oscillator for (a) $V = 0.5c_T$, (b) $V = 1.4c_T$, (c) $V = 1.8c_T$ and (d) $V = 2.3c_T$.

For an oscillator velocity equal to $1.4c_T$, increasing the material damping magnitude causes the frequency band in which $\Im(\chi_{\text{eq}}^{\text{beam}}) < 0$ to shrink. Moreover, for this velocity the absolute value of $\Im(\chi_{\text{eq}}^{\text{beam}})$ decreases for increasing values of μ^*. When analyzing other velocities, this effect is found for velocities up to about $1.6c_T$. However, for higher vehicle velocities, a higher value of the material damping seems to cause an increase in the absolute value of the imaginary part of the equivalent stiffness for the frequency band where this value is negative. This has been shown in fig. 4.4c for $V = 1.8c_T$. The frequency band where $\Im(\chi_{\text{eq}}^{\text{beam}}) < 0$ is still wider for lower magnitudes of the material damping though. When the velocity is increased to $V = 2.3c_T$, the imaginary part of the equivalent dynamic stiffness is positive everywhere for the lowest material damping value, while for higher magnitudes the dynamic stiffness of the beam embedded in the visco-elastic half-plane has a negative imaginary part for the low frequencies. The larger the material damping, the larger the absolute value of $\Im(\chi_{\text{eq}}^{\text{beam}})$ at the low frequency band. From the analysis of higher velocities and $\mu^* = \lambda^* = 0.01\mu$ s, it follows that the 'negative damping' disappears at $V = 2.5c_T$. Yet, for $\mu^* = \lambda^* = 0.1\mu$ s, $\Im(\chi_{\text{eq}}^{\text{beam}})$ has a negative part even for the highest observed velocity of $2.9c_T$. This is a remarkable result as the material damping in the half-plane seems to have a destabilizing effect for the high vehicle velocities.

4.3. THE INSTABILITY DOMAIN

As mentioned before, a negative imaginary part of the equivalent dynamic stiffness of the beam embedded in the half-plane is a necessary but not a sufficient condition for instability. In what follows, the roots of the characteristic equation 3.49 are studied using the D-decomposition method explained in section 2.2.4. If at least one of the eigenvalues has a positive real part, the vibrations of the oscillator moving along the beam embedded in the visco-elastic half-plane are unstable. For the analysis the parameters in table 4.1 are applied and the material damping is again set to $\mu^* = \lambda^* = 0.001\mu$ s.

4.3.1. INSTABILITY OF A SINGLE MASS ON A BEAM

Let us start with the stability analysis for $m_2 = K = \epsilon_0 = 0$, which is analogous to the case where the beam would be loaded by a uniformly moving single mass only. In that case, the mapping rule for the D-decomposition of the complex m_1-plane is derived from the characteristic equation (eq. (3.49)) as

$$m_1 = \frac{\chi_{\text{eq}}^{\text{beam}}(\Omega)}{\Omega^2}, \tag{4.4}$$

where s has been substituted by iΩ.

D-DECOMPOSITION OF THE m_1-PLANE

The complex roots of the polynomial in eq. (4.4) have been calculated using Matlab R2018a for different values of Ω. Appendix E shows the code for the calculation. The resulting D-decomposition curves for different values of the load velocity V are depicted in fig. 4.5. Only physically possible values of the mass are considered, which means that the analysis focuses on the positive side of the real m_1-axis. As mentioned in references [12, 32], no instability may occur when the magnitude of the single mass goes to zero because then the vibrations of the beam are free. This implies that the system will be stable irrespective the value of m_1 if, starting at $\Re(m_1) = 0$ and going in the positive direction, no crossing points of the D-decomposition line with the real m_1-axis are encountered. In fig. 4.5 the number of roots of eq. (4.4) with a positive real part (from now on referred to as 'unstable' roots) is given by the red numbers. This number changes every time the D-decomposition curve crosses the positive $\Re(m_1)$-axis. The shaded side of the mapping lines corresponds to the right-hand side of the imaginary s-axis. Therefore, crossing it in the direction of the shading means that one more 'unstable'

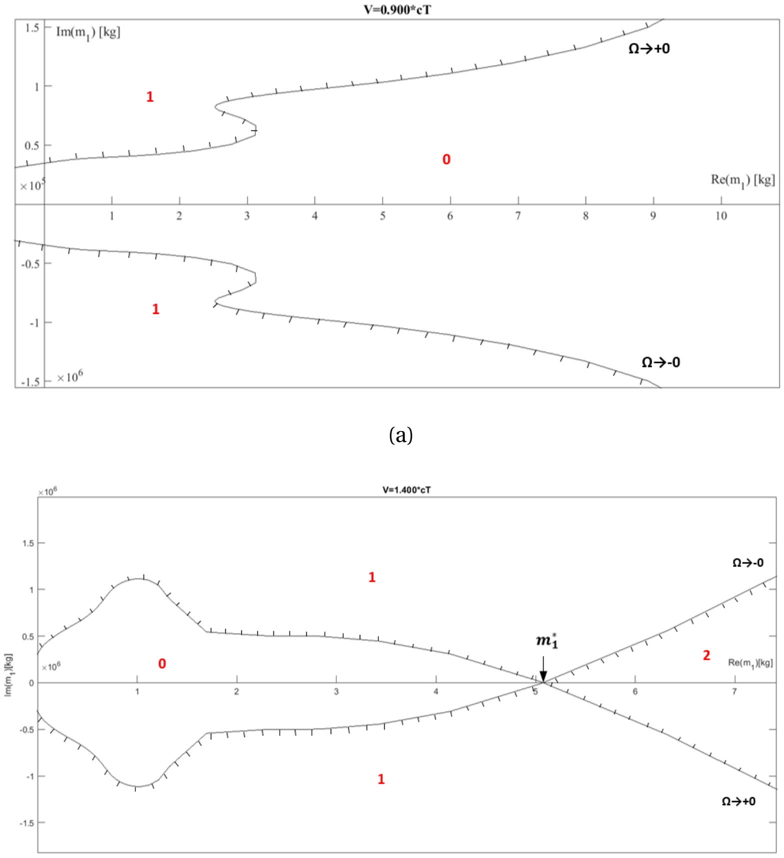

(a)

(b)

Figure 4.5: Separation of the complex m_1-plane into domains with different number of 'unstable roots' (number given in each figure) for (a) sub-critical and (b) super-critical motion of the single mass.

root is obtained.

As demonstrated when analyzing the dynamic stiffness of the beam embedded in the half-plane, for the given parameters and a load velocity $V = 0.9c_T$, the imaginary part of $\chi_{\text{eq}}^{\text{beam}}$ is positive for all frequencies. As explained earlier, the mass vibrations are unconditionally stable when $\Im(\chi_{\text{eq}}^{\text{beam}}) > 0$ for all frequencies. Figure 4.5a indeed shows that the mapped line does not cross the real m_1-axis, which means that for $V = 0.9c_T$ the stability of the system does not depend on the magnitude of the single mass.

Figure 4.5b depicts the super-critical case for which a frequency band exists where $\Im(\chi_{\text{eq}}^{\text{beam}})$ is negative. When tracing the real m_1-axis starting from $m_1 = 0$, the D-decomposition curve intersects this axis twice at a mass magnitude $m_1^* = 5.07 \cdot 10^6$ kg. Taking into account that the vibrations are stable when $m_1 \to 0$, eq. (4.4) has two 'unstable' roots for values of $m_1 > 5.07 \cdot 10^6$ kg. Thus, the mass vibrations are unstable in that case.

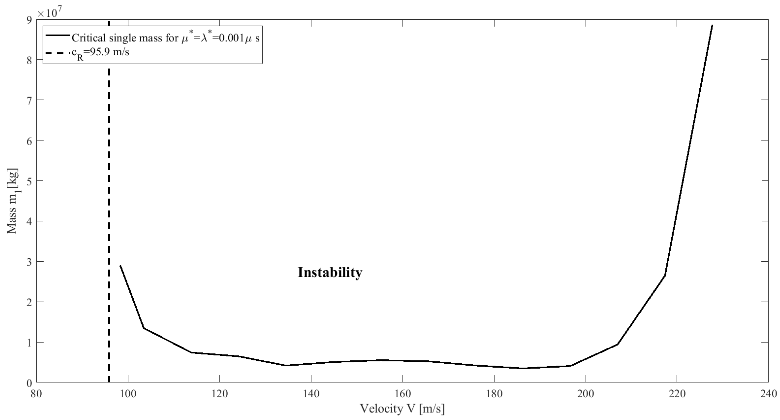

Figure 4.6: Instability region for a uniformly moving single mass.

INSTABILITY DOMAIN

Using the approach outlined above for different values of the velocity, the instability region as function of the velocity can be determined. This has been done in fig. 4.6 where, for different mass velocities, the magnitude of m_1 from which instability first occurs is depicted. The Matlab code for determining the instability domain for the single mass is included in appendix E.

The single mass vibration is always stable for V lower than a critical velocity, which lies slightly above the Rayleigh wave speed. Moreover, the instability domain is bounded at the right by a velocity of approximately 230 m/s. This is due to the material damping in the half-plane [12]. When the elasticity of the oscillator is neglected, instability of vibrations occurs only for unrealistically high magnitudes of the mass, i.e. for a mass magnitude in the order of 10^6 kg or higher.

4.3.2. INSTABILITY OF A TWO-MASS OSCILLATOR ON A BEAM

In what follows, the elasticity of the oscillator is included for the stability study. Now, the parameters m_2, K and ϵ_0 in the characteristic equation are no longer equal to zero. For the D-decomposition, the choice is made to map the imaginary axis of the complex s-plane onto the complex K-plane. Therefore, the characteristic equation is rewritten as a function of K while at the same time s is substituted by iΩ [12]. This results in the mapping rule given by eq. (4.5).

$$K = -\mathrm{i}\epsilon_0\Omega + m_2\Omega^2 \frac{\chi_{\text{eq}}^{\text{beam}}(\Omega) - m_1\Omega^2}{\chi_{\text{eq}}^{\text{beam}}(\Omega) - m_2\Omega^2 - m_1\Omega^2}. \tag{4.5}$$

D-DECOMPOSITION OF THE *K*-PLANE

Table 4.2 gives the initial values of m_1, m_2 and ϵ_0 for which the D-decomposition curves are drawn and the instability domain is derived. Material damping is again set to $\mu^* = \lambda^* = 0.001\mu$ s and the beam and half-plane parameters in table 4.1 are applied.

Again, only the positive and real values of K are physically relevant and therefore only the positive part of the real K-axis is considered. For the sub-critical case ($V = 0.9c_T$) presented in fig. 4.7a, the D-decomposition curve has no crossing points with the positive $\Re(K)$-axis which means that the characteristic equation has no 'unstable roots' and the vibrations of the sub-critically moving oscillator are stable regardless of its stiffness.

Figure 4.7b corresponds to a super-critically moving oscillator. The number of roots with a positive

Parameter	Value	Unit
m_1	2000	kg
m_2	20000	kg
ϵ_0	0	Ns/m

Table 4.2: Oscillator parameters [12].

real part for each domain is indicated in the figure. To determine these numbers, the following reasoning has been applied. When the stiffness of the oscillator K tends to infinity, the masses m_1 and m_2 actually vibrate as one single mass with a value equal to $m_1 + m_2 = (2+20)\cdot 10^3 = 22\cdot 10^3$ kg. As can be derived from fig. 4.6, the system with a single moving mass (neglecting the elasticity of the oscillator) is stable for all studied velocities as long as the total magnitude of the mass is lower than approximately $3.5\cdot 10^6$ kg. Therefore, one can conclude that the system is stable for $\Re(K) \to +\infty$ [12]. In fig. 4.7b the real and positive K-axis is traced starting from infinity and going to $K = 0$ N/m. At an oscillator stiffness $K = K^*$ the D-decomposition curve crosses $\Re(K)$ twice. When this double crossing point is passed in the direction of the shading, the characteristic equation 4.5 has two 'unstable' roots. Up to the origin ($\Re(K) = 0$, $\Im(K) = 0$) there are no more crossing points of the D-decomposition curve with the real K-axis, which means that the domain $K \in [0 \quad K^*]$ corresponds to unstable vibrations.

INSTABILITY DOMAIN AND PARAMETRIC STUDY

As for the case of the single mass moving on the Euler-Bernoulli beam, the instability domain is derived from the D-decomposition curves. In fig. 4.8 the domain of stiffness values for which the vibrations of the oscillator are unstable for the given parameters is indicated. The curve representing the values of the critical stiffness K^* is a bit jagged, because, as denoted in the Matlab code in appendix D, steps of $0.1c_T$ are taken for the oscillator velocity. This is done to reduce the computation time when determining the integral in the expression for $\chi_{\text{eq}}^{\text{beam}}$.
The instability domain starts at an oscillator velocity slightly lower than 100 m/s and, in addition, is bounded from the right due to the effect of the material damping in the half-plane. For the given parameters, the oscillator is unconditionally stable when the vehicle velocity is larger than approximately 230 m/s. As the Hyperloop pod should be able to reach velocities of about 300 m/s, one could conclude that the spring stiffness should be at least $5.2\cdot 10^6$ N/m. However, before drawing conclusions from this single figure, the influence of the model constants on the instability domain should be examined in a parametric study. Therefore, the approach followed in [12] is adopted, repeating the analysis several times while keeping all but one of the parameter values unchanged.

Variation of material damping of the half-plane In first instance the influence of the material damping in the half-plane on the critical oscillator spring stiffness is studied. Figure 4.9 presents the instability domain for three different values of the half-plane viscosity. The effect of an increase in the half-plane material damping on the instability domain is twofold: when the material damping is increased from $\mu^* = \lambda^* = 0.001\mu$ s to $\mu^* = \lambda^* = 0.01\mu$ s, the instability domain expands towards higher oscillator velocities. A further increase to $\mu^* = \lambda^* = 0.1\mu$ s causes the critical velocity at which vibrations first become unstable to increase and in this case, vibrations are unstable up to the highest considered velocity. Thus, it seems that the instability domain shifts to the right due to a rise in the material damping magnitude. At the same time, the increase in the magnitude of the material damping causes the oscillator stiffness K^* for which instability first occurs, to decrease. As mentioned before, there exists a critical material damping for which the system is stable over the whole velocity range.

Variation of half-plane Young's modulus Figure 4.10 depicts the instability domain for different values of the half-plane Young's modulus. On the one hand, the increase of the half-plane stiffness shifts

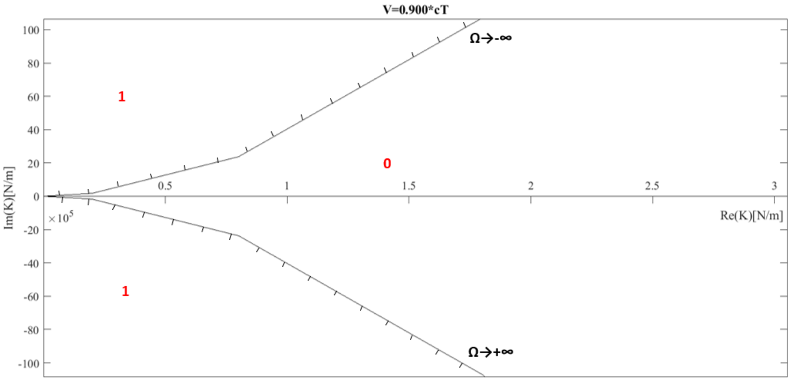

(a)

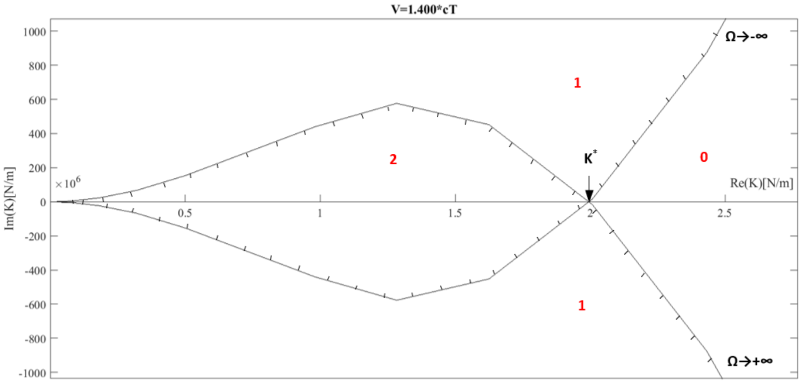

(b)

Figure 4.7: Separation of the complex K-plane into domains with different number of 'unstable roots' (number given in each figure) for (a) sub-critical and (b) super-critical motion of the oscillator.

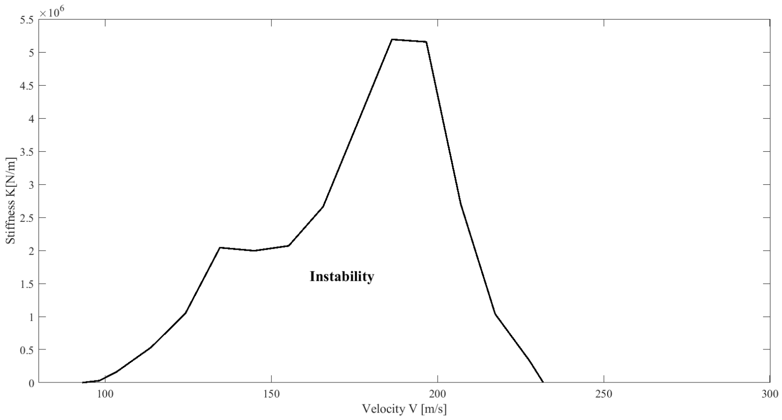

Figure 4.8: Instability region for a uniformly moving two-mass oscillator with stiffness K on a beam embedded in a visco-elastic half-plane.

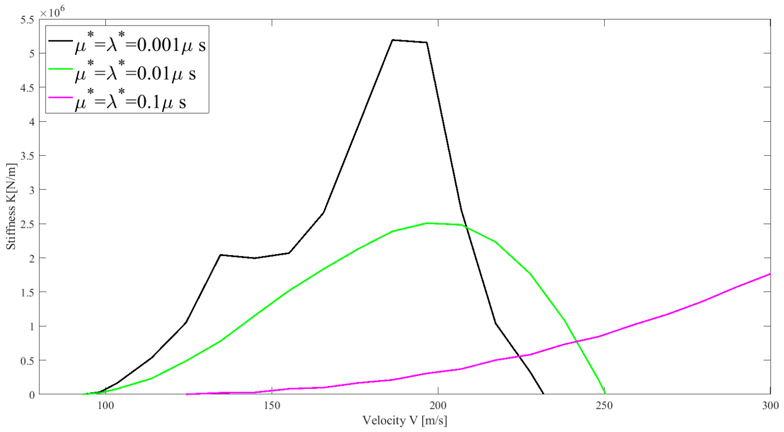

Figure 4.9: Effect of the material damping of the half-plane on the instability domain. The domain located below the curves is the domain of unstable oscillator vibrations.

the right boundary slightly to the right, so the velocity range in which unstable vibrations occur grows. On the other hand however, a rise in the Young's modulus leads also to the shrinkage of the instability domain along the stiffness axis.

Variation of depth of the tube Figure 4.11 depicts the effect of the depth h of the tube on the instability domain. When h is increased, the zone expands along the stiffness axis. For the observed depths of the tube, the critical velocity is similar. At the right however, changing the depth of the tube does affect the bounding velocity. Apparently, when the depth increases from 8 m to 12 m, the instability domain expands along the velocity axis. However, a further increase of the oscillator velocity to $h = 16$ m causes the right boundary to shift towards lower velocities again. One can conclude that the depth of the tube has a destabilizing effect, although varying its magnitude may lead to a shift of the right instability domain boundary towards lower oscillator velocities.

To determine whether the shift of the right boundary of the instability domain is caused by the half-plane-beam system or by the oscillator itself, the critical frequency Ω^* from which $\Im(\chi_{\text{eq}}^{\text{beam}})$ first becomes positive is examined. Figure 4.12 presents the magnitude of this critical frequency over the whole velocity range for the three considered depth magnitudes. From the comparison of fig. 4.11 and fig. 4.12, it follows that the shift of the right instability zone boundary is caused by the supporting structure rather than by the oscillator itself.

Variation of the beam's flexural rigidity Figure 4.13 depicts the instability domain for three different magnitudes of the flexural rigidity of the beam. Stiffening the beam causes the critical velocity to rise but, at the same time, expands the instability domain towards higher velocities. Moreover, with increasing flexural rigidity, the instability domain shrinks along the stiffness axis.

Variation of the mass per unit length of the beam Figure 4.14 shows that increasing the mass per unit length of the beam causes the instability domain to shift towards the lower velocities and to expand along the stiffness axis. As the critical velocity is lower and the stiffness that has to be exceeded to avoid unstable oscillator vibrations is higher for a heavier tube, decreasing the weight of the tube can stabilize the system.

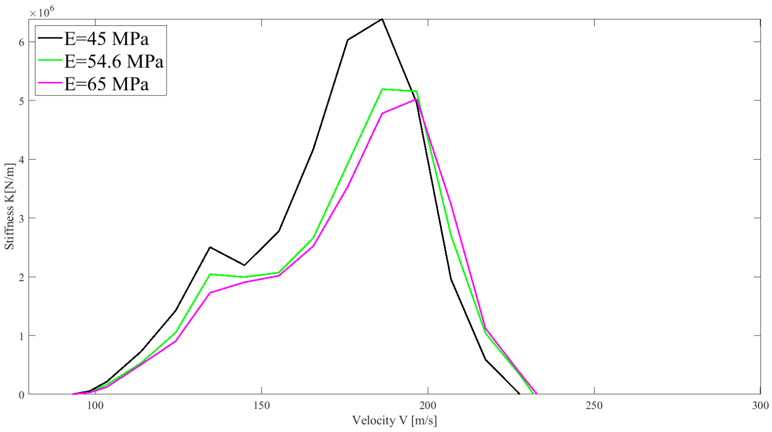

Figure 4.10: Effect of the half-plane Young's modulus on the instability domain. The domain located below the curves is the domain of unstable oscillator vibrations.

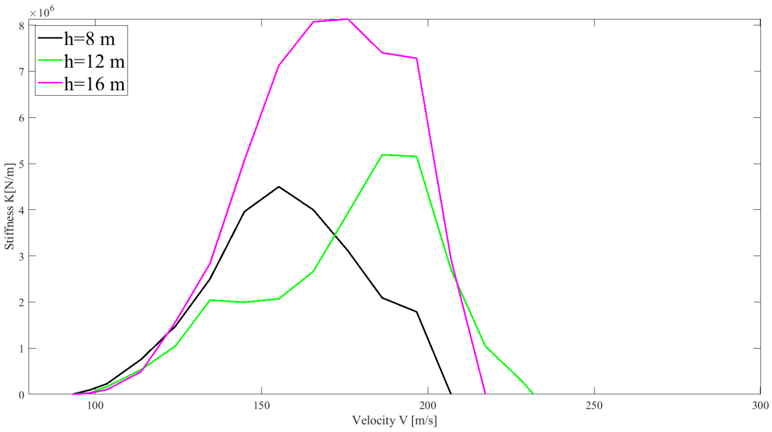

Figure 4.11: Effect of depth of the tube on the instability domain. The domain located below the curves is the domain of unstable oscillator vibrations.

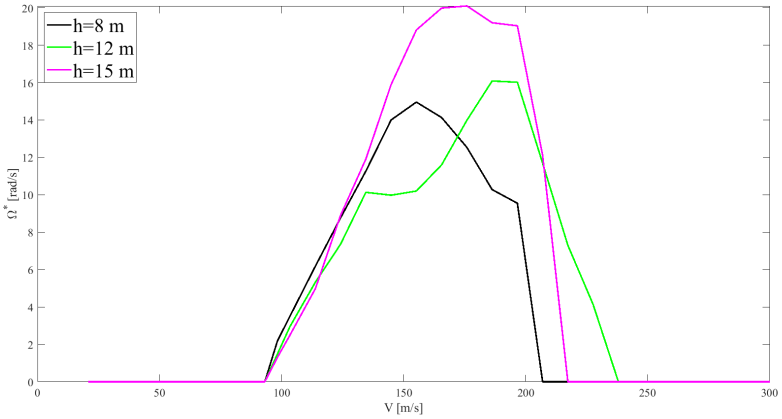

Figure 4.12: Critical frequency Ω^* from which the imaginary part of the equivalent dynamic stiffness of the beam first becomes positive for the given velocity range and different values of the tube depth.

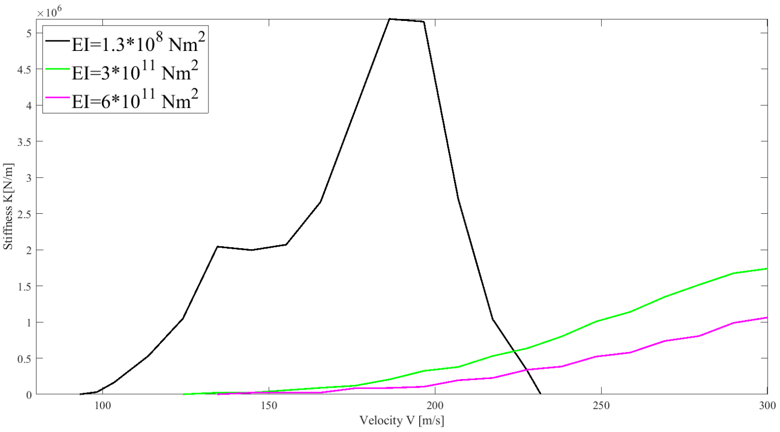

Figure 4.13: Effect of the beam's flexural rigidity on the instability domain. The domain located below the curves is the domain of unstable oscillator vibrations.

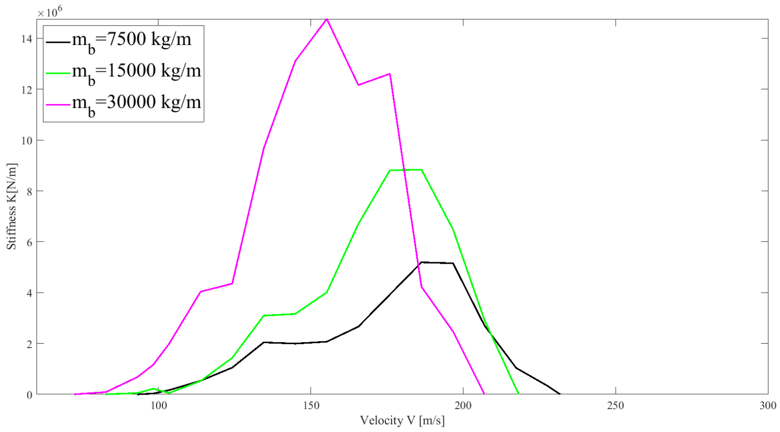

Figure 4.14: Effect of the mass per unit length of the beam on the instability domain. The domain located below the curves is the domain of unstable oscillator vibrations.

Variation of upper mass magnitude As can be derived from fig. 4.15 the upper mass destabilizes the system. Although the bounding velocities of the instability zone are not influenced by the magnitude of the upper oscillator mass, the critical spring stiffness is. As the upper mass destabilizes the system, it is advised to keep the mass of the chassis (=upper mass, see fig. 2.26a) as low as possible to avoid instability of the Hyperloop pod.

Variation of lower mass magnitude From fig. 4.16 one can conclude that the lower mass has (almost) no influence on the shape and location of the instability domain. A logical reason follows from eq. (4.5). As the real part of $\chi_{\text{eq}}^{\text{beam}}$ is in the order of 10^7 or higher, subtracting the rather limited value of m_1 multiplied with the square of Ω, does not significantly impact the mapping rule onto the complex K-plane.

Variation of viscous damping in the oscillator As for the two-mass oscillator moving on a beam *at the surface* supported by a visco-elastic half-space [12], the variation of the damping coefficient of the oscillator changes not only the size but also the shape of the instability domain. This effect is visualized in fig. 4.17. With increasing oscillator viscosity the instability domain shrinks, and, at a rather small viscosity $\epsilon_0 = 75$ Ns/m, the instability domain has already disappeared completely. As discussed before, increasing the magnitude of the material damping can also remove the instability zone, but to that end the material damping needs to be very high. With respect to the viscosity of the oscillator however, the conclusion can be made that this parameter has a very important stabilizing effect as a limited viscosity can make the vertical vibrations of the oscillator unconditionally stable.

4.3.3. INTRODUCTION OF THE HYPERLOOP PARAMETERS

In this last section, the parameters of the Hyperloop pod are inserted in the model. Firstly, only the properties of the Hyperloop pod are taken into account, while for the beam and half-plane the parameters in table 4.1 are applied once again. The material damping in the half-plane is set to $\mu^* = \lambda^* = 0.001\mu$ s. We will consider both the small-scale Hyperloop competition pod, for which the description is given in the final design document of Delft Hyperloop team [15] and a realistic model for a full-scale pod, for which the parameters are based on the specifications of a Maglev train, as described in [42], as well as on the information given in the design document [15]. Finally, the flexural

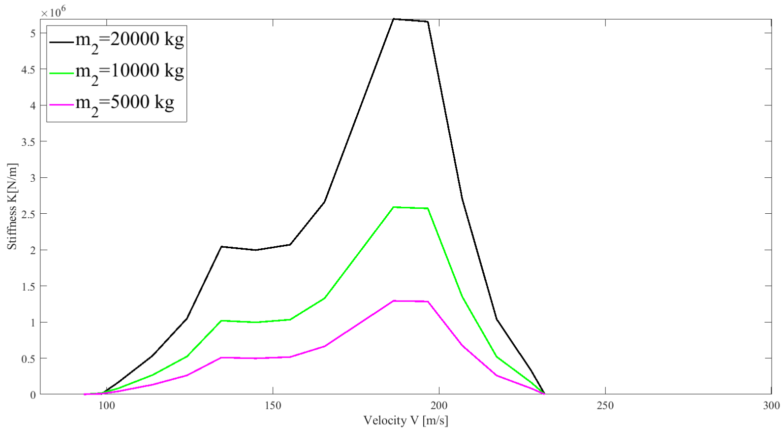

Figure 4.15: Effect of upper mass of the oscillator on the instability domain. The domain located below the curves is the domain of unstable oscillator vibrations.

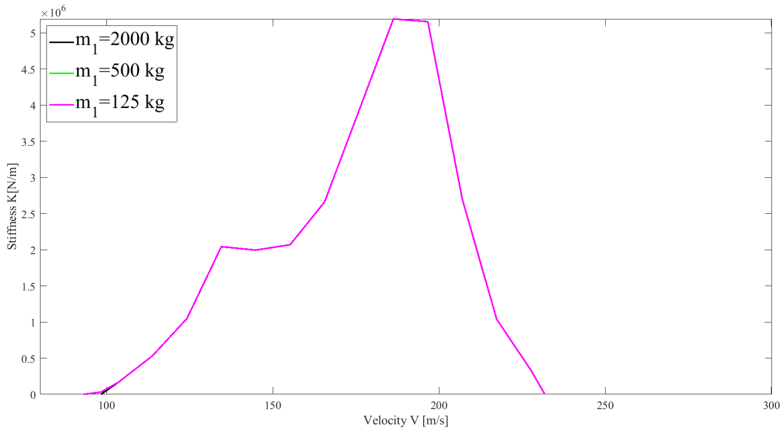

Figure 4.16: Effect of lower mass of the oscillator on the instability domain. The domain located below the curves is the domain of unstable oscillator vibrations.

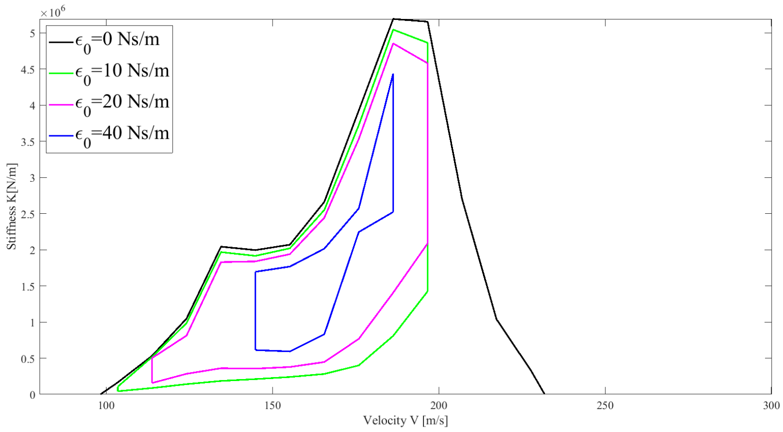

Figure 4.17: Effect of oscillator viscosity on the instability domain. The domain located below the curve for $\epsilon_0 = 0$ Ns/m or within the boundaries determined by the curves for higher values of ϵ_0 is the domain of unstable oscillator vibrations.

Vehicle model	**Parameter**	**Value**	**Unit**
Small-scale competition pod	m_1	62.9	kg
	m_2	113	kg
	K	$1.2 \cdot 10^5$	N/m
	ϵ_0	8228	Ns/m
Full-scale pod	m_1	150	kg
	m_2	10000	kg
	K	$8 \cdot 10^5$	N/m
	ϵ_0	$2 \cdot 10^4$	Ns/m

Table 4.3: Hyperloop pod parameters [15, 42].

rigidity, EI, and mass per unit length, m_b, of a realistic concrete tunnel are introduced and the motion of both the small-scale and full-scale Hyperloop pod on such a beam in the half-plane is analyzed.

HYPERLOOP POD PARAMETERS

The relevant pod parameters for both the competition pod and the full-scale vehicle are presented in table 4.3. The pod has four lifting bogies, each of them containing a spring-damper system. In the studied model, the spring stiffness and damping coefficient are lumped in one spring and one damper respectively and therefore their magnitude, as denoted in [15, 42], is multiplied by four. The upper mass m_2 is determined by the mass of the pod itself. For the full-scale pod the payload (28 passengers, seats, luggage, etc.) is accounted for to obtain the magnitude of m_2. The lower mass m_1 is the mass of the bogies.

Since the properties of beam and half-plane are not changed, the equivalent dynamic stiffness of the beam embedded in the half-plane remains unaltered. As before, the critical oscillator stiffness K^* as a function of pod velocity is determined from the D-decomposition of the K-plane, whereupon the instability domain in the (K, V)-space is derived for the given parameters.

From the analysis of the system's stability, we can conclude that, as the instability domain disappears completely for both for the small-scale and the full-scale pod parameters, the vibrations of both

Tunnel parameter	Value	Unit
I	$\frac{\pi}{2}(2.5^4 - 2.25^4) = 21.1$	m^4
E	$30 \cdot 10^9$	$\mathrm{N/m}^2$
EI	$6.33 \cdot 10^{11}$	Nm^2
m_b	8950	kg/m

Table 4.4: Estimated concrete tunnel parameters.

pods are stable over all velocities.

HYPERLOOP POD AND TUBE PARAMETERS

An estimation remains to be made of the flexural rigidity, EI, and mass per unit length, m_b, of the Hyperloop tube. As an underground Hyperloop tube has not yet been build, a realistic model of the tunnel is chosen by the author. Let us consider a concrete tunnel with an outer radius equal to 2.5 m and an inner radius equal to 2.25 m. The relevant parameters for such a tunnel are given in table 4.4. As this research considers a two-dimensional model of soil and tunnel and the height of the beam is neglected, the tunnel in this model is in fact a plate which extends towards infinity in the out-of-plane direction. This means that the stiffness of a realistic tunnel can in fact not simply be incorporated in a two-dimensional model. However, in what follows, this scaling problem which occurs for any two-dimensional model has been neglected.

The change of the beam parameters influences the value of the equivalent dynamic stiffness of the beam, $\chi_\mathrm{eq}^\mathrm{beam}$. After determining the adapted values for this complex-valued stiffness, the D-decomposition of the K-plane enables the derivation of the instability domain as a function of the oscillator stiffness K and its velocity V. Combining the parameter values for the tube and the Hyperloop vehicle (both small-scale and full-scale) (tables 4.3 and 4.4) with the structural parameters for the half-plane in table 4.1, the instability domain disappears over the whole velocity range from 0 to 300 m/s. This happens for both the competition and full-scale pod. Based on these results, it is tempting to conclude that instability of the pod vibrations should not be expected. However, up to now it has been assumed that during the motion, the lower oscillator's mass stays in contact with the beam. Yet, in reality, the Hyperloop pod is levitated using a non-contact suspension system. The influence of the magnetic levitation system on the system's stability is examined in chapter 5.

5

MODEL OF THE MAGNETIC LEVITATION SYSTEM AND INSTABILITY ANALYSIS

Up to now it has been assumed that the lower mass m_1 remains in contact with the beam during the motion. However, as explained in section 2.2.5, the Hyperloop pods are suspended using a non-contact suspension system. In what follows the influence of the introduction of the electrodynamic suspension system on the instability of the vertical vibrations of the vehicle is studied. For this purpose, the levitation force for the Hyperloop pods moving on a track with coils as in the Inductrack system is inserted in the model. After deriving the characteristic equation for the modified system, the instability is studied by plotting the critical oscillator stiffness K^* versus its velocity V for different values of the oscillator and structural parameters.

5.1. MODEL AND CHARACTERISTIC EQUATION

THE electrodynamic suspension (EDS) system as described in section 2.2.5 is accounted for in the model in fig. 5.1 by introducing the levitation force F_{lift} as described by eq. (2.55). This force is a function of both the uniform pod velocity V and the gap g_1 between the pod bogies and the track. This gap is a function of the displacement of both the lower mass m_1 and the beam. Therefore, eq. (2.55) may be written as

$$\begin{aligned} F_{\text{lift}}(V,x,t) &= 4 * b_{\text{mag}} N_c \frac{B_0 \phi_0}{2L} \frac{1}{1+\left(\frac{R}{\omega_{\text{mag}} L}\right)^2} \exp\Big(-k_{\text{mag}}\Big(g_{\text{nom}} - \big(w_1(x,t) - w_{\text{b}}(x,t)\big)\Big)\Big) \\ &= 4 * b_{\text{mag}} N_c \frac{B_0 \phi_0}{2L} \frac{1}{1+\left(\frac{R}{\omega_{\text{mag}} L}\right)^2} \exp\big(-k_{\text{mag}} g_{\text{nom}}\big) \exp\Big(k_{\text{mag}}\big(w_1(x,t) - w_{\text{b}}(x,t)\big)\Big). \end{aligned} \tag{5.1}$$

As stated in section 2.2.3, the Laplace and Fourier transforms are only applicable in case of a linear statement of the equations of motion. F_{lift} however is nonlinear in w_1 and w_{b} and thus the term $\exp\big(k_{\text{mag}}(w_1 - w_{\text{b}})\big)$ in eq. (2.55) first needs to be linearized. As only the onset of instability is studied in this thesis, $(w_1 - w_{\text{b}})$ will be small. Hence, the first order Taylor approximation around zero may be applied and the exponential term in the expression for F_{lift} is replaced as follows:

$$\exp\big(k_{\text{mag}}(w_1 - w_{\text{b}})\big) \approx 1 + k_{\text{mag}}\big(w_1 - w_{\text{b}}\big). \tag{5.2}$$

This means that the levitation force to be included in the description of the model changes to

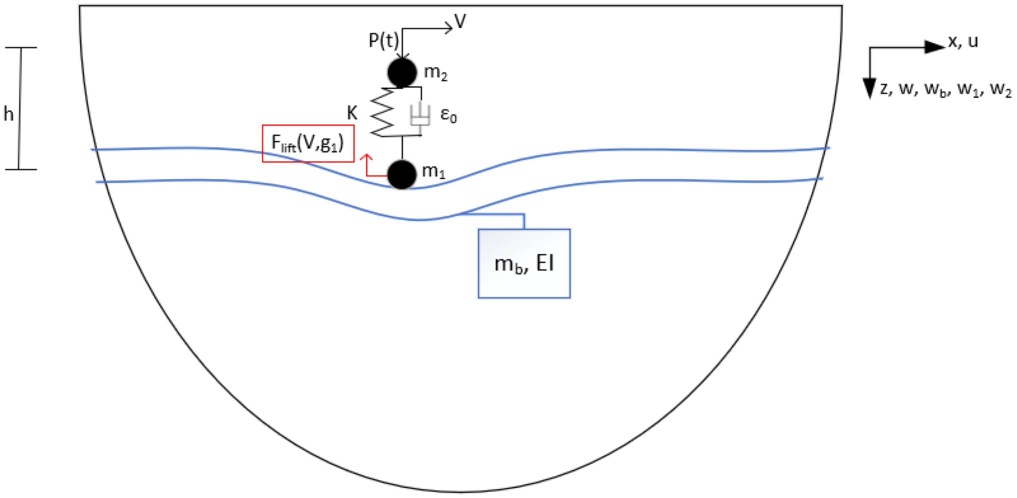

(a)

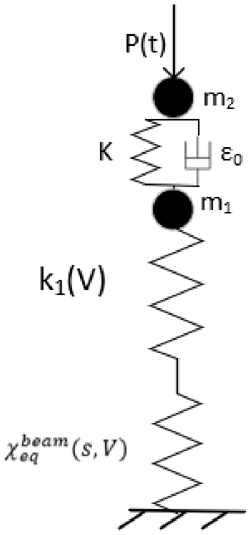

(b)

Figure 5.1: (a) Two-dimensional model of the moving oscillator on the beam including the magnetic levitation suspension system and (b) lumped model of the two-mass oscillator on an equivalent spring $\chi_{\mathrm{eq}}^{\mathrm{beam}}$ with the magnetic levitation force modelled as a spring with stiffness k_1.

$$F_{\text{lift}}(V,x,t) = C_{\text{mag}}(V)\Big(1 + k_{\text{mag}}\big(w_1 - w_{\text{b}}\big)\Big), \tag{5.3}$$

with

$$C_{\text{mag}}(V) = 4 * b_{\text{mag}} N_c \frac{B_0\phi_0}{2L} \frac{1}{1+\left(\frac{R}{\omega_{\text{mag}}L}\right)^2} \exp\left(-k_{\text{mag}} g_{\text{nom}}\right).$$

As has been explained extensively in chapters 2 and 3, the two-dimensional model of the beam-half-plane system can be reduced to the lumped mass-spring-dashpot model depicted in fig. 5.1b by introducing a moving reference system and subsequently applying the Laplace and Fourier integral transforms and defining the equivalent dynamic stiffness of the beam. As the beam-half-plane model remains unchanged as compared to that in chapter 3, $\chi_{\text{eq}}^{\text{beam}}$ is still defined by eq. (3.47). In the model in fig. 5.1b the levitation force F_{lift} is modelled as a magnetic spring with k_1 representing the stiffness of the magnet. The stability of the system is studied when the system is at its equilibrium, therefore the static part of the levitation force (= $C_{\text{mag}}(V)$) is omitted and only the dynamic part remains. According to this reasoning, k_1 is only a function of the uniform vehicle velocity V and is defined as

$$k_1(V) = \frac{F_{\text{lift,dynamic part}}(V,s)}{v_1(s) - v_b(s)} = C_{\text{mag}}(V) k_{\text{mag}}. \tag{5.4}$$

5

To study the stability of the system that accounts for the electrodynamic suspension system, the characteristic equation first needs to be derived. Referring to fig. 5.1b, the equations of motion for the system in the Laplace domain are determined as follows:

- EOM for the beam:

$$\big(\chi_{\text{eq}}^{\text{beam}}(s,V) + k_1(V)\big) v_b(s) - k_1(V) v_1(s) = 0, \tag{5.5}$$

- EOM for the lower mass:

$$m_1 s^2 v_1(s) + k_1(V)\big(v_1(s) - v_b(s)\big) + \big(K + \epsilon_0 s\big)\big(v_1(s) - v_2(s)\big) = 0, \tag{5.6}$$

- EOM for the upper mass:

$$m_2 s^2 v_2(s) + \big(K + \epsilon_0 s\big)\big(v_2(s) - v_1(s)\big) = p(s). \tag{5.7}$$

In eq. (5.5) the displacement of the beam v_b is considered in the contact point with the moving oscillator and therefore this variable is only a function of the Laplace s. By solving eq. (5.5) for $v_b(s)$ in terms of $v_1(s)$ the following equations are obtained:

- EOM for the lower mass:

$$\Big(m_1 s^2 + \frac{k_1(V)\chi_{\text{eq}}^{\text{beam}}(s,V)}{k_1(V) + \chi_{\text{eq}}^{\text{beam}}(s,V)} + K + \epsilon_0 s\Big) v_1(s) - \big(K + \epsilon_0 s\big) v_2(s) = 0, \tag{5.8}$$

- EOM for the upper mass:

$$\big(m_2 s^2 + K + \epsilon_0 s\big) v_2(s) - \big(K + \epsilon_0 s\big) v_1(s) = p(s). \tag{5.9}$$

In matrix form, the above system of equations becomes

$$\begin{bmatrix} m_1 s^2 + \frac{k_1(V)\chi_{\text{eq}}^{\text{beam}}(s,V)}{k_1(V)+\chi_{\text{eq}}^{\text{beam}}(s,V)} + K + \epsilon_0 s & -K + \epsilon_0 s \\ -K + \epsilon_0 s & m_2 s^2 + K + \epsilon_0 s \end{bmatrix} \begin{bmatrix} v_1(s) \\ v_2(s) \end{bmatrix} = \begin{bmatrix} 0 \\ p(s) \end{bmatrix} \tag{5.10}$$

and by setting the determinant of the coefficient matrix in eq. (5.10) equal to zero, the characteristic equation is obtained as

$$\left(m_1 s^2 + K + \epsilon_0 s + \chi'\right)\left(m_2 s^2 + K + \epsilon_0 s\right) - \left(K + \epsilon_0 s\right)^2 = 0. \tag{5.11}$$

In eq. (5.11), χ' is the equivalent stiffness of the two springs $\chi_{\text{eq}}^{\text{beam}}$ and k_1 acting in series and is defined as

$$\chi'(s, V) = \frac{k_1(V)\chi_{\text{eq}}^{\text{beam}}(s, V)}{k_1(V) + \chi_{\text{eq}}^{\text{beam}}(s, V)}. \tag{5.12}$$

5.2. INSTABILITY ANALYSIS

BEFORE the system's stability can be studied, the parameters of the magnetic field need to be determined. Then, analogous to the procedure followed in section 4.3.1, the stability of a single mass moving on the embedded beam is examined. For velocities from 0 to 300 m/s, the smallest magnitude of the oscillator's lower mass from which the system becomes unstable is derived. Once this magnitude has been determined, the D-decomposition of the K-plane gives the domain of unstable vehicle vibrations for the considered parameters.

To establish the effect of the introduction of the magnetic levitation system in the model, firstly the instability of the uniformly moving single mass is studied for electrodynamic suspension system, beam and half-plane parameters as given in tables 4.1, 5.1 and 5.2. Then the beam parameters are changed to those for a normal strength concrete tunnel (table 4.4), while, at the same time, introducing the masses m_1 and m_2 of both the competition vehicle and the full-scale Hyperloop pod given in table 4.3. A third analysis considers the effect of using high-strength concrete for the construction of the tunnel. For both the normal strength and high-strength concrete tunnel, the zones of unstable vehicle vibrations are derived for the uniformly moving mass as well as for the two-mass moving oscillator, for which the relevant properties are given in table 4.3. Finally, the viscosity of the oscillator is introduced and its effect is examined for both the normal strength and high-strength concrete tunnel.

For the normal strength and high strength concrete tunnel, the remark made in section 4.3.3 has to be kept in mind: as this report considers a two-dimensional model, the stiffness of a realistic tunnel can in fact not simply be incorporated in the model where the tunnel is an infinite plate rather than a real tube.

5.2.1. PARAMETERS OF THE MAGNETIC FIELD

The final design document of Delft Hyperloop [15] discusses the design of a small-scale pod for which the suspended mass is rather limited. As the suspended mass of the full-scale pod is considerably higher, the magnetic levitation force needs to be increased as well. Thus, the properties of the magnetic levitation suspension system for both vehicle models are different.

The Halbach array for the competition pod is presented in fig. 2.24b. This figure gives the dimensions and wavelength of the permanent magnet array. The magnitude of the nominal gap between the pod and the track is set to 23 mm. To establish the inductance and resistance of the track, the small-scale Inductrack model in reference [43] is considered. Its parameters, and those of the Halbach arrays on the competition pod, are denoted in table 5.1. To determine the electrical resistivity of the coils in the track, aluminium wires are assumed.

When the properties in this table are inserted in eqs. (2.54a) and (2.54b) the inductance, L, and the

System part	Parameter	Value	Unit
Hyperloop pod Halbach array	λ_{mag}	0.36	m
	k_{mag}	$\frac{2\pi}{\lambda_{\text{mag}}} = 17.45$	m^{-1}
	b_{mag}	0.05	m
	h_{mag}	0.02	m
Track	μ_0	$4\pi \cdot 10^{-7}$	H/m
	d_c	$16 \cdot 10^{-3}$	m
	P_c	$508 \cdot 10^{-3}$	m
	A_c	$2 \cdot 10^{-4}$	m^2
	ρ_r	$2.65 \cdot 10^{-8}$	Ω m
	N_c	$\frac{\lambda_{\text{mag}}}{d_c} = 22$	-

Table 5.1: Small-scale Hyperloop pod permanent magnet and Inductrack parameters [15, 43].

System part	Parameter	Value	Unit
Hyperloop pod Halbach array	λ_{mag}	0.6	m
	k_{mag}	$\frac{2\pi}{\lambda_{\text{mag}}} = 10.47$	m^{-1}
	b_{mag}	0.3	m
	h_{mag}	0.15	m
Track	μ_0	$4\pi \cdot 10^{-7}$	H/m
	d_c	$25 \cdot 10^{-3}$	m
	P_c	1	m
	A_c	$1 \cdot 10^{-3}$	m^2
	ρ_r	$2.65 \cdot 10^{-8}$	Ω m
	N_c	$\frac{\lambda_{\text{mag}}}{d_c} = 24$	-

Table 5.2: Full-scale Hyperloop pod permanent magnet and Inductrack parameters [43].

resistance, R, of the track are obtained:

$$L = \frac{\mu_0 P_c}{2 k_{\text{mag}} d_c} = \frac{4\pi \cdot 10^{-7} * 508 \cdot 10^{-3}}{2 * 17.45 * 16 \cdot 10^{-3}} = 1.14 \cdot 10^{-6} [\text{H}], \tag{5.13a}$$

$$R = \frac{\rho_r P_c}{A_c} = \frac{2.65 \cdot 10^{-8} * 508 \cdot 10^{-3}}{2 \cdot 10^{-4}} = 6.7 \cdot 10^{-5} [\Omega]. \tag{5.13b}$$

For a full-scale vehicle, the inductance and resistance are derived in the same way. In this case however, the dimensions of the permanent magnet array and of the track coils are larger. Furthermore, the distance between the track coils increases. Table 5.2 presents the relevant parameters as derived from reference [43].

For the full-scale pod the inductance and resistance are obtained as follows:

$$L = \frac{4\pi \cdot 10^{-7} * 1}{2 * 10.47 * 25 \cdot 10^{-3}} = 2.4 \cdot 10^{-6} [\text{H}], \tag{5.14a}$$

$$R = \frac{2.65 \cdot 10^{-8} * 1}{1 \cdot 10^{-3}} = 2.65 \cdot 10^{-5} [\Omega]. \tag{5.14b}$$

In accordance with the approach in reference [43], the nominal gap g_{nom} for the full-scale model is set to 50 mm. For both the small-scale and full-scale case, the peak strength of the magnetic field at the surface of the Halbach arrays (=B_0) is set to one Tesla.

The parameters of the magnetic field determine the stiffness k_1 of the magnetic spring in fig. 5.1b. The dependency of this spring stiffness on the velocity V is depicted in figs. 5.2a and 5.2b for the small-scale model on the one hand and the full-scale model on the other hand.

5.2.2. INSTABILITY OF A SINGLE MOVING MASS

For the analysis of the stability of the single moving, magnetically suspended mass on the beam, the rule for the mapping of the imaginary axis of the complex s-plane onto the complex m_1-plane given in eq. (4.4) changes to

$$m_1 = \frac{\chi'(\Omega)}{\Omega^2}. \tag{5.15}$$

ORIGINAL MODEL

For the properties of the magnetic levitation suspension system denoted in section 5.2.1 and those of the beam and the half-plane presented in table 4.1, the instability domains for the small-scale and full-scale model as derived from the D-decomposition of the complex m_1-plane are depicted in fig. 5.3.

In fig. 5.3 the lowest magnitude of the single mass for which instability starts is indicated. Let us compare this figure to fig. 4.6. We can conclude that, though the width of the instability domain is not influenced, the critical mass magnitude reduces sharply due to the introduction of the magnetic levitation suspension system. Moreover, the obtained instability zone depends strongly on the magnetic field parameters:

- minimum critical single mass magnitude for the small-scale track: 167.1 kg,
- minimum critical single mass magnitude for the full-scale track: 2441 kg.

The downward shift of the instability domain is caused by the fact that the equivalent spring, $\chi_{\text{eq}}^{\text{beam}}$, is placed in series with the considerably more flexible magnetic spring, k_1.

MODEL WITH NORMAL STRENGTH CONCRETE TUNNEL

Figure 5.4 presents the domain for unstable single mass vibrations when the flexural rigidity and mass per unit length of the beam are changed to that of a normal strength concrete tunnel (table 4.4).

Due to the change in the properties of the beam, both the critical velocity and the critical single mass magnitude increase (as compared to those for the original model). Instability of vibrations first occurs at a velocity of approximately 140 m/s and the lowest critical mass magnitudes are:

- for the small-scale track: 806.2 kg,
- for the full-scale track: 11770 kg.

MODEL WITH HIGH-STRENGTH CONCRETE TUNNEL

Finally, the case of a single mass moving on an embedded beam with EI and m_b set to realistic values of a high-strength concrete tunnel, is examined. The outer radius of the tunnel is again set to 2.5 m, while the inner radius is now 2.35 m, as high-strength concrete enables the construction of thinner tunnel linings. The parameters for the beam are presented in table 5.3.

From fig. 5.5 one can conclude that the construction of a thinner, high-strength concrete tunnel does not influence the critical velocity significantly. However, it does cause the critical mass magnitude to decrease as compared to the values obtained for the normal strength concrete tube:

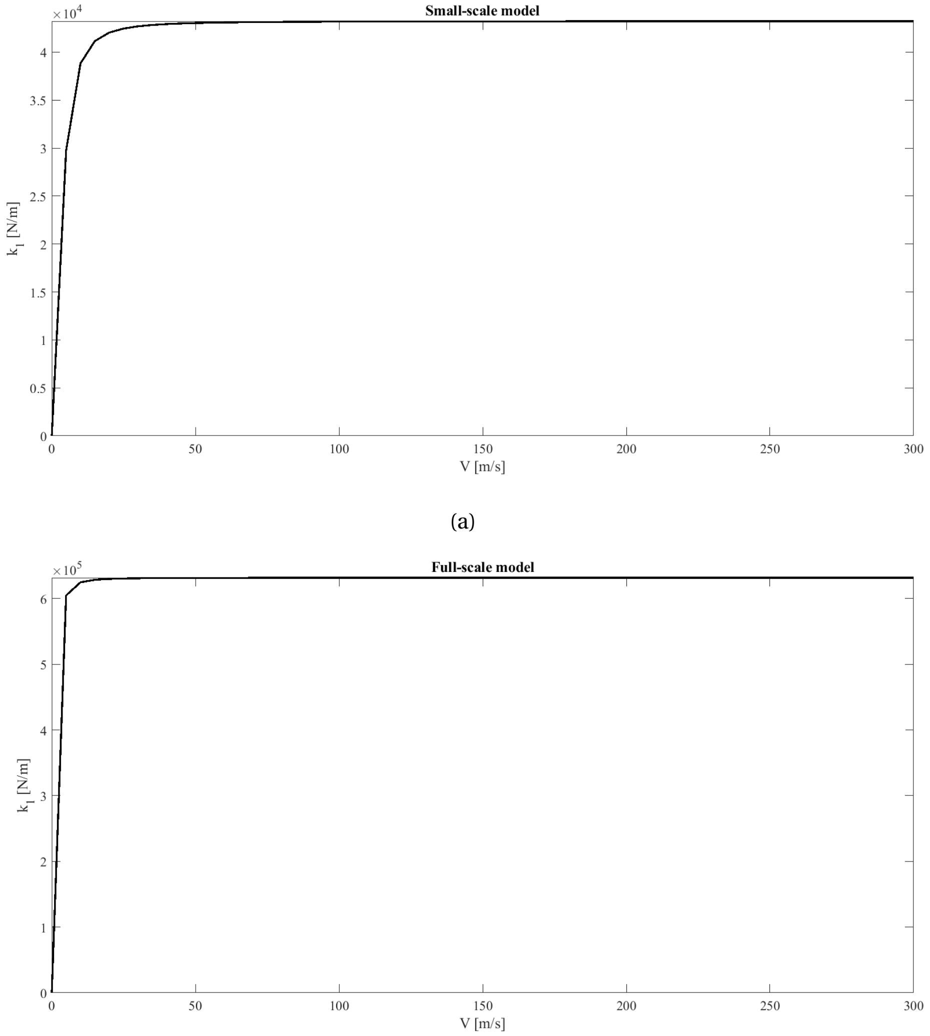

(a)

(b)

Figure 5.2: Dependency of the magnetic spring stiffness k_1 on the uniform vehicle velocity V for (a) a small-scale and (b) a full-scale model of pod and track for which the parameters are given in tables 5.1 and 5.2.

Tunnel parameter	**Value**	**Unit**
I	$\frac{\pi}{2}(2.5^4 - 2.35^4) = 13.45$	m^4
E	$42 \cdot 10^9$	$\mathrm{N/m}^2$
EI	$5.65 \cdot 10^{11}$	Nm^2
m_b	6170	kg/m

Table 5.3: Estimated high-strength concrete tunnel parameters.

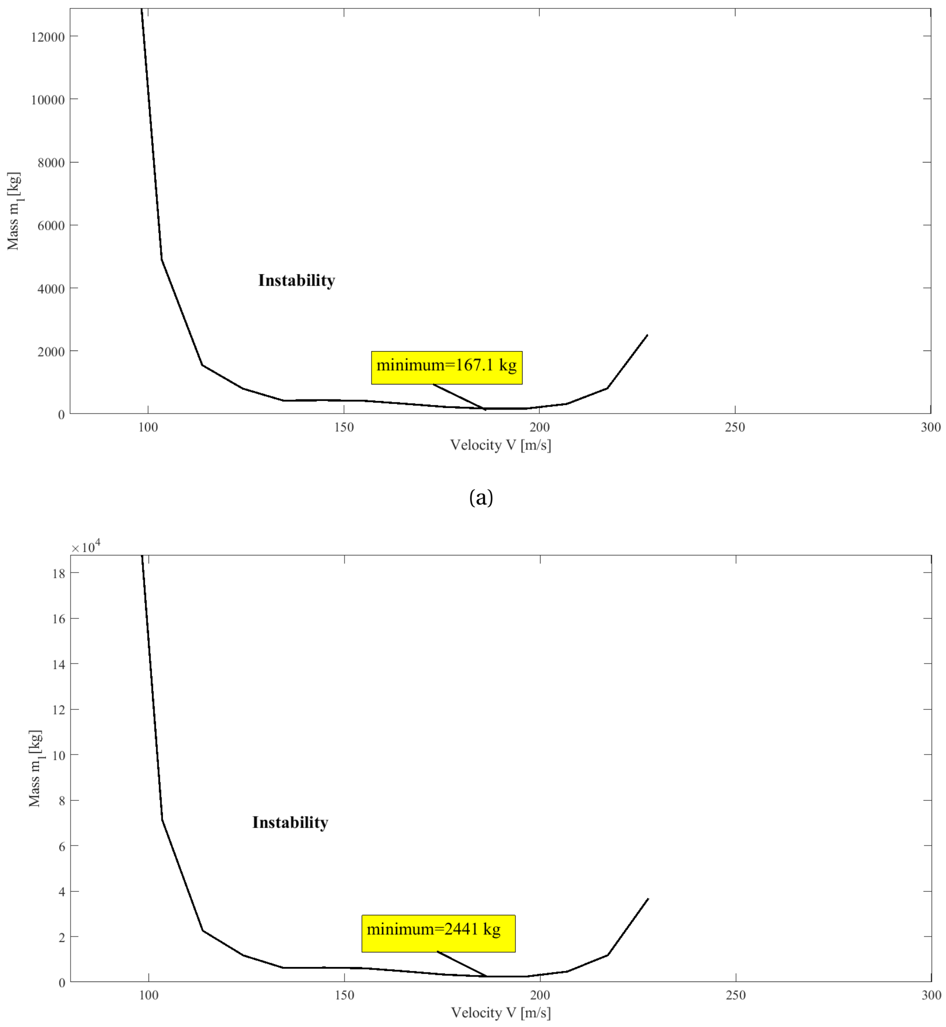

(a)

(b)

Figure 5.3: Instability region for a magnetically levitated uniformly moving single mass on (a) a small-scale and (b) a full-scale track based on the parameters of the original model given in table 4.1.

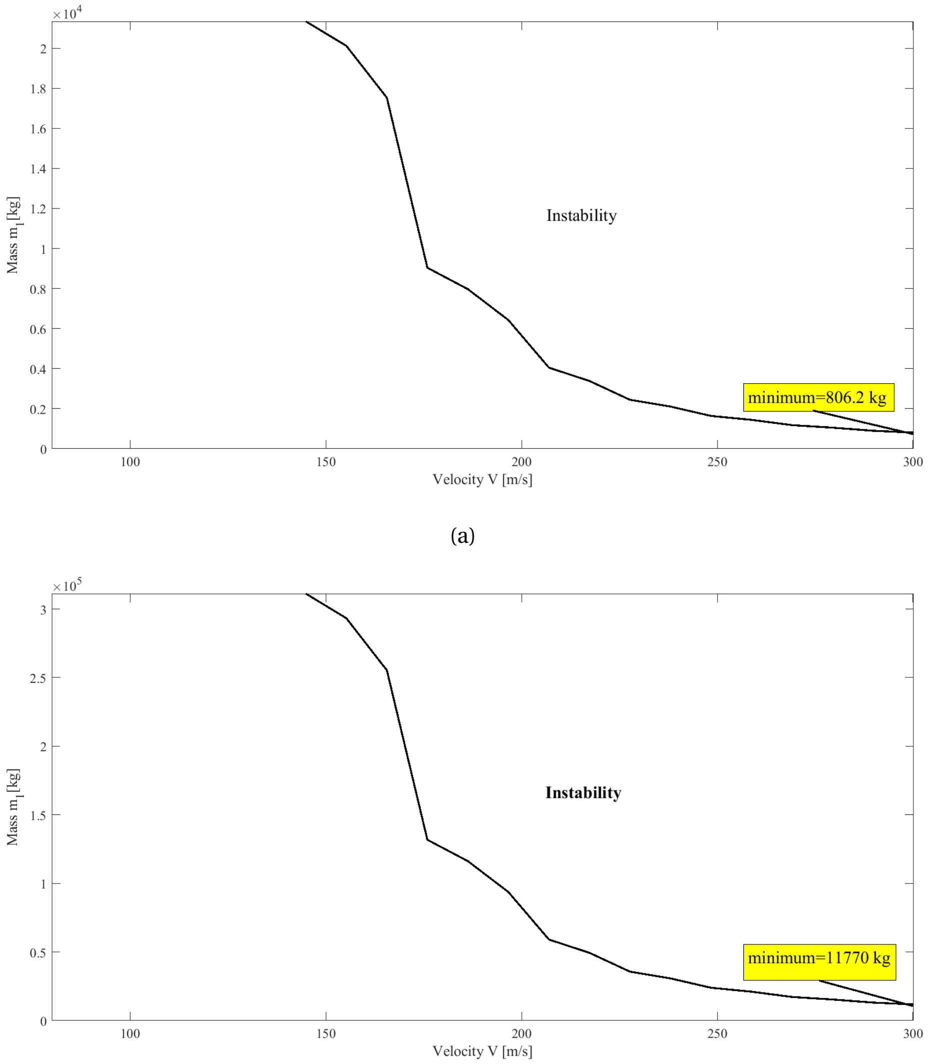

(a)

(b)

Figure 5.4: Instability region for a magnetically levitated uniformly moving single mass on (a) a small-scale and (b) a full-scale track based on the parameters of the normal strength concrete tube (table 4.4), while the parameters of the half-plane are taken from table 4.1.

- for the small-scale track: critical single mass magnitude = 764.8 kg,
- for the full-scale track: critical single mass magnitude = 11170 kg.

5.2.3. INSTABILITY OF THE HYPERLOOP POD

The mapping rule for the D-decomposition of the complex K-plane reads

$$K = -\mathrm{i}\epsilon_0\Omega + m_2\Omega^2 \frac{\chi'(\Omega) - m_1\Omega^2}{\chi'(\Omega) - m_2\Omega^2 - m_1\Omega^2}, \tag{5.16}$$

where the Laplace s has been replaced by iΩ.

The conclusions with respect to the instability of the uniformly moving single mass on the beam have an impact on the instability analysis of the oscillator moving on the beam embedded in a half-plane. With respect to the D-decomposition of the K-plane, the system is stable for an oscillator stiffness tending to infinity, as long as the total mass magnitude of the oscillator is lower than the critical single mass magnitude. This has been explained in section 4.3.2. In other words, for velocities where the latter value is lower than the sum of the masses of the oscillator, the system is **unstable** for $\Re(K) \to +\infty$. Therefore, as the introduction of the electrodynamic suspension system in the model greatly reduces the critical magnitude of the uniformly moving single mass, there is a danger in increasing the vehicle mass. Especially for the high velocities this may strongly affect the instability domain. This section will study the instability of vibrations of both the competition pod and full-scale Hyperloop pod moving in a normal strength and high-strength concrete tunnel respectively.

MODEL WITH NORMAL STRENGTH CONCRETE TUNNEL

From combining table 4.3 with the conclusions of section 5.2.2, we can derive that, for the normal strength concrete tunnel, the minimum critical mass magnitude for both the small-scale and full-scale model is higher than the total mass of the pod, which is found as the sum of m_1 and m_2. Therefore, when performing the D-decomposition of the complex K-plane, the system is stable for $\Re(K) \to +\infty$. The D-decomposition of the K-plane for sub-critical and super-critical motion of the full-scale pod on a full-scale track is depicted in appendix F.

Based on the D-decomposition, the instability domain is found. Figure 5.6 shows the zone of unstable vehicle vibrations for both the small-scale and full-scale model of Hyperloop pod and track.

For both the small-scale and full-scale model, the critical velocity for instability of vibrations is about 140 m/s and the magnitude of the critical oscillator stiffness rises monotonically up to the highest considered velocity of 300 m/s.

In the absence of damping in the oscillator, the spring stiffness of the competition pod needs to exceed the value of 6870 N/m for the vibrations to remain stable over the complete velocity range. From section 4.3.3, we know that the lumped spring stiffness of the Hyperloop pod as designed by Delft Hyperloop, is equal to $1.2 \cdot 10^5$ N/m. Hence, according to this analysis, the vibrations of the vehicle are stable for all velocities up to 300 m/s, even when the viscosity of the oscillator is not accounted for.

From fig. 5.6b, it can be seen that the vibrations of the full-scale pod moving on the full-scale track in the normal strength concrete tunnel are stable for all considered velocities when the stiffness of the oscillator spring is higher than $2.17 \cdot 10^6$ N/m. As the spring stiffness of the full-scale pod is assumed to have a magnitude of $8 \cdot 10^5$ N/m, in the absence of damping in the vehicle, the pod vibrations are unstable for velocities higher than approximately 268 m/s.

MODEL WITH HIGH-STRENGTH CONCRETE TUNNEL

From table 4.3 and fig. 5.5 it follows that, for all considered velocities, both vehicle models have a total mass below the critical magnitude of the uniformly moving single mass. Yet, for high velocities, the

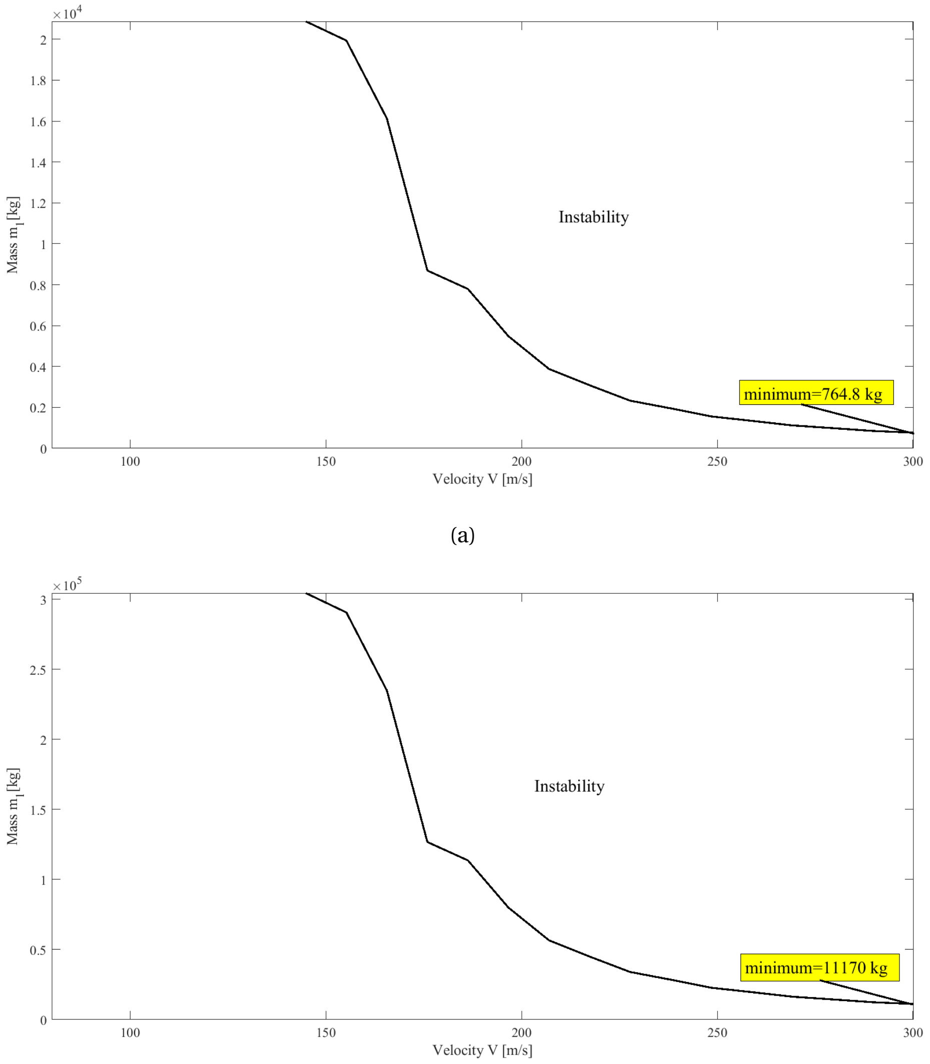

(a)

(b)

Figure 5.5: Instability region for a magnetically levitated uniformly moving single mass on (a) a small-scale and (b) a full-scale track based on the parameters of the high-strength concrete tube (table 5.3), while the parameters of the half-plane are taken from table 4.1.

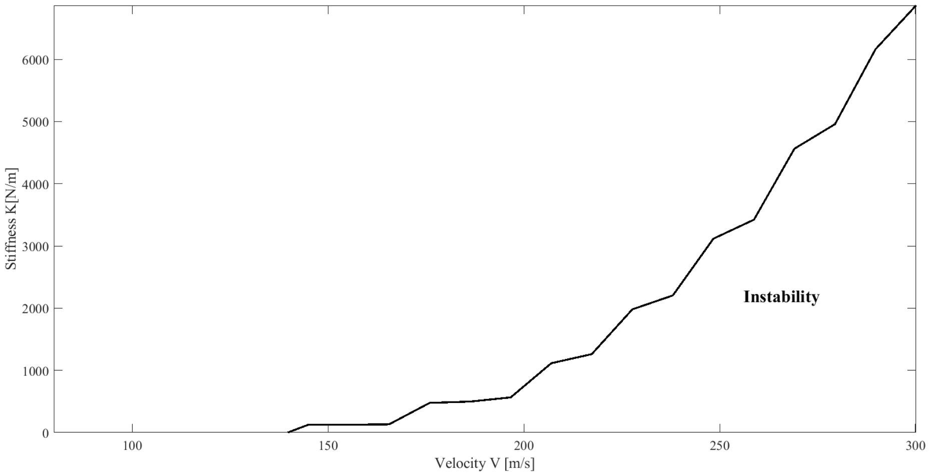

(a)

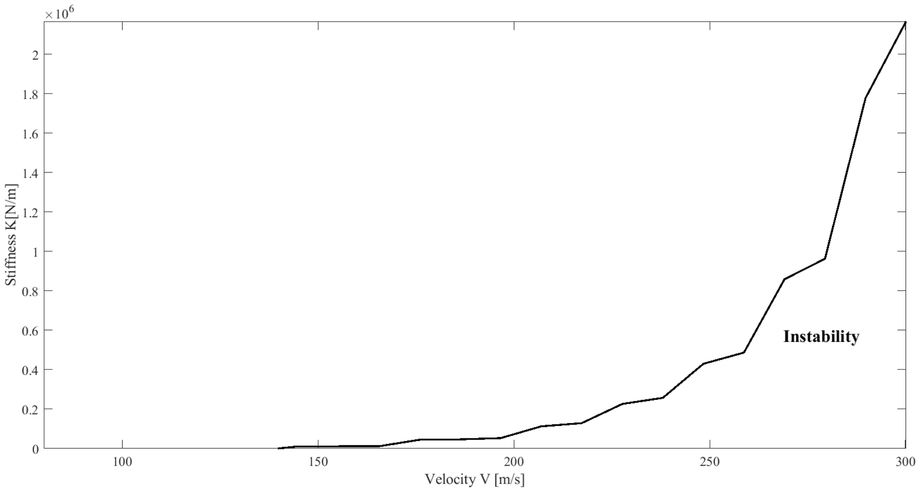

(b)

Figure 5.6: Instability region for a magnetically levitated uniformly moving (a) competition pod on a small-scale track and (b) full-scale Hyperloop pod on a full-scale track respectively, based on the parameters of the normal strength concrete tube (table 4.4), while the parameters of the half-plane are taken from table 4.1.

total mass of the full-scale pod lies only slightly below the critical single mass magnitude. The analysis below is carried out, assuming that the values of m_1 and m_2 in table 4.3 are upper limit values of the masses of the vehicle. If, especially for the full-scale pod, the mass would be higher, this could have a strong impact on the zone of unstable vibrations.

The velocity at which instability first occurs is identical for both the small- and full-scale model of pod and track. As for the normal-strength concrete tunnel, the critical velocity is approximately 140 m/s. For the vibrations to remain stable over all considered velocities, the spring stiffness of the small-scale pod should exceed the magnitude of 7241 N/m, while that of the full-scale pod should be larger than $2.25 \cdot 10^6$ N/m. These critical values of the spring stiffness K slightly surpass the values obtained for the normal strength concrete tunnel. One can conclude that, in case viscous damping in the vehicle is absent, the small-scale system is stable over the whole velocity range, while unstable vibrations of the full-scale pod moving along the full-scale track occur for large velocities. More specifically, from a velocity V of approximately 266 m/s, the full-scale system becomes unstable.

EFFECT OF THE OSCILLATOR'S VISCOSITY

Up to now, the viscous damping in the Hyperloop pod has not been taken into account. For the model without electrodynamic suspension system it was found that the viscous damping in the oscillator has an important stabilizing effect on the system. Moreover, the full-scale vehicle without dashpot and with the spring stiffness as defined in table 4.3, becomes unstable when high velocities are reached. Therefore, the final section of this chapter investigates the effect of the oscillator's viscosity on the vehicle vibrations for the both the small-scale and full-scale model of pod and track. In first instance, the normal strength concrete tunnel is considered again, whereupon the beam parameters EI and m_b are changed to match those of a high-strength concrete tube.

Model with normal strength concrete tunnel Figure 5.8 shows the effect of the viscous damping for the small- and full-scale model of vehicle and track respectively. Analogously to the results found for the model without the magnetic levitation suspension system, the oscillator's viscosity changes both the size and the shape of the instability domain. For both the small-scale and the full-scale model, the zone of unstable vehicle vibrations shrinks rapidly.

For the competition pod moving on the small-scale track, the instability domain disappears completely from a value $\epsilon_0 = 7.7 \cdot 10^{-4}$ Ns/m. As the viscous damping in the competition pod is set to 8228 Ns/m, based on this analysis, instability of vibrations of the competition pod moving in a small-scale Inductrack system in a normal strength concrete tunnel should not be expected.

With respect to the full-scale model, the zone of unstable vehicle vibrations disappears at a somewhat higher level of the damping coefficient, i.e. from $\epsilon_0 = 80$ Ns/m. This magnitude of the viscous damping is considerably lower than that of a maglev train, for which a realistic damping coefficient is given in table 4.3. Thus, also for the magnetically suspended full-scale pod moving in a full-scale Inductrack system in a normal strength concrete tunnel, unstable pod vibrations are not likely to occur.

Model with high-strength concrete tunnel Figure 5.9 presents the effect of the viscous damping for the case where the vehicle is moving through a high-strength concrete tunnel. These figures are very similar to the ones for the normal strength concrete tunnel. Yet, the instability domain shrinks at a slightly slower pace. For the small scale model, the instability domain disappears completely for $\epsilon_0 = 7.9 \cdot 10^{-4}$ Ns/m. For the full-scale model, the system is stable over all velocities and for all values of the stiffness once the magnitude of the viscous damping is larger than approximately 90 Ns/m. For both the small-scale and full-scale model these values of the damping coefficient in the vehicle are still considerably lower than the viscosity given in table 4.3. Therefore, also for the high-strength concrete tunnel, unstable vibrations of the pods moving in the Inductrack system should not be expected.

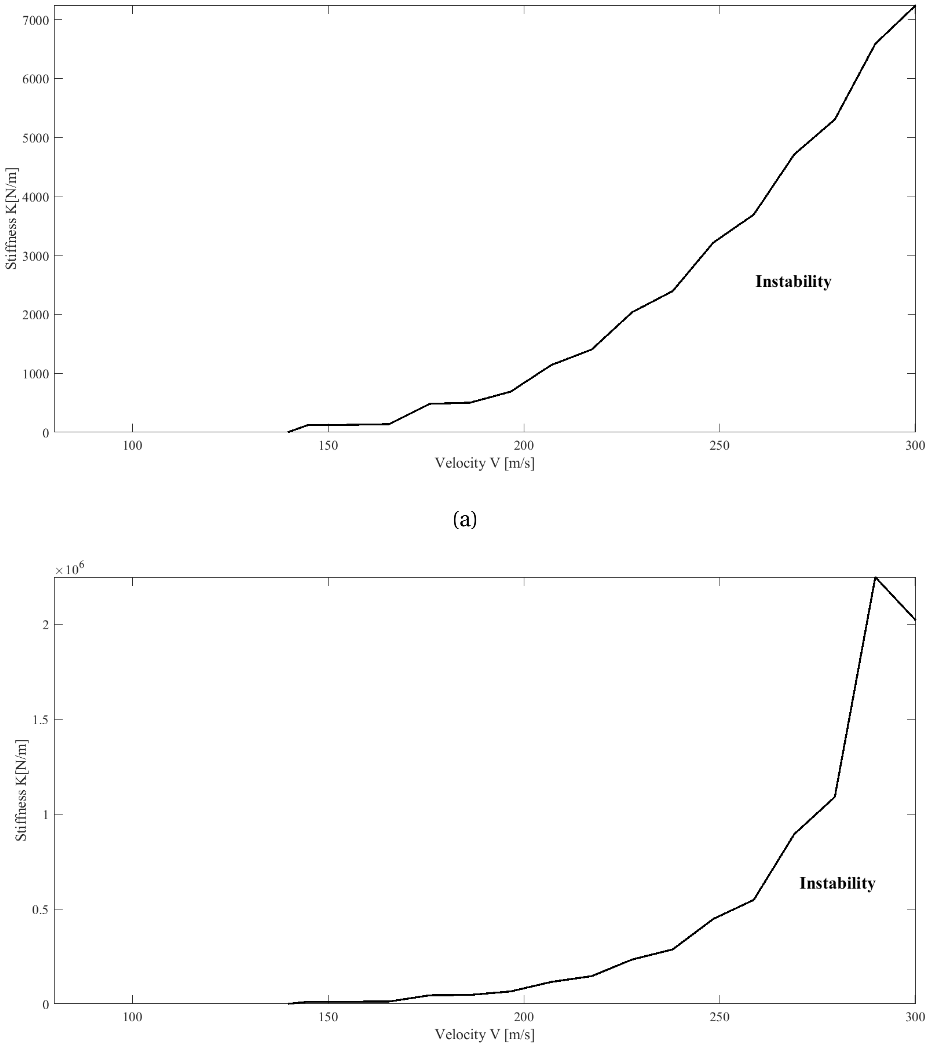

(a)

(b)

Figure 5.7: Instability region for a magnetically levitated uniformly moving (a) competition pod on a small-scale track and (b) full-scale Hyperloop pod on a full-scale track respectively, based on the parameters of the high-strength concrete tube (table 5.3), while the parameters of the half-plane are taken from table 4.1.

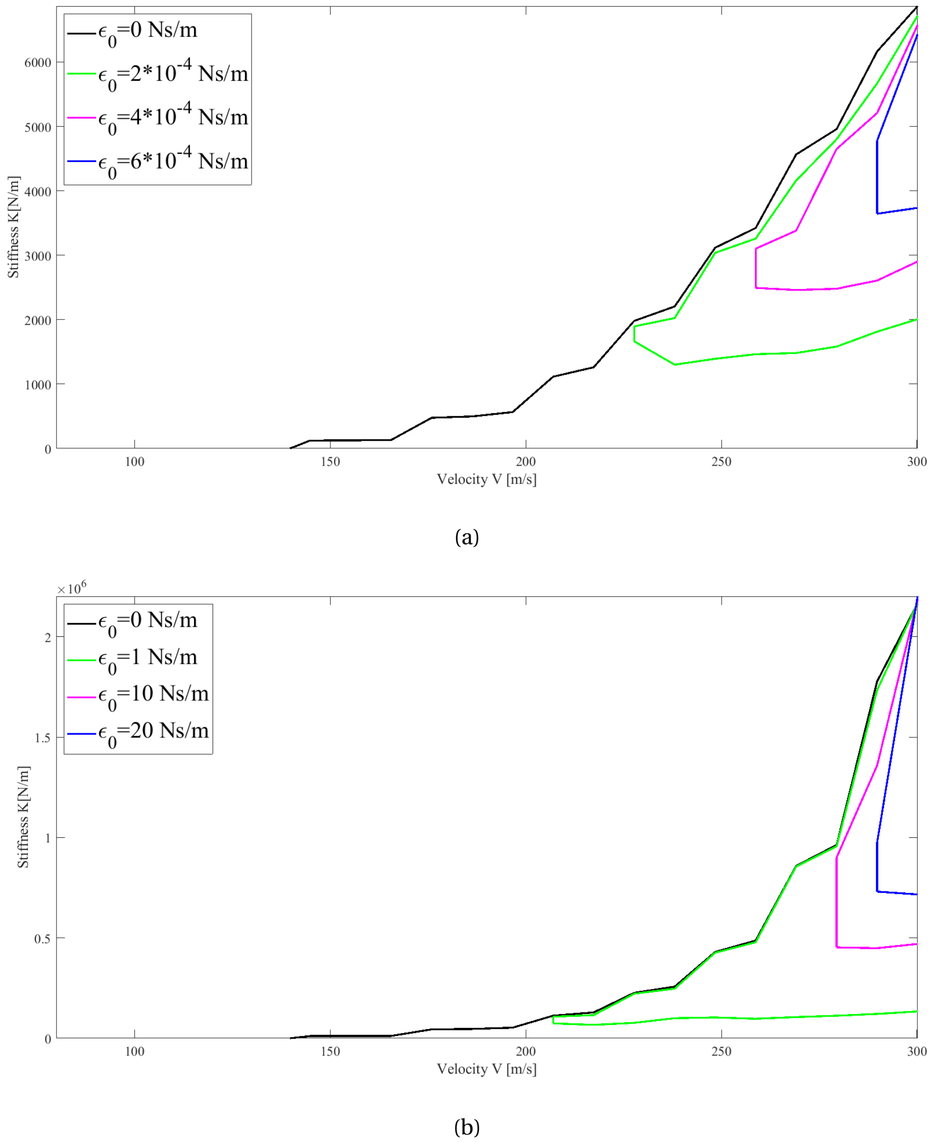

(a)

(b)

Figure 5.8: Effect of the oscillator's viscous damping on the instability region for a magnetically levitated uniformly moving (a) competition pod on a small-scale track and (b) full-scale Hyperloop pod on a full-scale track respectively, based on the parameters of the normal strength concrete tube (table 4.4), while the parameters of the half-plane are taken from table 4.1.

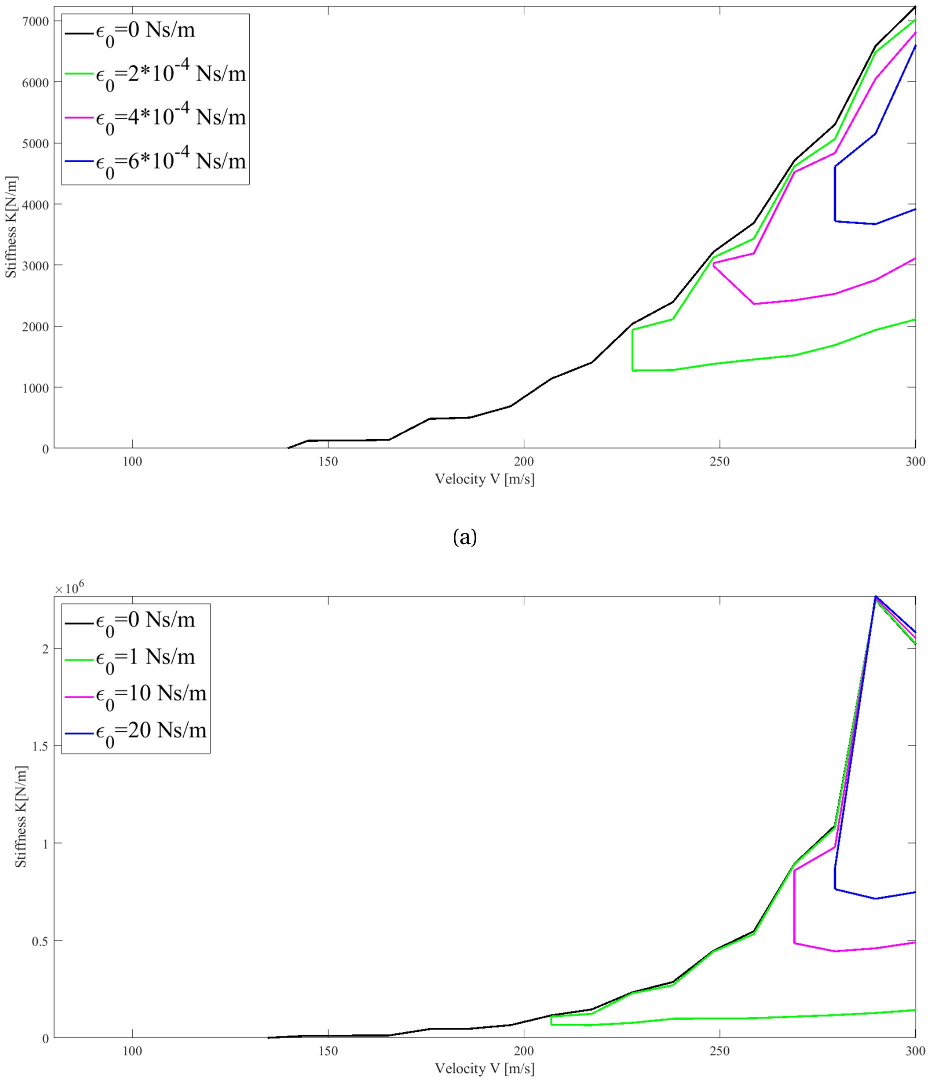

(a)

(b)

Figure 5.9: Effect of the oscillator's viscous damping on the instability region for a magnetically levitated uniformly moving (a) competition pod on a small-scale track and (b) full-scale Hyperloop pod on a full-scale track respectively, based on the parameters of the high-strength concrete tube (table 5.3), while the parameters of the half-plane are taken from table 4.1.

6

CONCLUSIONS AND DISCUSSION

This chapter summarizes the results found in the previous chapters and relates them to the research questions raised in chapter 1. The last part of this chapter gives suggestions for further research and discusses some of the assumptions made in the report.

6.1. FIRST CENTRAL RESEARCH QUESTION

THE first main research question of this thesis is:

How can the motion of a high-speed vehicle moving in a tunnel be modelled in a transparent way taking into account the interaction between soil, tunnel and vehicle? How does the description of the motion change when the magnetic levitation suspension system is introduced?

This question was answered in chapter 3 and chapter 5. More specifically, the third chapter describes the governing equations of motion, boundary and interface conditions for the model where the two-mass moving oscillator remains in direct contact with the beam throughout the motion. The fifth chapter analyzes the changes in the description of the model when the non-contact suspension system is taken into account.

To answer the first central research question in a structured way, the five sub-questions belonging to it are treated below.

(1a) How can the vehicle-tube-soil system be modelled?

The different modelling options are discussed thoroughly in the literature review. Because of the fact that a quantitatively accurate estimation of the instability domain for the vehicle velocity can not be achieved when a one-dimensional model of the railway track is considered, a two-dimensional model of the supporting structure is chosen. A three-dimensional model could have been opted for as well, but neglecting the out-of-plane dimension simplifies the problem to some extent. The final model is that of a two-mass oscillator moving along an Euler-Bernoulli beam embedded in a visco-elastic half-plane. The material damping in the half-plane is accounted for because it makes the model more realistic.
Introducing the magnetic levitation suspension system raises the question as to how this can be included in the model in the most realistic way. The literature review provides an answer to this problem. The non-contact suspension system is added as a nonlinear spring for which the stiffness depends on

both the velocity of the vehicle and the gap between the pod and the beam. For the analysis, this spring stiffness is linearized by applying a simple first order Taylor approximation. For the instability analysis, both a small-scale and full-scale model of pod and track are considered.

The next two sub-questions are dealt with together.

(1b) What are the governing equations of motion for the soil, for the tube and for the uniformly moving vehicle in the tube and how do they relate?

(1c) Which boundary and interface conditions have to be accounted for?

To formulate the governing equations of motion, boundary and interface conditions, a few assumptions are made. The half-plane is considered to be homogeneous and isotropic and its surface is not loaded and traction free. The beam does not move horizontally. For the model without magnetic levitation suspension system, the vertical vibrations of beam and half-plane are assumed to be equal at the interface.

Following the procedure described in the literature review, the equations of motion for the soil, beam and vehicle are determined. Employing Helmholtz decomposition, two uncoupled equations describing the soil motion are obtained. The Dirac-delta function enters the right-hand side of the beam equation to account for the vehicle-structure interaction in the loading point. As the stability of the oscillator is studied in this report, a reference system which is fixed to the moving vehicle is introduced. Then, the Laplace transform with respect to time and the Fourier transform with respect to the horizontal spatial coordinate are applied on all equations to facilitate the stability analysis. Eventually, application of this procedure delivers equations of motion, boundary and interface conditions in the Laplace-wavenumber domain. When the general solution to the soil equation is substituted into the boundary and interface conditions and the result is combined with the equations of motion for the beam and the oscillator, a reduced one-dimensional model is obtained. This model is equivalent to that of a two-mass oscillator moving along a beam on a visco-elastic foundation for which the stiffness $\chi_{\mathrm{eq}}^{\mathrm{h\text{-}p}}$ is complex-valued.

(1d) Based on the answers to sub-questions 1a) to 1c), how can the soil-beam system be characterized and based on this characterization, how are the vehicle vibration described?

To find the characteristic equation for the vertical vibrations of the oscillator the inverse Fourier transform is applied to reduce the one-dimensional model to a lumped mass-spring-dashpot model. In the equation describing the motion of the latter model, the reaction of the beam-half-plane system in the point of contact with the oscillator is reflected by the frequency- and velocity-dependent complex stiffness $\chi_{\mathrm{eq}}^{\mathrm{beam}}$. Finally, the characteristic equation is obtained by combining the equation of motion for the lumped model with that for the upper oscillator mass.

(1e) How does the introduction of a non-contact suspension system influence the answers to sub-questions 1a) to 1d)?

For the model including the non-contact suspension system the assumption that the vertical vibrations of beam and half-plane are equal at the interface, is not valid anymore as the magnetic spring now connects the vehicle to the beam. From the literature review, an expression for the levitation force of the magnetic suspension system is obtained. The latter force is first linearized to allow for the application of the Fourier and Laplace transform. Subsequently, the levitation force is introduced in the lumped model by means of a magnetic spring. After linearization, the magnetic spring stiffness only depends on the uniform vehicle velocity V and the properties of the magnetic field. From the equations of motion describing the behaviour of the lumped mass model, the characteristic equation is derived. As the introduction of the electrodynamic suspension system does not alter the beam-half-plane system, the equivalent dynamic stiffness of the beam embedded in the half-plane, $\chi_{\text{eq}}^{\text{beam}}$, remains unchanged. In the lumped model however, the magnetic spring is put in series with $\chi_{\text{eq}}^{\text{beam}}$. Therefore, the characteristic equation now contains the equivalent stiffness of both springs in series.

6.2. SECOND CENTRAL RESEARCH QUESTION

THE second main research question raised in the first chapter of this thesis is:

What is the influence of the different model parameters on the vehicle vibrations and how do modifications in the vehicle suspension affect the instability of the pod vibrations?

The answers to this question are formulated in chapter 4 for the model where the vehicle is in constant contact with the beam and in chapter 5 for the magnetically levitated vehicle. The latter chapter studies the instability of vibrations of both the Hyperloop small-scale vehicle as designed by Delft Hyperloop and the full-scale pod, for which the parameters are derived from the literature.

The sub-questions belonging to this central research question are treated one by one.

(2a) Up to which velocity are the vibrations of the vehicle unconditionally stable for a given set of parameters?

The answer to this sub-question has been formulated for one set of parameters, which are used as the base parameters throughout this research. The system in unconditionally stable when the imaginary part of the equivalent dynamic stiffness, $\chi_{\text{eq}}^{\text{beam}}$, is positive over the complete frequency range. A negative imaginary part of $\chi_{\text{eq}}^{\text{beam}}$ implies a negative radiation damping that is related to the radiation of anomalous Doppler waves. In that case, oscillator vibrations *may* become unstable.

For velocities below the Rayleigh wave speed, the vertical oscillator vibrations are unconditionally stable. For a uniform vehicle velocity between the Rayleigh and shear wave speed, $\Im(\chi_{\text{eq}}^{\text{beam}}) < 0$ for the very low frequencies, and thus the system *may* become unstable. When the velocity is further increased, the imaginary part of the equivalent dynamic stiffness is always negative over a certain frequency band up to a velocity of approximately $2.2c_T = 228$ m/s. From this velocity on, due to the effect of the material damping in the half-plane, the 'negative damping' disappears and the system is unconditionally stable again.

The study of the effect of the material damping on the equivalent dynamic stiffness shows that an increasing material damping raises the velocity at which the imaginary part of the equivalent stiffness first becomes negative. Moreover, up to a velocity of approximately 166 m/s, the frequency band where this imaginary part is negative, shrinks and the absolute value of $\Im(\chi_{\text{eq}}^{\text{beam}})$ decreases with increasing material damping. However, when the velocity rises further, a higher magnitude of the material damping increases the absolute value of the imaginary part of the equivalent stiffness in the frequency band where the latter is negative. Besides, the 'negative damping' will only disappear at higher vehicle velocities when the viscosity of the half-plane increases. This is a remarkable result, as apparently the material damping destabilizes the system for the higher velocities.

Sub-questions (2b) and (2c) are considered together. They refer to the model where the magnetic levitation suspension system is not included.

(2b) When examining the moving vehicle vibrations, from which velocity does instability occur?

(2c) How does changing the model parameters influence the outcome of sub-question 2b) ?

In first instance, the instability of a single mass moving along the beam is investigated for the base parameters of the beam and the half-plane to establish the total mass magnitude from which vibrations of that single mass become unstable. The instability domain is derived from the D-decomposition of the complex m_1-plane. From this analysis it can be concluded that instability of vibrations only occurs for mass magnitudes in the order of 10^6 kg or higher, which is considerably higher than the total mass of the observed two-mass oscillator.
Based on the results for the uniformly moving single mass and the D-decomposition of the complex K-plane, the instability domain for the two-mass oscillator's vertical vibrations is derived, taking into account the base parameters. The zone of unstable vibrations is bounded from the left, as well as from the right. It starts at a velocity slightly below 100 m/s and extends to $V \approx 240$ m/s. The stiffness below which unstable vibrations can occur over the velocity range $V = 0 \rightarrow 300$ m/s is found as $K^* = 5.2 \cdot 10^6$ N/m.
The effect of the model parameters on the instability zone is then analyzed. The following effects have been found:

- increase of the material damping in the half-plane causes the instability domain to shrink along the stiffness axis and increases the critical velocity, though it also expands the instability domain towards higher vehicle velocities,
- increase of the Young's modulus of the half-plane leads to a shrinkage of the instability domain along the stiffness axis, but at the same time, this zone expands to the right along the velocity axis,
- increase of the depth of the tube causes the magnitude of the critical stiffness to increase. However, no unambiguous result has been found concerning the effect on the instability domain's size along the velocity axis,
- increase in the flexural rigidity of the beam leads to shrinkage of the instability domain along the stiffness axis and increases the critical velocity at which instability first occurs, but it also causes the right boundary to shift towards the higher vehicle velocities,
- increase of the mass per unit length shifts the instability domain towards lower velocities and expands the zone along the stiffness axis,
- increase of the upper mass magnitude destabilizes the system, though it does not influence the bounding velocities of the instability domain,
- increase of the viscous damping in the oscillator stabilizes the system considerably, as it leads to a shrinkage and a change in size of the instability domain.

The material damping and the viscous damping in the oscillator can cause the instability domain to disappear completely, thus making the system unconditionally stable. The oscillator's viscosity has the most important stabilizing effect as it causes the instability domain to shrink rapidly and disappear completely for a rather limited value of the oscillator's viscous damping, namely 75 Ns/m for the base parameters of the model.
For both the Hyperloop small-scale pod and full-scale pod moving along the embedded beam, the instability domain disappears completely. This is mainly due to the viscous damping in the observed vehicles, which is considerably larger than the viscosity for which the instability domain first disappears.

(2d) What is the effect of a change in the vehicle suspension on the instability of the vehicle vibrations?

When the magnetic levitation suspension system is accounted for, the instability domain for the uniformly moving single mass shifts down and the critical mass magnitude above which the vibrations of the single mass become unstable decreases steeply. The magnitude of the downward shift depends mainly on the parameters of the magnetic field as they determine the stiffness of the magnetic spring. Thus, the design of the magnetic levitation suspension system has a considerable influence on the system's stability. Moreover, there is a danger in increasing the total mass of the vehicle as it may cause vibrations to become unstable at certain velocities, even for very high K.
For both the small- and full-scale model of pod and track the total mass magnitude lies below the lowest critical mass magnitude that is derived for a uniformly moving single mass in both a normal strength and high-strength tunnel. Yet, especially for the full-scale pod, the total mass and the critical mass are not that far apart for the highest vehicle velocities. Hence, the mass of the Hyperloop pods should be established taking into account the equivalent stiffness of both the magnetic spring and the beam-half-plane structure which work in series.
When considering the total pod mass magnitudes as upper limits, it is found that, in the absence of viscous damping in the vehicle, the critical velocity for a pod moving in a normal strength or high-strength tunnel is more or less identical, namely $V_{\text{crit}} \approx 140$ m/s. Considered over the full velocity range though, the model with the high-strength tunnel has a slightly higher maximum magnitude of the critical stiffness. Furthermore, when viscous damping is introduced in the vehicle, the instability domain shrinks rapidly for all considered models. For both the small-scale pod and the full-scale pod, the instability domain has disappeared completely at a viscosity which is considerably lower than the assumed viscosity for both vehicle models. This is the case for the normal strength as well as for the high-strength concrete tunnel. Based on the stability analysis, the conclusion can be drawn that instability should not be considered as a threat for the magnetically levitated small-scale pod nor for the full-scale pod. Yet, especially for the full-scale pod, the properties of the magnetic levitation system and of the vehicle itself should be determined with care because of the steep decrease in the critical value of the uniformly moving single mass magnitude.

6.3. DISCUSSION AND RECOMMENDATIONS

In this report the beam embedded in the half-plane is considered as a two-dimensional model for the underground tunnel. This way, the properties of the soil and the reaction of the beam-half-plane system in the point of contact with the moving vehicle are accounted for. Yet, as the beam height and the out-of-plane dimension are neglected, a two-dimensional model also implies that the beam is actually an infinite plate rather than a real tunnel. This means that the analyses in which the stiffness of a realistic tunnel is accounted for, are not completely correct. To incorporate a realistic tunnel in a two-dimensional model, its stiffness should have been reduced. Furthermore, it would be interesting to compare the obtained results with those from a three-dimensional model in which the out-of-plane dimension is taken into account.

The two-mass oscillator vehicle model is a simplistic one. A more sophisticated two-oscillator model would enable the study of the effect of the distance between the supports of the pod on the instability of its vertical vibrations. An even more extensive model of a rigid bar placed on two supports that connect the bar and the beam would add an extra degree of freedom to the model. The latter vehicle model makes the instability analysis more complete as the moment of inertia of the Hyperloop vehicle body would be accounted for.

A few assumptions should be discussed as well. First, the half-plane is considered to be homogeneous. This is a significant simplification given that in reality, the soil is layered with each layer having different properties. Moreover, localized variations throughout a soil layer can occur. Veritchev has shown that taking into account periodic inhomogeneity of the foundation affects the instability domain [10]. Often, limited information is available about the properties of the soil and even if the soil

could be modelled realistically, analytical methods to analyze the instability of vibrations lack the flexibility to investigate such complex scenarios. Semi-analytical methods and discrete numerical methods have proven to be more suited for modelling the complex soil structure [39]. Application of such methods could provide more realistic conclusions with respect to the instability of vibrations of the Hyperloop pod moving in an underground tunnel.
Secondly, the beam is assumed not to move horizontally. It would be interesting to investigate how horizontal movement of the beam would influence the results.
Finally, the Euler-Bernoulli beam has been used as a model for the tunnel. As mentioned in [13], this beam model is only valid for relatively small frequencies. It is shown in this report that instability only occurs for the lower angular frequencies , so the Euler-Bernoulli beam can be applied for the stability analysis.

It is clear that the stability analysis for the model including the electrodynamic suspension system depends strongly on the definition of the magnetic spring stiffness. The definition in this report has been based on the levitation force found for the Inductrack system. Moreover, the properties of the permanent magnets and the track have been derived from literature. Both the definition of the magnetic spring stiffness and of the parameters should be reevaluated when constructing a real Hyperloop track consisting of coils. Moreover, for a full-scale vehicle, very limited information about the configuration of the permanent magnets is available. As a different configuration of the Halbach arrays on the Hyperloop pods may influence the system's stability, the results in this report should be reassessed when constructing such a pod.

REFERENCES

[1] A. C. W. M. Vrouwenvelder, *Random vibrations,* Lecture notes CIE5145, Delft University of Technology.

[2] J. W. Welleman, *Slender structures - load carrying principles, part 1: Basic cases,* (2017), lecture notes CIE4190, Delft University of Technology.

[3] A. V. Metrikine, *Dynamics, slender structures and an introduction to continuum mechanics,* (2006), lecture notes CT4145, Delft University of Technology.

[4] Maloney, *Waves and vibrations,* Lecture notes, Massachusetts Institute of Technology.

[5] K. van Dalen, *Soil dynamics, part b: Body waves in an elastic continuum and rayleigh waves at the free surface,* (2015), lecture notes CIE5340, Delft University of Technology.

[6] A. V. Metrikine and A. C. W. M. Vrouwenvelder, *"dynamics of structures, part 2: Wave dynamics",* (2006), lecture notes CT4140, Delft University of Technology.

[7] A. Gharahi, M. Rahimian, M. Eskandari-Ghadi, and R. Pak, *Dynamic interaction of a pile with a transversely isotropic elastic half-space under transverse excitations,* "International Journal of Solids and Structures" **51**, 4082 (2014).

[8] A. V. Metrikine and A. C. W. M. Vrouwenvelder, *Surface ground vibration due to a moving train in a tunnel: Two-dimensional model,* "Journal of Sound and Vibration" **234**, 43 (2000).

[9] A. Wolfert, *Wave-effects in One-Dimensional Elastic Systems Interacting with Moving Objects*, Thesis, Delft University of Technology (1999).

[10] S. N. Veritchev, *Instability of a vehicle moving on an elastic structure*, Ph.D. thesis, TU Delft, Delft University of Technology (2002).

[11] A. Wolfert, H. Dieterman, and A. Metrikine, *Stability of vibrations of two oscillators moving uniformly along a beam on a viscoelastic foundation,* Journal of Sound and Vibration **211**, 829 (1998).

[12] A. Metrikine, S. Verichev, and J. Blaauwendraad, *Stability of a two-mass oscillator moving on a beam supported by a visco-elastic half-space,* "International Journal of Solids and Structures" **42**, 1187 (2005).

[13] A. V. Metrikine and K. Popp, *Instability of vibrations of an oscillator moving along a beam on an elastic half-space,* "European Journal of Mechanics - A/Solids" **18**, 331 (1999).

[14] N. H. Kim and L. Ge, *Modeling of electrodynamic suspension systems,* in *ASME 2006 International Design Engineering Technical Conferences and Computers and Information in Engineering Conference* (American Society of Mechanical Engineers, 2006) pp. 667–676.

[15] *Final Design Package*, Delft Hyperloop team, Delft (2018).

[16] J. Blauwendraad, *Dynamica van systemen,* (2006), collegedictaat CTB2300, Delft University of Technology.

[17] A. Schafer and D. G. Victor, *The future mobility of the world population,* "Transportation Research Part a-Policy and Practice" **34**, 171 (2000).

[18] *Conceptual feasibility study of the Hyperloop vehicle for next-generation transport* (NASA Glenn Research Center; Cleveland, OH United States, 2017).

[19] S. Pfoser, T. Berger, G. Hauger, C. Berkowitsch, R. Schodl, S. Eitler, K. Markvica, B. Hu, J. Zajicek, and M. Prandtstetter, *Integrating high-performance transport modes into synchromodal transport networks,* in *Dynamics in Logistics*, edited by M. Freitag, H. Kotzab, and J. Pannek (Springer International Publishing, Cham, 2018) pp. 109–115.

[20] A. V. Metrikine and H. A. Dieterman, *Instability of vibrations of a mass moving uniformly along an axially compressed beam on a viscoelastic foundation,* "Journal of Sound and Vibration" **201**, 567 (1997).

[21] H. A. Dieterman and A. Metrikine, *The equivalent stiffness of a half-space interacting with a beam. critical velocities of a moving load along the beam,* "European Journal of Mechanics a-Solids" **15**, 67 (1996).

[22] R. Gans, *Mechanical Systems: A Unified Approach to Vibrations and Controls*, SpringerLink : Bücher (Springer International Publishing, 2014).

[23] J. M. J. Spijkers, A. C. W. M. Vrouwenvelder, and E. Klaver, *Dynamics of structures, part 1: Vibrations of structures,* (2006), lecture notes CT4140, Delft University of Technology.

[24] S. H. Schot, *Eighty years of sommerfeld's radiation condition,* "Historia Mathematica" **19**, 385 (1992).

[25] S. van Dijk, *The dynamic behavior of floors in high-rise buildings and their contribution to damping - an analytical model*, Master's thesis, Delft University of Technology, Delft (2015).

[26] A. Salih, *Second-order wave equation,* (2016), lecture notes, Indian Institute of Space Science and Technology.

[27] S. Mahajan, *Art of approximation,* (2008), lecture notes, Massachusetts Institute of Technology.

[28] M. Dehestani, A. Vafai, M. Mofid, and F. Szidarovszky, *Computation of the stresses in a moving reference system in a half-space due to a traversing time-varying concentrated load,* "Computers & Mathematics with Applications" **65**, 1849 (2013).

[29] H. A. Dieterman and A. Metrikine, *Critical velocities of a harmonic load moving uniformly along an elastic layer,* "Journal of Applied Mechanics" **64**, 596 (1997).

[30] T. Mazilu and M. Dumitriu, *On the anomalous doppler effect,* Romanian Journal of Acoustics and Vibration **8**, 115 (2011).

[31] A. Metrikin, *Unstable lateral oscillations of an object moving uniformly along an elastic guide as a result of an anomalous doppler effect,* "Acoustical Physics" **40**, 85 (1994).

[32] A. V. Metrikine and S. N. Verichev, *Instability of vibrations of a moving two-mass oscillator on a flexibly supported timoshenko beam,* "Archive of Applied Mechanics" **71**, 613 (2001).

[33] G. Denisov, E. Kugusheva, and V. Novikov, *On the problem of the stability of one-dimensional unbounded elastic systems,* "Journal of Applied Mathematics and Mechanics" **49**, 533 (1985).

[34] S. Verichev and A. Metrikine, *Instability of a bogie moving on a flexibly supported timoshenko beam,* Journal of sound and vibration **253**, 653 (2002).

[35] S. N. Verichev and A. V. Metrikine, *Dynamic rigidity of a beam in a moving contact,* Journal of Applied Mechanics and Technical Physics **41**, 1111 (2000).

[36] D. Zheng, F. Au, and Y. Cheung, *Vibration of vehicle on compressed rail on viscoelastic foundation,* Journal of Engineering Mechanics **126**, 1141 (2000).

[37] D. Zheng and S. Fan, *Instability of vibration of a moving-train-and-rail coupling system,* Journal of Sound and vibration **255**, 243 (2002).

[38] S. Verichev and A. Metrikine, *Instability of vibrations of a mass that moves uniformly along a beam on a periodically inhomogeneous foundation,* "Journal of Sound and Vibration" **260**, 901 (2003).

[39] S. Jones, *Ground vibration from underground railways: how simplifying assumptions limit prediction accuracy*, Ph.D. thesis, University of Cambridge (2010).

[40] R. F. Post and D. D. Ryutov, *The inductrack: A simpler approach to magnetic levitation,* IEEE Transactions on Applied Superconductivity **10**, 901 (2000).

[41] J. Gohil and K. Jani, *Electromagnetic and magnetic suspension,* International Journal of Engineering Development and Research (2017).

[42] H. Hoshino, E. Suzuki, T. Yonezu, and K. WATANABE, *Examination of vehicle motion characteristics of a maglev train set using a reduced-scale model experiment apparatus,* Quarterly Report of RTRI **53**, 52 (2012).

[43] T. Murai and H. Hasegawa, *Electromagnetic analysis of inductrack magnetic levitation,* Electrical Engineering in Japan **142**, 67 (2003).

[44] J. Sikkema, *Grid_zeros,* (2018), matlab code.

[45] J. Sikkema, *Newton_raphson,* (2018), matlab code.

[46] J. Sikkema, *Gradient,* (2018), matlab code.

[47] J. Sikkema, *Grid_optimization,* (2018), matlab code.

[48] J. Sikkema, *Gradient_descent,* (2018), matlab code.

[49] J. Sikkema, *Integration_method,* (2018), matlab code.

[50] S. Brueckner, *Crossing,* (2007), matlab code.

A

Appendix A

In the x,z-reference system, the governing equations of motion for the beam loaded by a moving two-mass oscillator and supported by a Winkler foundation with stiffness χ (as shown in fig. A.1 below) are given by [13]

$$m_b \frac{\partial^2 w_b}{\partial t^2} + EI \frac{\partial^4 w_b}{\partial x^4} + \chi w_b = \delta(x - Vt) \Big\{ - \Big[m_1 \frac{\partial^2 w_1}{\partial t^2} + \big(K + \epsilon_0 \frac{\partial}{\partial t}\big)\big(w_1 - w_2\big) \Big] \Big\}, \tag{A.1a}$$

$$m_2 \frac{\partial^2 w_2}{\partial t^2} + \big(K + \epsilon_0 \frac{\partial}{\partial t}\big)\big(w_2 - w_1\big) = P(t). \tag{A.1b}$$

Equation (A.1a) describes the displacement of the beam, while eq. (A.1b) gives the EOM for the upper oscillator mass m_2.

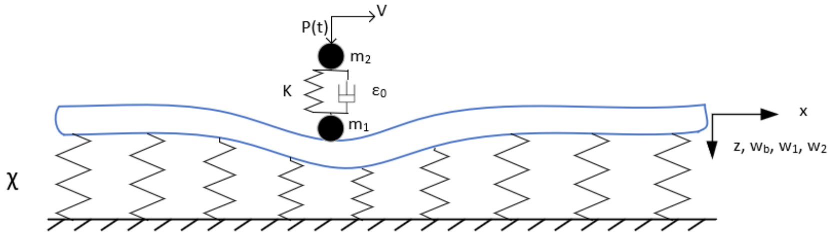

Figure A.1: Beam loaded by moving two-mass oscillator on Winkler foundation

As described in section 2.2.3, a moving reference system is introduced. For a one-dimensional model, the coordinates of this reference system are given by

$$\begin{cases} \xi & = x - Vt, \\ \tau & = t. \end{cases}$$

Equations A.1 can then be rewritten as

$$m_{\mathrm{b}}\Big(\frac{\partial}{\partial\tau}-V\frac{\partial}{\partial\xi}\Big)^2 w_{\mathrm{b}}+EI\frac{\partial^4 w_{\mathrm{b}}}{\partial\xi^4}+\chi w_{\mathrm{b}}=\delta(\xi)\Big\{-\Big[m_1\frac{\partial^2 w_1}{\partial\tau^2}+\Big(K+\epsilon_0\frac{\partial}{\partial\tau}\Big)\big(w_1-w_2\big)\Big]\Big\}, \tag{A.2a}$$

$$m_2\frac{\partial^2 w_2}{\partial\tau^2}+\Big(K+\epsilon_0\frac{\partial}{\partial\tau}\Big)\big(w_2-w_1\big)=P(\tau). \tag{A.2b}$$

In a last step the transforms defined in eqs. (3.18) to (3.20) are applied to eq. (A.2):

$$v_b\Big[m_{\mathrm{b}}\big(s-ikV\big)^2+EIk^4+\chi\Big]=-\Big[m_1 s^2 v_1+\big(K+\epsilon_0 s\big)\big(v_1-v_2\big)\Big], \tag{A.3a}$$

$$m_2 s^2 v_2+\big(K+\epsilon_0 s\big)\big(v_2-v_1\big)=p(s). \tag{A.3b}$$

Equation (A.3a) gives then eq. (3.30).

B

Appendix B

The expressions for the terms a_{ij} and F_i in the system of equations given by eq. (3.38) are obtained from eqs. (3.34) to (3.36):

$$a_{ij} = \begin{bmatrix} \frac{\mu_{sk}(2c_T^2-c_L^2)k^2+R_L^2c_L^2}{c_T^2} & \frac{\mu_{sk}(2c_T^2-c_L^2)k^2+R_L^2c_L^2}{c_T^2}\exp(-hR_L) & -2\mathrm{i}\mu_{sk}R_Tk & 2\mathrm{i}\mu_{sk}R_Tk\exp(-hR_T) & 0 & 0 \\ -2\mathrm{i}\mu_{sk}R_Lk & 2\mathrm{i}\mu_{sk}R_Lk\exp(-hR_L) & -\mu_{sk}(R_T^2+k^2) & -\mu_{sk}(R_T^2+k^2)\exp(-hR_T) & 0 & 0 \\ \mathrm{i}k\exp(-hR_L) & \mathrm{i}k & R_T\exp(-hR_T) & -R_T & 0 & 0 \\ \left(-R_L+\frac{a\mu_{sk}\left((2c_T^2-c_L^2)k^2+R_L^2c_L^2\right)}{c_T^2D(k,s)}\right)\exp(-hR_L) & R_L+\frac{a\mu_{sk}\left((2c_T^2-c_L^2)k^2+R_L^2c_L^2\right)}{c_T^2D(k,s)} & \mathrm{i}k\left(1-\frac{2a\mu_{sk}R_T}{D(k,s)}\right)\exp(-hR_T) & \mathrm{i}k\left(1+\frac{2a\mu_{sk}R_T}{D(k,s)}\right) \quad , & -\frac{a\mu_{sk}\left((2c_T^2-c_L^2)k^2+R_L^2c_L^2\right)}{c_T^2D(k,s)} & \frac{2\mathrm{i}a\mu_{sk}R_Tk}{D(k,s)} \\ 0 & 0 & 0 & 0 & \mathrm{i}k & R_T \\ \frac{a\mu_{sk}\left((2c_T^2-c_L^2)k^2+R_L^2c_L^2\right)}{c_T^2D(k,s)}\exp(-hR_L) & \frac{a\mu_{sk}\left((2c_T^2-c_L^2)k^2+R_L^2c_L^2\right)}{c_T^2D(k,s)} & -\frac{2\mathrm{i}a\mu_{sk}R_Tk}{D(k,s)}\exp(-hR_T) & \frac{2\mathrm{i}a\mu_{sk}R_Tk}{D(k,s)} & -R_L-\frac{a\mu_{sk}\left((2c_T^2-c_L^2)k^2+R_L^2c_L^2\right)}{c_T^2D(k,s)} & \mathrm{i}k\left(1+\frac{2a\mu_{sk}R_T}{D(k,s)}\right) \end{bmatrix}$$

$$F_i = \begin{bmatrix} 0 & 0 & 0 & -\frac{m_1s^2v_1+(K+\epsilon_0s)(v_1-v_2)}{D(k,s)} & 0 & -\frac{m_1s^2v_1+(K+\epsilon_0s)(v_1-v_2)}{D(k,s)} \end{bmatrix}^T \quad ,$$

where, according to eqs. (3.25), (3.29) and (3.33),

$$\mu_{sk} = \mu + \mu^* \left(s - \mathrm{i}kV\right),$$
$$D(k,s) = m_b\left(s - \mathrm{i}kV\right)^2 + EIk^4,$$
$$R_L = \sqrt{k^2 + \frac{\left(s-\mathrm{i}kV\right)^2}{c_L^2 + \frac{\lambda^*+2\mu^*}{\rho}\left(s-\mathrm{i}kV\right)}}, \qquad R_T = \sqrt{k^2 + \frac{\left(s-\mathrm{i}kV\right)^2}{c_T^2 + \frac{\mu^*}{\rho}\left(s-\mathrm{i}kV\right)}}$$

Using Maple 2017 Release 3, the unknowns in eqs. (3.31) and (3.32) are determined. The value of $A1 \rightarrow A6$ and the Maple code used to find these constants is included below.

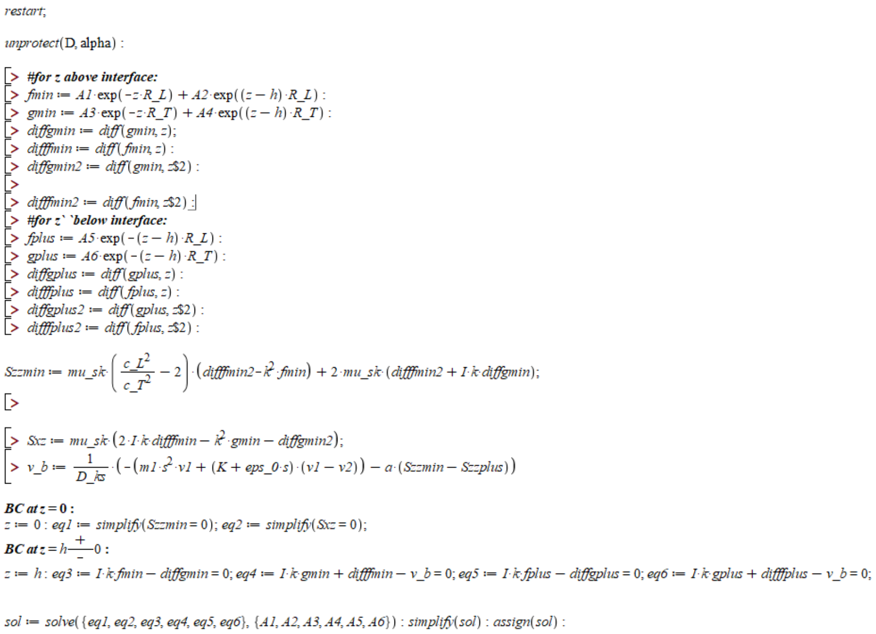

```
restart;

unprotect(D, alpha) :

[> #for z above interface:
[> fmin := A1·exp(−z·R_L) + A2·exp((z − h)·R_L) :
[> gmin := A3·exp(−z·R_T) + A4·exp((z − h)·R_T) :
[> diffgmin := diff(gmin, z);
[> difffmin := diff(fmin, z) :
[> diffgmin2 := diff(gmin, z$2) :
[>
[> difffmin2 := diff(fmin, z$2) :
[> #for z` `below interface:
[> fplus := A5·exp(−(z − h)·R_L) :
[> gplus := A6·exp(−(z − h)·R_T) :
[> diffgplus := diff(gplus, z) :
[> difffplus := diff(fplus, z) :
[> diffgplus2 := diff(gplus, z$2) :
[> difffplus2 := diff(fplus, z$2) :

Szzmin := mu_sk·(c_L^2/c_T^2 − 2)·(difffmin2−k^2·fmin) + 2·mu_sk·(difffmin2 + I·k·diffgmin);
[>

[> Sxz := mu_sk·(2·I·k·difffmin − k^2·gmin − diffgmin2);
[> v_b := 1/D_ks·(−(m1·s^2·v1 + (K + eps_0·s)·(v1 − v2)) − a·(Szzmin − Szzplus))

BC at z = 0 :
z := 0 : eq1 := simplify(Szzmin = 0); eq2 := simplify(Sxz = 0);
BC at z = h+/-0 :
z := h : eq3 := I·k·fmin − diffgmin = 0; eq4 := I·k·gmin + difffmin − v_b = 0; eq5 := I·k·fplus − diffgplus = 0; eq6 := I·k·gplus + difffplus − v_b = 0;

sol := solve({eq1, eq2, eq3, eq4, eq5, eq6}, {A1, A2, A3, A4, A5, A6}) : simplify(sol) : assign(sol) :
```

Figure B.1: Maple code to find unknown constants $A1 \rightarrow A6$.

- $$\boxed{A_1 = \frac{N_1}{D^-},} \tag{B.1}$$

  where

  $$\begin{aligned} N_1 = v_b R_T \Big\{ & \left[\alpha k^4 + \left(\alpha R_T^2 + \gamma - \beta\right)k^2 - \beta R_T^2\right] \exp\left(-h(R_L + 2R_T)\right) \\ & + \left[\alpha k^4 + \left(\alpha R_T^2 - \gamma - \beta\right)k^2 - \beta R_T^2\right] \exp\left(-hR_L\right) \\ & + \left[4k^2 c_T^2 \left(R_T^2 + k^2\right)\right] \exp\left(-hR_T\right) \Big\} \end{aligned} \tag{B.2}$$

  and

$$
\begin{aligned}
D^{-} = &\big(-R_L R_T + k^2\big)\Big[\alpha k^4 + \big(\alpha R_T^2 + \gamma - \beta\big)k^2 - \beta R_T^2\Big] \exp\left(-2h(R_L + R_T)\right) \\
&- \big(R_L R_T + k^2\big)\Big[\alpha k^4 + \big(\alpha R_T^2 - \gamma - \beta\big)k^2 - \beta R_T^2\Big] \exp\left(-2hR_T\right) \\
&- \big(R_L R_T + k^2\big)\Big[\alpha k^4 + \big(\alpha R_T^2 - \gamma - \beta\big)k^2 - \beta R_T^2\Big] \exp\left(-2hR_L\right) \\
&+ \big(-R_L R_T + k^2\big)\Big[\alpha k^4 + \big(\alpha R_T^2 + \gamma - \beta\big)k^2 - \beta R_T^2\Big] \\
&+ 8R_L R_T k^2\Big[\big(c_L^2 - 3c_T^2\big)k^2 - \beta - R_T^2 c_T^2\Big] \exp\left(-h(R_L + R_T\right).
\end{aligned}
\tag{B.3}
$$

- $$\boxed{A_2 = \frac{N_2}{D^{-}},} \tag{B.4}$$

where

$$
\begin{aligned}
N_2 = -v_b R_T\Big\{&\Big[\alpha k^4 + \big(\alpha R_T^2 - \gamma - \beta\big)k^2 - \beta R_T^2\Big] \exp\left(-2hR_T\right) \\
&+ \Big[\alpha k^4 + \big(\alpha R_T^2 + \gamma - \beta\big)k^2 - \beta R_T^2\Big] \\
&+ 4k^2 c_T^2\big(R_T^2 + k^2\big) \exp\left(-h(R_L + R_T)\right)\Big\},
\end{aligned}
\tag{B.5}
$$

- $$\boxed{A_3 = \frac{N_3}{D^{-}},} \tag{B.6}$$

where

$$
\begin{aligned}
N3 = -\mathrm{i}v_b k\Big\{&4R_T R_L\Big[\alpha k^2 - \beta\Big] \exp\left(-hR_L\right) \\
&+ \Big[\alpha k^4 + \big(\alpha R_T^2 + \gamma - \beta\big)k^2 - \beta R_T^2\Big] \exp\left(-h(2R_L + R_T)\right) \\
&+ \Big[-\alpha k^4 + \big(-\alpha R_T^2 + \gamma + \beta\big)k^2 + \beta R_T^2\Big] \exp\left(-hR_T\right)\Big\}.
\end{aligned}
\tag{B.7}
$$

- $$\boxed{A_4 = \frac{N_4}{D^{-}},} \tag{B.8}$$

where

$$
\begin{aligned}
N_4 = \mathrm{i}v_b k\Big\{&-4R_T R_L\Big[\alpha k^2 - \beta\Big] \exp\left(-h(R_L + R_T)\right) \\
&+ \Big[\alpha k^4 + \big(\alpha R_T^2 - \gamma - \beta\big)k^2 - \beta R_T^2\Big] \exp\left(-2hR_L\right) \\
&+ \Big[-\alpha k^4 + \big(-\alpha R_T^2 - \gamma + \beta\big)k^2 + \beta R_T^2\Big]\Big\}.
\end{aligned}
\tag{B.9}
$$

- $$\boxed{A_5 = \frac{N_5}{D^{+}},} \tag{B.10}$$

where

$$N_5 = -R_T v_b \tag{B.11}$$

and

$$D^{+} = R_L R_T - k^2. \tag{B.12}$$

- $$\boxed{A_6 = \frac{N_6}{D^{+}},} \tag{B.13}$$

  where

  $$N_6 = \mathrm{i} k v_b. \tag{B.14}$$

In the equations above following notations are introduced:

- $$\alpha = c_L^2 - 2c_T^2, \tag{B.15}$$
- $$\beta = R_L^2 c_L^2, \tag{B.16}$$
- $$\gamma = 4 R_L R_T c_T^2. \tag{B.17}$$

C

APPENDIX C

C.1. MATLAB CODE FOR FINDING THE DISPERSION CURVES

BELOW the Matlab code employed for finding the dispersion curves is depicted. The real solution to eq. (4.1) is found using Newton Raphson, while the minima of $|\Delta(k,\omega)|$ are determined using grid optimization over the $k-\omega$-field.

- Define the system parameters in the script named "modeldata":

```
% define the value of the parameters
%for the half-plane
nu           = 0.3;
mu           = 2.1*10^7;
rho          = 1960;
lambda_star=mu_star = 0.0*mu; %material damping in the half-plane set to zero
%for finding the dispersion curve
cT = 103.5;
cL = 193.6;
cR = 95.9;
%for the beam
EI = 1.3e8;
mb = 7500;
a  = 1.5;
h  = 12;
```

- Define the determinant $\Delta(k,\omega)$ in the function "determinant":

```
function [disprel]=determinant(k,omega)
    % If real part of qL or real part of qT is negative change qL,qT to -qL,-qT
    qLHat = qL(k, omega);
    if real(qLHat) < 0
        qLHat = -qLHat;
    end
    qTHat = qT(k, omega);
    if real(qTHat) < 0
        qTHat = -qTHat;
    end
    fmin=A1*exp(-z*qL)+A2*exp(z*qL);
    gmin=A3*exp(-z*qT)+A4*exp(z*qT);
```

```
        fplus=A5*exp(-z*qL)+A6*exp(z*qL);
        gplus=A7*exp(-z*qT)+A8*exp(z*qT);
        sigzzmin=mu*(cL^2/cT^2-2)*(diff(fmin,z,2)-(k^2)*fmin)
        +2*mu*(diff(fmin,z,2)-1i*k*diff(gmin,z));
        sigzzplus=mu*(cL^2/cT^2-2)*(diff(fplus,z,2)-(k^2)*fplus)
        +2*mu*(diff(fplus,z,2)-1i*k*diff(gplus,z));
        sigxz=mu*(2*1i*k*diff(fmin,z)+(k^2)*gmin+diff(gmin,z,2));
        eq1=subs(sigzzmin==0,z,0);
        eq2=subs(sigxz==0,z,0);
        eq3=subs(1i*k*fmin+diff(gmin,z)==0,z,h);
        eq4=subs(-1i*k*gmin+diff(fmin,z)+a*(sigzzmin-sigzzplus)/
        (-mb*omega^2+EI*(k^4))==0,z,h);
        eq5=subs(1i*k*fplus+diff(gplus,z)==0,z,h);
        eq6=subs(-1i*k*gplus+diff(fplus,z)+a*(sigzzmin-sigzzplus)/
        (-mb*omega^2+EI*(k^4))==0,z,h);
        eq7=subs(1i*k*fplus+diff(gplus,z)==0,z,h+H);
        eq8=subs(-1i*k*gplus+diff(fplus,z)==0,z,h+H);
        eqns=[eq1 eq2 eq3 eq4 eq5 eq6 eq7 eq8];
        vars = [A1 A2 A3 A4 A5 A6 A7 A8];
        M = equationsToMatrix(eqns,vars);
        disprel = det(M);
    end
```

- Define the functions to be employed for finding the real zeros of the determinant:
    - Grid_zeros function [44]:

```
%% For every point of the grid the newton raphson method is applied
% to find the real zeros
function [z]=grid_zeros(fct, parameter_grid, constraint, descent)
z = zeros(size(parameter_grid, 1), size(parameter_grid, 2)+1);
for i=1:size(parameter_grid,1)
    warning off
    [x y] = newton_raphson(fct, parameter_grid(i, 1:end)', 500,
    10^(-2), descent, constraint);
    warning on
    z(i, 1:end) = [x' y];
    end
end
```

    - Newton_raphson function [45]:

```
function [x_value fct_value] = newton_raphson(fct, x0, iterations,
delta, is_descent, constraint)
%% Newton raphson method to find zero points
% fct = The function to optimize
% x0 = initial guess for the parameters
% iterations = maximum number of iterations allowed
% delta = convergence accuracy
% is_descent = steepest descent if true (minima), steepest ascent
% if false(maxima)
% constraint = function that constrains the search space to avoid
% ridiculous physical values. If the identity function is specified no
% constraint is applied.
% The gradient is presently calculated using finite differences.

% Variation
% Step size for finite differences
epsilon  = 10^(-6);
```

```
    % How fast the step size is grown or shrunk.
    % The stepsize prevents the algorithm from getting stuck if too large
    % or too small steps are taken.
    growth   = 1.1;
    % Initial guess for the stepsize.
    lambda    = 0.5;
    x = x0;
    prev_value = fct(x);
    for iter=1:iterations
        % For every iteration. Update x = x - stepsize*gradient
        new_x2 = x - lambda * prev_value./gradient(fct, x, epsilon);
        % Calculate the new function value.
        % Apply constraints
        new_x = constraint(new_x2)';
        new_value = fct(new_x);
        % If the function value and steps hardly change we are in a
        % minimum. Stop the algorithm and return x.
        if (~isnan(new_value) && abs(new_value) < delta &&
        sum(abs(x - new_x)) < delta)
            fprintf("Convergence Reached -  Iter: %d New function value:
            %f Lambda: %f x: %s new_x %s\n", iter, prev_value, lambda,
            %sprintf('%f ', x), sprintf('%f ', new_x2));
            fct_value = new_value;
            x_value = new_x;
            return;
        end

        % If the function increases we are taking too big steps. Decrease
        % the stepsize
        if (isnan(new_value) || abs(prev_value) < abs(new_value))
            lambda = lambda/growth;
        elseif (~isnan(new_value))
            % If the function value decreases we are closer to the local
            % minimum. Update x and increase the stepsize
            x = new_x;
            prev_value = new_value;
            if (new_value/prev_value > 0)
                lambda = lambda * growth;
            end
        end

    end
    % If maximum number of iterations is reached print a message
    fprintf("Convergence NOT Reached -  Iter: %d Convergence Error:
    %f New function value: %f Lambda: %f x: %s new_x
    %s\n", iter, abs(new_value-prev_value), prev_value, lambda,
    %sprintf('%f ', x), sprintf('%f ', new_x2));
    fct_value = NaN;
    x_value = x;
end
```

- Gradient function [46]:

```
     function [result]=gradient(fct, parameters, epsilon)
    % Calculates the gradient by applying simple finite differences.
    % We adjust the epsilon according to the value of the parameter
    % (smaller variations for small values, to
    % account for the different scales in different parameters).
    result = zeros(length(parameters), 1);
    root = fct(parameters);
    for i = 1:length(parameters)
```

```
        tmp = parameters;
        tmp(i) = tmp(i)*(1+epsilon);
        result(i, 1) = (fct(tmp) - root)/(tmp(i)*epsilon);
        end

    end
```

- The script "realzeros" finds the real zeros of the determinant function by calling the grid_zeros function given earlier:

```
%Import values of variables
run('modeldata.m')

% Function parameter for determinant.m
qL = @(k, omega) sqrt(k^2-omega^2/cL^2);
qT = @(k, omega) sqrt(k^2-omega^2/cT^2);

Create an anonimous function of this where all the parameters
% are filled in and this is passed to the newton_raphson routine.
g = @(k, omega) determinant(k,omega,qL,qT,h,cL,cT,EI,a,mu,mb)
f = @(x) double(sqrt(conj(g(x(1), x(2)))*g(x(1), x(2))));

% Create a grid of starting points for the search
grid = zeros(21*161, 2);
count = 1;
constraint = @(x) [max(0, min(x(1), 1.0)) max(0, min(x(2), 90))];
for k=0:0.05:1
    for omega=0:0.5:80
        grid(count, 1:end) = [k omega];
        count = count + 1;
    end
end
% Calculate a table of zeros, together with the function value.
h = @(x) double(conj(g(x(1), x(2)))*g(x(1), x(2)));
z=grid_zeros(h, grid, constraint, true)
z = z(~isnan(z(1:end, 3)), 1:end)% Show a graph with the zero points
% plot(z(1:end, 1), z(1:end, 2), 'k.')

% Calculate kR,kT and kL
omega_kRLT=0:5:80;
kR=omega_kRLT/cR;
kL=omega_kRLT/cL;
kT=omega_kRLT/cT;

%Plot the results as well as cR,cT,cL
figure;
plot(z(1:end, 1), z(1:end, 2), 'k-')
hold on
p(1)= plot(kR,omega_kRLT,'r--');
p(2)=plot(kT,omega_kRLT,'g--');
p(3)=plot(kL,omega_kRLT,'y--');
hold off
ylabel('\omega[rad/s]')
xlabel('k [rad/m]')
axis([0 1 0 70]);
legend(p([1 2 3]),'c_R','c_T','c_L','Location','Southeast')
```

- Define the functions to be employed for determining the local minima using grid optimization over k and ω:

- Grid_optimization function [47]:

```
%% For every point of the grid a gradient descent is performed to
% find minima
function [z]=grid_optimization
(fct, parameter_grid, constraint, descent)
    z = zeros(size(parameter_grid, 1), size(parameter_grid, 2)+1);
    for i=1:size(parameter_grid,1)
        [x y] = gradient_descent
        (fct, parameter_grid(i, 1:end)', 50000,
        10^(-6), descent, constraint);
        z(i, 1:end) = [x' y];
    end
end
```

- Gradient_descent function [48]:

```
function [minimum fct_value] = gradient_descent
(fct, x0, iterations, delta, is_descent, constraint)
%% GradientDescent is the core routine that looks for minima
% using steepest descent
% fct = The function to optimize
% x0 = initial guess for the parameters
% iterations = maximum number of iterations allowed
% delta = convergence accuracy
% is_descent = steepest descent if true (minima),
%steepest ascent if false (maxima)
% constraint = function that constrains the search space
% to avoid ridiculous physical values. If the
% identity function is specified no constraint is
% applied.
% The gradient is calculated using finite differences.

% Variation step size for finite differences
epsilon  = 10^(-6);
% How fast the step size is grown or shrunk. This means that in a
% little over 3 iterations the stepsize grows with a factor of 10.
% The stepsize prevents the algorithm from getting stuck if
% too large or too small steps are taken.
growth   = 1.25;
% Initial guess for the stepsize. Not so important, but 1/grad is used.
lambda    = 0.1/sum(abs(gradient(fct, x0, epsilon)));
if (is_descent)
    factor = 1;
else
    factor = -1;
end
x = x0;
prev_value = factor*fct(x);
for iter=1:iterations
    % For every iteration. Update x = x - stepsize*gradient
    new_x2 = x - factor*lambda*gradient(fct, x, epsilon);
    % Calculate the new function value.
    % Apply constraints
    new_x = constraint(new_x2)';
    new_value = factor*fct(new_x);
    % If the function value and steps hardly changes we are in a
    % minimum. Stop the algorithm and return x.
    if (~isnan(new_value) && abs(new_value-prev_value) < delta &&
    sum(abs(x - new_x)) < delta)
```

```
                fprintf("Convergence Reached -  Iter: %d Convergence Error:
                %f New function value: %f Lambda: %f x: %s new_x: %s \n", iter,
                %abs(new_value-prev_value), %prev_value, lambda, sprintf('%f ', x),
                %sprintf('%f ', new_x2));
                fct_value = factor*new_value;
                minimum = new_x;
                return;
            end

            % If the function increases we are taking too big steps. Decrease
            % the stepsize
            if (isnan(new_value) || prev_value < new_value)
                lambda = lambda/growth;
            elseif (~isnan(new_value))
                % If the function value decreases we are closer to the local
                % minimum. Update x and increase the stepsize
                x = new_x;
                prev_value = new_value;
                lambda = lambda * growth;
            end

        end
        % If maximum number of iterations is reached print a message
        fprintf("Convergence NOT Reached -  Iter: %d Convergence Error:
        %f New function value: %f Lambda: %f x: %s new_x %s\n",
        %iter, abs(new_value-prev_value), factor*prev_value, lambda,
        %sprintf('%f ', x), sprintf('%f ', new_x2));
        fct_value = NaN;
        minimum = x;
    end
```

- The script "dispcurves" finds the local minima of the determinant function by calling the grid_optimization function given earlier:

```
%Import values of variables
run('modeldata.m')

% Function parameter for determinant.m
qL = @(k, omega) sqrt(k^2-omega^2/cL^2);
qT = @(k, omega) sqrt(k^2-omega^2/cT^2);

% % We are interested in optimizing the absolute value of the determinant
% function. Create an anonimous function of this where all the parameters
% are filled in and this is passed to the optimization routine.
g = @(k, omega) determinant(k,omega,qL,qT,h,cL,cT,EI,a,mu,mb);

f = @(x) double(sqrt(conj(g(x(1), x(2)))*g(x(1), x(2))));

% Create a grid of starting points for the optimization
grid = zeros(19*80, 2);
count = 1;
constraint = @(x) [max(0, min(x(1), 1.0)) max(0, min(x(2), 90))];
for k=0.1:0.05:1
    for omega=0.001:1:80
        grid(count, 1:end) = [k omega];
        count = count + 1;
    end
end
% Calculate a table of minima, together with the function value.
```

```
z=grid_optimization(f, grid, constraint, true)

% Caluculate kR,kT and kL
omega_kRLT=0:5:80;
kR=omega_kRLT/cR;
kL=omega_kRLT/cL;
kT=omega_kRLT/cT;

%Find the tangent to the lowest dispersion curve
% Filter out irrelevant minima.
relevant = z
relevant = relevant(~isnan(relevant(1:end, 3)), 1:end)
relevant = relevant((relevant(1:end, 1) < 0.1) |
(60* relevant(1:end, 1) < relevant(1:end, 2)), 1:end)
relevant = relevant((relevant(1:end, 1) < 0.05) |
(100*relevant(1:end, 1) >= relevant(1:end, 2)), 1:end)
plot(relevant(1:end, 1), relevant(1:end, 2), 'k.')
%Perform a least squares fit
fit = glmfit(relevant(1:end, 1), relevant(1:end, 2))
range = 0:1

%Plot the results as well as cR,cT,cL
figure;
plot(z(1:end, 1), z(1:end, 2), 'k.')
ylim([0 80])
hold on
p(1)= plot(kR,omega_kRLT,'r--');
p(2)=plot(kT,omega_kRLT,'g--');
p(3)=plot(kL,omega_kRLT,'y--');
hold off
ylabel('\omega[rad/s]')
xlabel('k [rad/m]')
axis([0 1 0 80]);
legend(p([1 2 3]),'c_R','c_T','c_L','Location','Southeast')
```

C.2. MATLAB CODE FOR FINDING THE PEAKS IN THE VALUE OF THE INTEGRAND

For determining the peaks of the integrand in eq. (4.2) the grid optimization technique is applied again. The Matlab code is given below.

- Define the integrand:

```
    function [Int] = Integrand(omega,k,V,mu,mu_star,lambda_star,rho,cL,cT,EI,a,h,mb)

%introduce the variables defined in Chapter 3
cL_tilde = cL^2+(lambda_star+2*mu_star)/rho*(1i*omega-1i*k*V);
cT_tilde = cT^2+ mu_star/rho*(1i*omega-1i*k*V);
mu_sk = mu + mu_star*(1i*omega-1i*k*V);
% If real part of RL or real part of RT is negative change RL,RT to -RL,-RT
RLHat = RL(k, omega, V);
if real(RLHat) < 0
    RLHat = -RLHat;
end
RTHat = RT(k, omega, V);
if real(RTHat) < 0
    RTHat = -RTHat;
    end
vb = 1;
```

```
%Define variables necessary to find the constants Ai
alpha = cL^2-2*cT^2;
gamma = 4*RL*RT*cT^2;
beta  = RL^2*cL^2;

%% Derived with Maple

N1 = vb*RT*((alpha*k^4+(alpha*RT^2+gamma-beta)*k^2-beta*RT^2)*exp(-h*(RL+2*RT))
+(alpha*k^4+(alpha*RT^2-gamma-beta)*k^2-beta*RT^2)*exp(-h*RL)
+4*k^2*cT^2*(RT^2+k^2)*exp(-h*RT));
N2 = -vb*RT*((alpha*k^4+(alpha*RT^2-gamma-beta)*k^2-beta*RT^2)*exp(-2*h*RT)
+(alpha*k^4+(alpha*RT^2+gamma-beta)*k^2-beta*RT^2)
+(4*k^2*cT^2*(RT^2+k^2)*exp(-h*(RL+RT))));
N3 = 1i*vb*k*(-4*RT*RL*(alpha*k^2-beta)*exp(-h*RL)+(alpha*k^4
+(alpha*RT^2-gamma-beta)*k^2-beta*RT^2)*exp(-h*RT)+(-alpha*k^4
+(-alpha*RT^2-gamma+beta)*k^2+beta*RT^2)*exp(-h*(2*RL+RT)));
N4 = 1i*vb*k*(-4*RT*RL*(alpha*k^2-beta)*exp(-h*(RL+RT))+(-alpha*k^4
+(-alpha*RT^2-gamma+beta)*k^2+beta*RT^2)
+(alpha*k^4+(alpha*RT^2-gamma-beta)*k^2-beta*RT^2)*exp(-2*h*RL));
N5 = RT*vb;
N6 = -1i*k*vb;
Dmin = (-RL*RT+k^2)*(alpha*k^4+(alpha*RT^2+gamma-beta)*k^2-beta*RT^2)
*exp(-2*h*(RL+RT))-(RL*RT+k^2)*(alpha*k^4
+(alpha*RT^2-gamma-beta)*k^2-beta*RT^2)
*exp(-2*h*RT)-(RL*RT+k^2)*(alpha*k^4
+(alpha*RT^2-gamma-beta)*k^2-beta*RT^2)
*exp(-2*h*RL)+(-RL*RT+k^2)*(alpha*k^4
+(alpha*RT^2+gamma-beta)*k^2-beta*RT^2)
+8*RL*RT*k^2*((cL^2-3*cT^2)*k^2-beta-RT^2*cT^2)*exp(-h*(RL+RT));
Dplus = -RL*RT+k^2;

%define constants
A1 = N1/Dmin;
A2 = N2/Dmin;
A3 = N3/Dmin;
A4 = N4/Dmin;
A5 = N5/Dplus;
A6 = N6/Dplus;

%define stresses at z=h
Szzmin  = -2*mu_sk/cT^2*(A1*(alpha*k^2-beta)/2*exp(-h*RL)
+A2*(alpha*k^2-beta)/2 +A3*1i*RT*cT^2*k*exp(-h*RT)
-A4*1i*RT*cT^2*k);
Szzplus = mu_sk/cT^2*(A5*(beta-cL^2*k^2+2*cT^2*k^2)-A6*2*1i*RT*cT^2*k);



%define integrand
Int = (mb*(1i*omega-1i.*k*V).^2+EI.*k.^4+a*(Szzmin-Szzplus)/vb).^(-1);
end
```

- The script "peaksintegrand" finds the local maxima of the integrand function by calling the grid_optimization function given earlier:

```
     %Import values of variables
run('modeldata.m')

% Function parameter for integrand.m
```

```
cL_tilde = @(k, omega, V) cL^2+(lambda_star+2*mu_star)/rho*(1i*omega-1i*k*V);
cT_tilde = @(k, omega, V) cT^2+ mu_star/rho*(1i*omega-1i*k*V);
mu_sk = @(k, omega, V) mu + mu_star*(1i*omega-1i*k*V);
RL = @(k, omega, V) sqrt(k.^2+(1i*omega-1i.*k*V).^2/cL_tilde(k, omega, V));
RT = @(k, omega, V) sqrt(k.^2+(1i*omega-1i*k*V).^2/cT_tilde(k, omega, V));

% We are interested in optimizing the absolute value of the integrand
% function. Create an anonimous function of this where all the parameters
% are filled in and this is passed to theoptimization routine.
g = @(k, omega, V) integrand(k,omega,V,RL,RT,h,cL,cT,EI,a,mu,mu_star,mb);
f = @(x) 10^(8)*double(sqrt(subs(conj(g(x(1), x(2), x(3)))
*g(x(1), x(2), x(3)))));
constraint = @(x) [ max(0, min(x(1), 1.5)) max(0, min(x(2), 90))
max(0.0, min(x(3), 2.7*cT))];
grid = zeros(6*8*8, 3);
count = 1;
for V=0.2:0.5:2.7
    for k=[0:0.4:1.5]
        for omega=10:10:80
            grid(count, 1:end) = [k omega V*cT];
            count = count + 1;
        end
    end
end
y=grid_optimization(f, grid, constraint, false)
```

D

Appendix D

The Matlab code employed to determine the value of $\chi_{\mathrm{eq}}^{\mathrm{beam}}$ is depicted below.

- Integration_method function [49] performs an initial grid refinement, carries out the Riemann summation and subsequently, refines the grid based on the size of the errors:

```
function [answer, error] = Integration(fct, method, initial_grid, tolerance)
%% Integrates a function fct over a grid.
% fct = function to integrate
% method = riemann  Uses simple Riemann sums o
% initial_grid = an initial guess for the grid based on the integrand peaks
% tolerance = The allowed error as fraction of the integrand.

    % Maximum number of iterations. Note that since the grid take the
    % largest errors and divides their grid by half the algorithm should
    % converge exponentially so only a few iterations should be needed.
    MAX_ITERATIONS = 40;
    if (strcmp(method, "riemann"))
        [answer, error, iter] = Integration_riemann(fct, initial_grid,...
        tolerance, MAX_ITERATIONS);
    end
end

function [new_grid new_values] = refine_grid(old_grid, old_values, fct,...
refinement, refining_indices)
%% Function to break the grid into smaller pieces for either specific indices
% or the whole grid
% For efficiency fct is only calculated on newly calculated grid points
% old_grid = The grid to interpolate
% old_values = The function values on the old_grid points
% fct = The interpolating function
% refinement = The number of points to split the grid in
% refining_indices = Which gridpoints need to be split, [] splits all.
    if not(length(refining_indices))
        refining_indices = 1:(length(old_grid)-1);
    end
    mixing = 0;
    j = 1;
    k = 1;
    % Reserve space for the old grid+refined gridpoints
    new_grid    = zeros(length(old_grid)+length(refining_indices)*...
```

```
    (refinement-1), 1);
    new_values  = zeros(length(old_grid)+length(refining_indices)*...
    (refinement-1), 1);
    for i=1:length(new_grid)
        if (refining_indices(j) == k)
        %If the current gridpoint is refined, start mixing the current
        %gridpoint with the next one and calculate fct for the new
        %gridpoints
           new_grid(i) = (1-mixing)*old_grid(k)+mixing*old_grid(k+1);
           if (mixing > 0)
               new_values(i) = fct(new_grid(i));
           else
               new_values(i) = old_values(k);
           end
           mixing = mixing + 1/refinement;
           % If we are at the next gridpoint we are done.
           if (mixing >= 1.0)
               mixing = 0;
               j = min(j+1, length(refining_indices));
               k = k+1;
           end
        else
           % The current gridpoint does not need to be refined and the old
           % values are simply copied
           new_grid(i) = old_grid(k);
           new_values(i) = old_values(k);
           k = k+1;
       end
    end
end

function [result_grid, result_values] = interpolate_nans(grid, values)
    % Remove any gridpoints for which fct is not defined,
    % this might happen if the grid becomes too fine and you
    % run into the numerical precision of matlab (~10^(-16)).
    result_grid = grid(~isnan(values));
    result_values = values(~isnan(values));
    return;
end

function [answer, error, iterations] = Integration_riemann(fct,...
initial_grid, tolerance, MAX_ITERATIONS)
    % Perform integration of a function using riemann sums.
    % The first step is to make the initial grid reasonably fine.
    % Then the largest errors are found and only they are refined by a
    % factor of 2, since we are not interested in slowing things down for
    % areas for which the integral is already reasonably approximated.
    % In order to avoid problems with the numerical precision the
    % integration values and errors per gridpoint are corrected for the
    % approximate average size of a gridpoint.
    values          = arrayfun(@(x) fct(x), initial_grid);
    [grid, values]  = refine_grid(initial_grid, values, fct, 10, []);
    grid_size       = length(grid)*10^6;
    [grid, values]  = interpolate_nans(grid, values);
    mid_point       = @(index) 0.5*(grid(index+1) + grid(index));
    area        = @(index) 0.5*grid_size*(values(index) + values(index+1))*...
    (grid(index+1) - grid(index));
    error       = @(index) grid_size*abs(values(index) - values(index+1))*...
    (grid(index+1) - grid(index));
    integrands  = arrayfun(area, 1:(length(values)-1))';
    errors      = arrayfun(error, 1:(length(values)-1))';
    for iter=0:MAX_ITERATIONS
```

```
        iterations = iter;
        if (iter >= 1 && sum(errors)< tolerance*abs(sum(integrands)))
         % Convergence reached
            break
        end
        if (iter>= MAX_ITERATIONS)
            fprintf('Convergence not reached. Iter: %d Error: %.18f\n',...
            iter, sum(errors));
        end
        mid_point   = @(index, grid) 0.5*(grid(index+1) + grid(index));
        area        = @(index, values, grid) (0.5*(grid_size*values(index) +...
        grid_size*values(index+1)))*(grid(index+1) - grid(index));
        error       = @(index, values, grid) (abs(grid_size*values(index) -...
        grid_size*values(index+1)))*(grid(index+1) - grid(index));

        large_errors = find(errors > max(errors)*0.2);
        grid_size   = 2*(grid_size+1);
        [grid, values]  = refine_grid(grid, values, fct, 2, large_errors);
        [grid, values]      = interpolate_nans(grid, values);
        integrands  = arrayfun(@(index) area(index, values, grid),...
        1:(length(grid)-1))';
        errors      = arrayfun(@(index) error(index, values, grid),...
        1:(length(grid)-1))';
    end

    answer = sum(integrands)/grid_size;
    error  = sum(errors);
end
```

- Script "Integration" calls the function Integration_method to determine $\chi_{\mathrm{eq}}^{\mathrm{beam}}$:

```
format long
%Import values of variables
run('modeldata.m')
%run first the script peaksintegrand and the remove the rows where the
%script gives NaN value for the peak of the integrand. Then sort the
%values of k where there are peaks from low to high and define upper and
%lower bounds for integration
run('peaksintegrand.m')

y(any(isnan(y), 2), :) = [];
y=sortrows(y,1);
lb=[0;y(:,1)];
ub=[y(:,1);10000];

%define integration routine
err=1e-2;
omega1=-300:1:300;
%replace omega=0 by omega=0.0001 to avoid division by zero
omega=[omega1(1:300) 0.0001 omega1(302:601)];

%Define velocity range
B=0.2:0.1:2.9;
L=[B(1:8) 0.95 B(9:end)];

integration_method = "riemann";

A = cell(1,length(L));
Re_A = cell(1,length(L));
Im_A = cell(1,length(L));
```

```
parfor i=1:length(L) %parfor to use parallel for-loop to speed up computation
    V=L(i)*cT;
    T = zeros(length(omega),1);
    Re_T= zeros(length(omega),1);
    Im_T= zeros(length(omega),1);
    for j=1:length(omega)
        fprintf('i: %d, j: %d - V: %f omega: %f\n', i, j, L(i), omega(j))

        %START NUMERICAL INTEGRATION
        Integrand_real=@(k)(real(integrand(k,omega(j),V,RL,RT,h,cL,cT,EI,...
        a,mu,mu_star,mb) + integrand(-k,omega(j),V,RL,RT,h,cL,cT,EI,...
        a,mu,mu_star,mb)));
        Integrand_im =@(k)(imag(integrand(k,omega(j),V,RL,RT,h,cL,cT,EI,...
        a,mu,mu_star,mb) + integrand(-k,omega(j),V,RL,RT,h,cL,cT,EI,...
        a,mu,mu_star,mb)));
        %integration from 0 to inf instead of from -inf to inf so take
        %f(k)+f(-k) (see explanation chapter 4)

        % define integration grid based on earlier found integrand peaks
        grid = real([lb; ub(end)]);
        int_re = Integration_method(Integrand_real, integration_method,...
        grid, err);
        int_im = Integration_method(Integrand_im, integration_method,...
        grid, err);
        int = complex(int_re, int_im);
        T(j,1)=(1/(2*pi)*int)^(-1);
        Re_T(j,1)=real(T(j,1));
        Im_T(j,1)=imag(T(j,1));
    end
    A{1,i} = T;
    Re_A{1,i} = Re_T;
    Im_A{1,i} = Im_T;
end

% Fill matrix with values of equivalent beam stiffness for every omega and V
Chi_eq_beam_mustar01pc=horzcat(A{:});
Re_chi_eq_beam_mustar01pc=horzcat(Re_A{:});
Im_chi_eq_beam_mustar01pc=horzcat(Im_A{:});


% Plot the imaginary part of the equivalent stiffness of the beam against
% the frequency omega for omega going from 0 to 40
set(0,'DefaultFigureWindowStyle','docked')

for i=1:length(L)
    figure;
    % plot Re(chi_eq_beam) for \omega from 0.0001 to 40
    subplot(2,2,1);
    p(1)=plot(omega(301:341),Re_chi_eq_beam_mustar01pc(301:341, i)*10^(-6),'k');
    ylabel('Re(Chi_{eq}^{beam}) [MPa*m]')
    xlabel('omega [rad/s]')
    title(sprintf('V=%.3f*cT', L(i)))
    subplot(2,2,2);
    p(1)=plot(omega(301:341),Im_chi_eq_beam_mustar01pc(301:341,i)*10^(-6),'k');
    ylabel('Im(Chi_{eq}^{beam}) [MPa*m]')
    xlabel('omega [rad/s]')
    title(sprintf('V=%.3f*cT', L(i)))
    % % plot Im(chi_eq_beam) for \omega from 0.0001 to 10
    subplot(2,2,3);
    p(1)=plot(omega(301:311),Im_chi_eq_beam_mustar01pc(301:311,i)*10^(-6),'k');
    ylabel('Im(Chi_{eq}^{beam}) [MPa*m]')
```

```
    xlabel('omega [rad/s]')
    title(sprintf('V=%.3f*cT', L(i)))
    subplot(2,2,4);
    p(1)=plot(omega(301:341),Im_chi_eq_beam_mustar01pc(301:341,i)*10^(-6),'c');
    hold on
    p(2)=plot(omega(301:341),Re_chi_eq_beam_mustar01pc(301:341,i)*10^(-6),'r');
    hold off
    ylabel('Chi_{eq}^{beam}[MPa*m]')
    xlabel('omega [rad/s]')
    legend(p([1 2]),'Im(Chi_{eq}^{beam})','Re(Chi_{eq}^{beam})',...
    'Location','Southeast')
    title(sprintf('V=%.3f*cT', L(i)))
end
```

E

APPENDIX E

This appendix includes the Matlab code applied to perform the D-decomposition and subsequently determine the instability domain.

- D-decomposition of the m_1-plane:

```
%to be executed with workspace variables from the integration (See Appendix D)
%determining chi_eq_beam_mustar01pc!!

m1=zeros(length(omega),length(L));
Re_m1=zeros(length(omega),length(L));
Im_m1=zeros(length(omega),length(L));
for i=1:length(L)
    for j =1:length(omega)
        m1(j,i)= Chi_eq_beam_mustar01pc(j,i)/omega(j)^2;
        Re_m1(j,i)=real(m1(j,i));
        Im_m1(j,i)=imag(m1(j,i));
    end
end

%% Draw the D-decomposition curves
set(0,'DefaultFigureWindowStyle','docked')
for i=1:length(L)
    figure;
    plot(Re_m1(:,i),Im_m1(:,i),'-b')
    ylabel('Im(m_1)[kg]')
    xlabel('Re(m_1)[kg]')
    ax = gca;
    ax.XAxisLocation = 'origin';
    ax.YAxisLocation = 'origin';
    title(sprintf('V=%.3f*cT', L(i)))
end
```

- Instability domain for m_1:

```
   %to be executed after m1singlemass(j,i) has been calculated!

LineVphmin=linspace(0,9e7);
Vphmin=ones(1,100)*0.898*cT;
```

```
m1_instab=NaN(2,length(L));
tol=1e-2;
for i=1:length(L)
    % Execute two separate loops for negative and positive omega to
    % exclude omega=0 (so element 301 from the omega array)
    % from the calculation to avoid division by omega for p =1:299
        % Only consider the positive real values of m1
        if Re_m1(p,i)>=0 && Im_m1(p,i)*Im_m1(p+1,i)<=0
           %Use linear interpolation between two points
            m1_instab(1,i)=Re_m1(p,i)+(Re_m1(p+1,i)-Re_m1(p,i))/...
            (Im_m1(p+1,i)-Im_m1(p,i))*(0-Im_m1(p,i));
            break
        end
    end
    for j =302:600
        if Re_m1(j,i)>=0 && Im_m1(j,i)*Im_m1(j+1,i)<=0
           %Use linear interpolation between two points
            m1_instab(2,i)=Re_m1(j,i)+(Re_m1(j+1,i)-Re_m1(j,i))/...
            (Im_m1(j+1,i)-Im_m1(j,i))*(0-Im_m1(j,i));
            break
        end
    end
    % if the imaginary m1-axis crosses the real m1-axis in the same
    % point for negative and positive omega, delete the second row
    if  abs(m1_instab(1,i)-m1_instab(2,i))<tol
        m1_instab(2,i)=NaN;
    end
end


figure;
p(1)= plot(L(1,:)*cT,m1_instab(1,:),'-k');
hold on
p(2)=plot(Vphmin(1,:),LineVphmin,'--k');
hold off
xlabel('Velocity V [m/s]')
ylabel('Mass m_1[kg]')
ax = gca;
ax.XAxisLocation = 'origin';
ax.YAxisLocation = 'origin';
```

- D-decomposition of the K-plane:

```
%to be executed with workspace variables from the integration
%(See Appendix D)determining chi_eq_beam_mustar01pc!!
 m2  = 20000;
 m1  = 2000;%mass of vehicle bogies and suspension
 eps = 0;%damping coefficient oscillator
 K_oscillator=zeros(length(omega),length(L));
 Re_K=zeros(length(omega),length(L));
 Im_K=zeros(length(omega),length(L));
 omega=-300:1:300;

 for i=1:length(L)
     for j =1:length(omega)
         if omega(j)==0
             omega(j)=0.0001;
         end
         K_oscillator(j,i)= -1i*eps*omega(j)+m2*(omega(j))^2*
         (Chi_eq_beam_mustar01pc(j,i)-m1*(omega(j))^2)/
```

```
        (Chi_eq_beam_mustar01pc(j,i)-m2*(omega(j))^2-m1*(omega(j))^2);
        Re_K(j,i)=real(K_oscillator(j,i));
        Im_K(j,i)=imag(K_oscillator(j,i));
    end
end
```

- Instability domain for K:
    - Crossing function [50] finds the crossings of the D-decomposition curve with the real and positive K-axis:

```
     function [ind,t0,s0,t0close,s0close] = crossing(S,t,level,imeth)
% CROSSING find the crossings of a given level of a signal
%   ind = CROSSING(S) returns an index vector ind, the signal
%   S crosses zero at ind or at between ind and ind+1
%   [ind,t0] = CROSSING(S,t) additionally returns a time
%   vector t0 of the zero crossings of the signal S. The crossing
%   times are linearly interpolated between the given times t
%   [ind,t0] = CROSSING(S,t,level) returns the crossings of the
%   given level instead of the zero crossings
%   ind = CROSSING(S,[],level) as above but without time interpolation
%   [ind,t0] = CROSSING(S,t,level,par) allows additional parameters
%   par = {'none'|'linear'}.
%   With interpolation turned off (par = 'none') this function always
%   returns the value left of the zero (the data point thats nearest
%   to the zero AND smaller than the zero crossing).
%
%   [ind,t0,s0] = ... also returns the data vector corresponding to
%   the t0 values.


% check the number of input arguments
error(nargchk(1,4,nargin));

% check the time vector input for consistency
if nargin < 2 || isempty(t)
    % if no time vector is given, use the index vector as time
    t = 1:length(S);
elseif length(t) ~= length(S)
    % if S and t are not of the same length, throw an error
    error('t and S must be of identical length!');
end

% check the level input
if nargin < 3
    % set standard value 0, if level is not given
    level = 0;
end

% check interpolation method input
if nargin < 4
    imeth = 'linear';
end

% make row vectors
t = t(:)';
S = S(:)';

% always search for zeros. So if we want the crossing of
% any other threshold value "level", we subtract it from
```

```
% the values and search for zeros.
S   = S - level;


% then look for zero crossings between data points
S1 = S(1:end-1) .* S(2:end);
ind1 = find( S1 < 0 );

% sort indices in ascending order
ind = sort([ind1]);

% and pick the associated time values
t0 = t(ind);
s0 = S(ind);

if strcmp(imeth,'linear')
    % linear interpolation of crossing
    for ii=1:length(t0)
        if abs(S(ind(ii))) > eps(S(ind(ii))) % interpolate only when data point
        % is not already zero
            NUM = (t(ind(ii)+1) - t(ind(ii)));
            DEN = (S(ind(ii)+1) - S(ind(ii)));
            DELTA =  NUM / DEN;
            t0(ii) = t0(ii) - S(ind(ii)) * DELTA;
           % set the corresponding value of the signal to zero
            s0(ii) = 0;
        end
    end
end
```

- Script "Instabilitydomain_K" calls the function Crossing to determine the instability domain for the oscillator stiffness:

```
% to be executed with the values obtained from D-decomposition
% of the K-plane
K_instab_mustar01pc=zeros(10,length(L));
tol=1e-4;
for i=1:length(L)
     % find the crossing points for each velocity and sort them
     % in descending order
    [ind,Re_0] = crossing(Im_K(:,i),Re_K(:,i));
    K_cross=sort(Re_0,'descend');
    for j=1:(size(K_cross,2)-1)
        if abs(K_cross(1,j+1)-K_cross(1,j))<tol
            K_cross(1,j+1)=NaN;
        end
    end
    %fill the ith column with the values of k_cross
    K_instab_mustar01pc(1:size(K_cross,2),i)=K_cross;
end

%set zeros equal to NaN
K_instab_mustar01pc(K_instab_pod==0)=NaN;

% sort K_instab from high to low
K_instab_mustar01pc(isnan(K_instab_pod)) = -Inf;
K_instab_mustar01pc = sort(K_instab_pod,1,'descend');
K_instab_mustar01pc(isinf(K_instab_pod)) = NaN;

% plot the instability domain
figure;
```

```
p(1)=plot(L(1,:)*cT,K_instab_pod(1,:),'-b');
xlabel('Velocity V [m/s]')
ylabel('Stiffness K[N/m]')
ax = gca;
ax.XAxisLocation = 'origin';
ax.YAxisLocation = 'origin';
```

F

APPENDIX F

Figure F.1 presents the D-decomposition of the K-plane for the model including the magnetic levitation suspension. The full-scale model of Hyperloop pod and track is observed and the pod is moving through a normal strength concrete tunnel. The employed parameter values are given in tables 4.1, 4.3, 4.4 and 5.2
The number of 'unstable roots' per domain of the decomposed K-plane is given by the red numbers in the figures. Only the positive and real values of the spring stiffness are physically relevant, so only the positive part of the real K-axis is observed.

Let us now analyze the presented D-decomposition curves. As for the model without EDS, the D-decomposition curve has no crossing points with the real K-axis for the sub-critical velocity $V = 0.9c_T$ and thus, the vibrations of the oscillator are unconditionally stable.
In case of super-critical motion of the oscillator $(V = 1.4c_T)$ the mapped line crosses the $\Re(K)$-axis twice in the same point. The critical stiffness K^* below which instability occurs is denoted in the fig. F.1b.

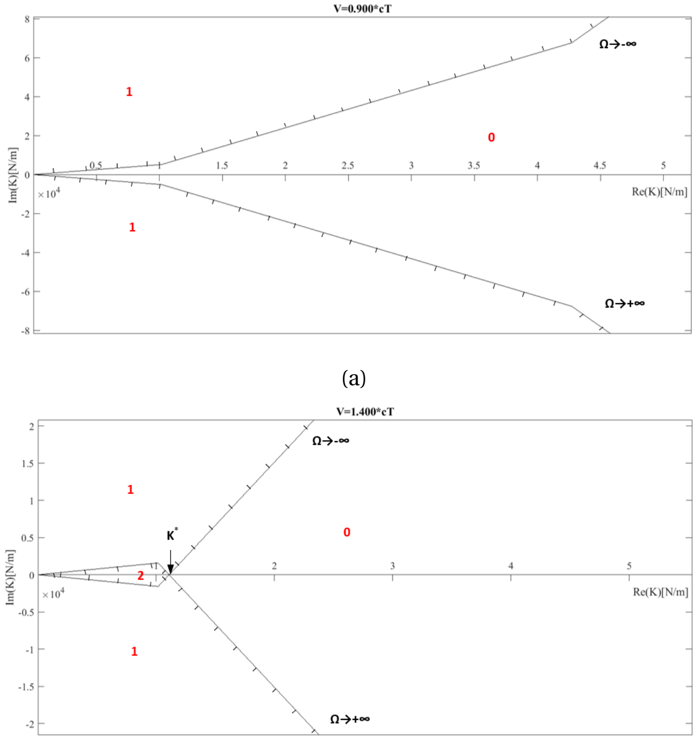

(a)

(b)

Figure F.1: Separation of the complex K-plane into domains with different number of 'unstable roots' (number given in each figure) for (a) sub-critical motion and (b) super-critical motion of the oscillator along the beam embedded in the half-plane. The electrodynamic suspension system has been included in the model by means of a magnetic spring with stiffness k_1

F